Investigation of Terahertz Band and Graphene based Antennas

A

Thesis Submitted

in Partial Fulfilment of the Requirements

for the Degree of

DOCTOR OF PHILOSOPHY

By

Mrinmoy Bharadwaj

Department of Electronics and Electrical Engineering

Indian Institute of Technology Guwahati

Guwahati - 781039, INDIA.

April 2021

Investigation of Terahertz Band and Graphene based Antennas

A

Thesis Submitted

in Partial Fulfilment of the Requirements

for the Degree of

DOCTOR OF PHILOSOPHY

By

Mrinmoy Bharadwaj

Department of Electronics and Electrical Engineering

Indian Institute of Technology Guwahati

Guwahati - 781039, INDIA.

April 2021

Dedicated to

My Beloved Parents

Mrs. Mamoni Kataky and **Dr. J. C. S. Kataky**

My Caring Sister

Ms. Neelakshi Kataky

My Teachers, Mentors

and

My Loving Wife

Mrs. Sukanya Baruah Bharadwaj

Certificate

This is to certify that the thesis titled "**Investigation of Terahertz Band and Graphene based Antennas**," submitted by **MRINMOY BHARADWAJ** (**126102008**), a doctoral student in the Department of Electronics and Electrical Engineering, Indian Institute of Technology Guwahati, for the award of the degree of **Doctor of Philosophy**, has been carried out by him under my supervision and guidance. The thesis has fulfilled all requirements as per the regulations of the institute and, in my opinion, has reached the standard needed for submission. The results embodied in this thesis have not been submitted to any other University or Institute for the award of any degree or diploma.

Dated: 15/05/2020

Place: Guwahati.

Prof. Ratnajit Bhattacharjee
Department of Electronics & Electrical Engineering
Indian Institute of Technology Guwahati
Guwahati - 781039, Assam, India.

Acknowledgements

Foremostly, I express my sincere respects and profound gratitude towards my supervisor Professor Ratnajit Bhattacharjee for his unwavering faith in my capability and his invaluable guidance throughout my journey towards my doctoral degree. His patience, kindness, dedication and his vast enriching volume of knowledge has help me learn a lot of fundamental topics in my area of research. His attention to detail has taught me to visualize several key points in multiple perspectives. Every discussion with him had instilled motivation and persistence in me even at times of distress and distractions, for which I owe sincere gratitude to him. His unending support and motivations has enriched my life in a lot of significant ways.

I would like to thank Chairman and all the members of my doctoral committee: Prof. Anup Kumar Gogoi, Prof. Rakhesh Singh Kshetrimayum, Dr. Ramesh Kumar Sonkar, Dr. Gagan Kumar and Dr. Mahima Arawatia, for their invaluable suggestions and feedback during the Annual Progress Seminars which has helped in structuring up my course of research. I thank them for finding time out of their busy schedules to periodically evaluate the progress of my research work. I would also take this opportunity to express my gratitude towards Prof. Anup Kumar Gogoi (Retd.), former chairman of my Doctoral committee, for his guidance, suggestions and support.

I thank and convey my gratitude towards Indian Institute of Technology Guwahati, for allowing me to carry out my Doctoral Research in the Department of Electronics and Electrical Engineering and avail all the institute facilities. I extend my gratitude to the Central Instruments Facility, IIT Guwahati for allowing me to carry out several material characterizations for the purpose of my research work. I would also like to sincerely thank the Hostel Affairs Board for allowing me to be a boarder at Brahmaputra Hostel Room F177, which was my abode for the entire tenure of my thesis work. Also, I thank the student gymkhana for allowing me to avail all the sports and recreational facilities.

I would to extend my sincere and heartfelt gratitude to Prof. Pugazhenthi G., Department of Chemical Engineering, IIT Guwahati for his incessant love and support during the entire

course of my research work. He allowed uninterrupted access to his laboratory and its facilities for my experiments. It was because of his love and kindness that I was able to push through lot of tough times and move ahead with my work. Especially, my contributions towards the Graphene based research works were possible only through his help and constant support.

I thank all the faculties of Department of EEE, IIT Guwahati who, at some or the other point of my thesis work, have contributed directly or indirectly through discussions and suggestions. Especially, Prof. Sisir Kumar Nayak and Prof. Manas Kamal Bhuyan who have always been a constant support and motivation to me.

I would like extend my special and deep gratitude towards Dr. Lakshmi Haobam, Student Counselor IIT Guwahati for her incessant patience and care in supporting me emotionally and mentally when I was going through a really stressful phase in my research work. It was the discussions that I had with Dr. Lakshmi that helped my widen my perspectives and emerge as a stronger and more evolved individual. Her contributions in my life would always be priceless.

My special thanks to Mr. Pranab Jyoti Goswami, Dr. Sanjib Das, Mr. Utpal Sharma, Mr. S. S. Mazid and all the other technical staff of the Department of EEE, IIT Guwahati who had been a source of fun, happiness and support during the tenure of my research work. Everybody extended a helping hand whenever I needed one and made this experience really enjoyable.

I also extend my thanks to the office staff of Dept. of EEE, IIT Guwahati for their co-operation and support in all official matters pertaining to my Doctoral program. They always extended a helping hand.

I thank the caretaker of Brahmaputra Hostel, IIT Guwahati for making my boarding at the hostel a comfortable one. I also extend my sincere thanks to all the mess-workers, cleaning staff, canteen and stationery shop vendors for their support, services and co-operation in ensuring a comfortable and happy stay in the hostel.

I extend a deep and sincere thanks to my dear colleague, co-worker, co-author and friend Dr. Jitendra Prajapati for his invaluable contributions in my doctoral research. All his suggestions and discussions helped me in clearing a lot of doubts and together, we were able to make several significant contributions to the field of Terahertz Optoelectronic Antennas.

My sincere thanks to my dear friends and colleagues Dr. Kukil Khanikar, Mr. Dibyajyoti Das, Mr. Anoop P., Mr. Arijit Bhattacharjee Da, Dr. Shivanshu Shrivastava, Dr. Binod Prasad and several others who have always motivated and supported me to work better and improve. I truly apologize if I have left out any names here out of my poor memory yet I am grateful for the contributions of all my peers and juniors that were with me in this journey. I thank all my seniors who have helped and guided me along and at times, directly or indirectly made significant contributions to my improvement.

My special thanks to my Badminton co-players Prof. Pugazhenthi G., Prof. Ajay Kalamdhad, Dr. Ram Kumar Yadav, Mr. Jitendra Rawat, Dr. Robin George, Dr. Sharbani Kaushik, Ms. Swapnali Borah Ma'am, Ms. Parijat Ma'am and several others, who have made significant contributions and ensured that my stay here at IITG is a memorable one for life.

A special thanks to Dr. Ram Kumar Yadav and Mr. Jitendra Rawat, who always supported me like my brothers and ensured that I was always in my best spirits.

I would like to thank all my teachers and gurus who have guided my throughout my career and have made significantly enriching contributions in my personality and capabilities. Their blessings and lessons have helped me shape myself into a more evolved and valuable individual. Their ways have inspired me and motivated me to always strive for the better.

Over and above all, I would like to express a sincere and heartfelt gratitude towards my family (my father, mother sister and wife) for their unwavering love and incessant support throughout my doctoral program. I am always indebted to them for all the sacrifices that they have made and the opportunities that they have provided for making this journey a beautiful phase of my life. They are the reason and motivation behind all that I have accomplished so far.

Finally, I believe the experience that I have gained during this research work will definitely help in my future endeavours and benefit my career.

(Mrinmoy Bharadwaj)

Abstract

Inspite of research and developments in the Terahertz band of frequencies of the electromagnetic spectrum, this band has not been able to emerge as a favourable band for communication activities mainly due to unavailability of robust and inexpensive sources and detectors capable of working at Terahertz frequencies. Terahertz band is sandwiched between the optical and the microwave regions of the electromagnetic spectrum. One major technical issue is that the fundamental working principle of the devices working in the two bands around the Terahertz band are quite different. Therefore, the sources and detectors used in these two regions fail to perform when simply scaled to work in the Terahertz region. This fact necessitates development of such components whose working principle is suitable for the Terahertz frequencies. Various potentially important applications have been envisioned especially in the fields of medicine, security, defence and short-distance communication. Hence, a proper analysis and design procedure for efficient Terahertz sources and detectors is a need of the hour. The research reported in this thesis focuses on the various issues related to design of antenna systems, in the Terahertz band, which is an essential component of Terahertz band sources and detectors. The work presented in this thesis analyses in detail novel optoelectronic antenna systems which involve multiple physical phenomena in their operations. Graphene, in recent times, is emerging as an attractive material for various applications. This thesis also investigates application of Graphene in design of conventional as well as Terahertz band antennas.

Contents

List of Figures

List of Tables

List of Acronyms

CAD	:	Computer Aided Design
CRE	:	Classical Relaxation Effect
CST-MWS^{TM}	:	Computer Simulation Technology-Microwave Studio
CW	:	Continuous-Wave
DC	:	Direct Current
EM	:	Electromagnetic
FDTD	:	Finite Difference Time Domain
FFT	:	Fast-Fourier Transfrom
FLG	:	Few-Layer Graphite
Gbps	:	Giga Bits per second
GHz	:	Gigahertz
GNP	:	Graphene Nano Particles
h-BN	:	Hexagonal Boron Nitride
HFSS^{TM}	:	High Frequency Structure Simulator
IL	:	Insertion Loss
ISM	:	Industrial, Scientific and Medical
ITU	:	International Telecommunication Union
KCL	:	Kirchhoff's Current Law
KVL	:	Kirchhoff's Voltage Law
LTG-GaAs	:	Low-Temperature Grown Galium Arsenide
MLG	:	Multi-Layer Graphene
MSM	:	Metal-Semiconductor-Metal

PCA	:	Photoconductive Antenna
PIN	:	P-type Intrinsic N-type
PMA	:	Photomixing Antenna
RF	:	Radio Frequency
RMSA	:	Rectangular Microstrip Antenna
SLG	:	Single Layer Graphene
SNR	:	Signal to Noise Ratio
Tbps	:	Tera bits per second
THz	:	Terahertz
TM	:	Transverse Magnetic

1

Introduction

1.1 Introduction

The terahertz (THz) frequency band (0.3-3 THz, ITU) [1] [2] lies in between the infrared and millimetre wave band in the electromagnetic spectrum as shown in Figure 1.1. The wavelength span of this band, 1 - 0.1 mm, gives it its second and well-known name as the sub-millimetre wave band.

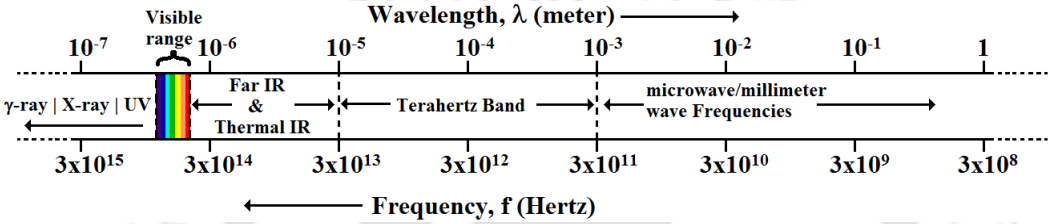

Figure 1.1: The electromagnetic spectrum

Although the THz band had been of interest to interferometry and spectroscopy applications since the 1920's [2], significant technological developments towards wireless communication in this band had been hindered by the lack of efficient and reliable sources and detectors. In fact, there is a lot of undetected and unnoticed THz energy pervading all universe. Several potential physical phenomena that go on inside matter and that are detectable only by THz interactions with the material are yet to be explored [2]. Propagation of THz through materials is expected to reveal unique macroscopic and physical properties of the internal structure of the material without the damage associated with ionizing radiations.

With new technical advancements in semiconductor and material science technologies [3], there has been an increase in efforts towards realization of suitable sources and detectors at the THz band over the last two decades. Consequently, applications of THz signals to various important fields such as biomedical [4, 5], medicine [6, 7], defence and security [8], space science [9, 10] etc. have also been reported.

The present research work, however, is motivated by the challenges of wireless communication in the THz band. Wireless communication in the THz band still remains a grey area because of the lack of suitable, economic and efficient transceivers and relevant sub-systems. In the following section we re-emphasize the potential and the factors drawing increased interest

towards wireless communications in the THz band.

1.2 Potential of THz Frequencies

In accordance to Edholm's law, the requirement for bandwidth in point-to-point communication and other multimedia links has doubled every 18 months over a period of 25 years. From basic circuit electronics we know that:

$$Bandwidth = \frac{Frequency}{Q - Factor} \tag{1.1}$$

A thousand fold increase in the net bandwidth requirement from 2010 to 2020 and a per user data rate requirement of 1 Gbps has been predicted in [11]. In order to support this increasing demand for more bandwidth and increased speeds, the carrier frequencies have to be increased further. This pressure has led scientists and researchers to look into the unallocated frequency bands in the electromagnetic spectrum used for communication purposes. THz frequency band is one such portion of the EM spectrum which is considered as a no man's land between microwave and optical bands. In a recent review [12], the THz band has been identified as the next frontier for wireless communications with speeds in the range of tera-bits per-second (tbps) and bandwidths in the range of terahertz. The THz band had already been put to use in applications such as THz spectroscopy. However with limited developments in the field, the THz band is yet to be explored from a communication perspective to its full potential. The millimeter wave (mm-Wave) band (30-300 GHz) provides enormous bandwidths as well and hence, is envisioned as the future of 5G mobile and multimedia communications [13].

In the field of communications, the THz frequencies present the potential of development of nano-networks [14, 15] which seems to be a new communication paradigm. Nano-antennas for operating in the THz band have also been studied, modelled and developed [16, 17].A concept of ultra-broadband THz communication, based on directed non-line-of-sight (NLOS) transmissions has been proposed in [18]. THz band also holds potential for applications in development of THz Nanocells, short-range data-transfer between different devices or modules in the same device (nano-communications), Kiosk downloading etc. A more detailed discussion about the

history and advantages about the THz band can be found in literature [2, 12, 19].

Though the need and potential of the THz band for wireless communications is now well understood, realizing systems at such high frequencies come with challenges which are discussed in the next section.

1.3 Technological Challenges

As discussed in [12], several research challenges in the THz band are yet to be overcome to explore its full potential. In the field of design of devices, there is a need to develop new wide and narrowband transceiver architectures that can operate efficiently and reliably at THz frequencies. The design must also be able to mitigate the high path-loss at the THz band with additional features like high power, high intensity and high Signal-to-Noise Ratio (SNR). Several alternative technologies have been proposed to this end. However further research is the need of the hour.

In the area of communication networks, a major amount of research has yet to be done in channel modelling (for line-of-sight, non line-of-sight, multi-path and noisy environments), network architecture, data modulation and coding schemes (characterization of error environment and development of efficient error detection and correcting codes), network synchronization, performance evaluation etc.

1.3.1 Technological Challenges in THz Antenna design and analysis

The realization of the next-generation wireless communication paradigm would indispensably depend on the availability of efficient transmitters and receivers operating at THz frequencies. The antenna being an integral component of any transmitter-receiver system, the main hurdle towards this objective has come from the lack of proper and efficient antennas capable of working at THz frequencies. Some of the key technological challenges faced by communication and antenna-design engineers world-wide have been:

- Scaling of conventional microwave antennas into the THz band.
- Very different source-detector technologies in the infra-red and optical frequency bands.

• High absorption of THz waves in moisture.

• Proper modelling and mathematical analysis for the individual components as well as the entire system.

• Analysis and design procedure for THz antennas.

• Electromagnetic Interference/Compatibility consideration at THz band scales.

• Development of proper simulation and CAD tools.

• Availability of proper testing and experimentation platforms.

• The need of proper micro-fabrication facilities for both laboratory and commercial ends.

1.3.2 Material Science and Technology

Another aspect to add to the above list is the behaviour of materials used in existing antenna technologies at THz frequencies. The constitutive parameters of the materials ϵ, μ, σ, which are fundamentally dispersive and complex in nature, vary with frequency. These variations are relatively negligible at micro-wave band frequencies, but start to matter as the wavelength reduces from mm to sub-mm wave regions of the spectrum. Many of the contemporary commercial EM solvers, presently, do not have enough provision of capturing some of these variations and therefore, at the sub millimeter band of frequencies, there are question marks regarding the reliability of the solutions obtained. Therefore, along with an update to the EM solvers, we also feel the need to look for materials which can be used predictably and reliably at the THz band.

A great deal of exploration and research has been invested in finding appropriate and efficient radiators, receivers, and data-processing subsystems capable of transmission, reception and processing of THz signals. Electronic components for working at sub-millimetre wavelengths and the materials to fabricate such components have also been investigated. In literature, the THz Photoconductive Antenna (PCA) [20] and the THz Photomixing Antenna (PMA) [21] are a popular candidate of choice for THz band sources where the combination of optical and electrical phenomena produces THz signals. In materials, Graphene [22] with its interesting and desirable properties has emerged as a popular material of choice for THz band antennas

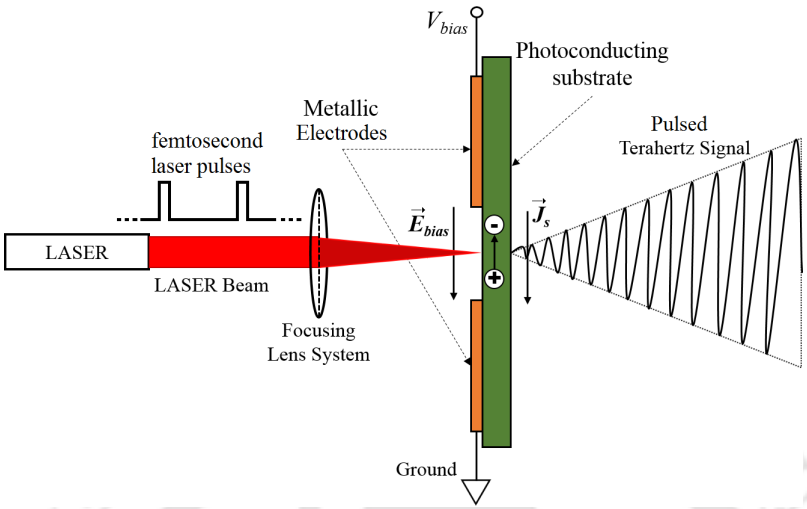

Figure 1.2: Antenna structure and operation of PCA

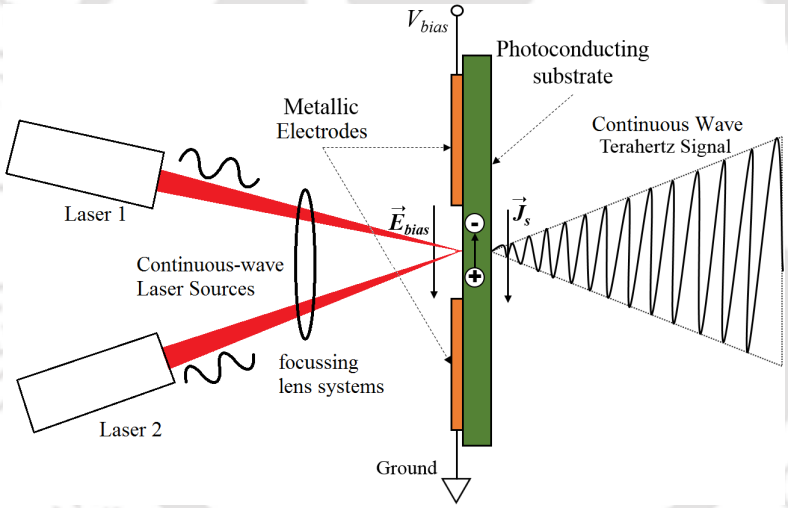

Figure 1.3: Antenna structure and operation of PMA

1.4 Literature Review

Photoconductive effect, in itself, is a well-known phenomenon since mid-1800 and has been used in several significant applications thereafter. However, utilizing photoconductivity to radiate THz signals was first reported by Auston in 1984 [20] wherein a photoconductive semiconductor material was irradiated with femtosecond wide laser pulses to generate charge carriers inside a photoconductive material which were accelerated by application of DC bias to give rise to THz signals. From a perspective of wireless communication this can be marked as beginning of THz PCA design and we carry out a survey of literature reported henceforth. The working

principle of a THz PMA is inherently similar to that of a PCA. The differences lie in the mechanism of laser illumination, nature of the output signal and the dynamic control of the radiated signal available in a PMA. That is why the review of existing literature has been carried out for both PCA and PMA in tandem. For the sake of clarity, Figure 1.2 and 1.3 depict the PCA and PMA structure and working.

The research work presented in [20] conceptualized the generation and reception of pulsed THz signals by using two identical PCAs as shown in Figure 1.4 wherein, a response time of 1.6 ps was reported in experiments. The approach reported mitigation of several limitations of the conventional transmission lines used in study of transient behaviours in materials. An approximate expression of the detector current and radiated electric field was presented but study of the influence of various geometrical and material factors in the analysis was not considered in detail. Although, some of these factors were addressed in [23], yet a complete analytical model was not presented. Radiation characteristics of large aperture PCAs was studied in [24] where the authors pointed out two main advantages of using large aperture PCAs as: the scalability of magnitude of the THz pulses with incident optical power and the steering capability of the main beam with varying angle of optical incidence. The authors compared the generation of THz pulses from large aperture PCAs in several substrates [25] and found that substrates with long free carrier lifetimes tend to be more useful for directional radiations. In [26], the authors further enhance the time resolution in [20] to 380 fs using repetitive optical excitation of the PCA. Using the Drude model and a frequency dependent mobility model, the authors derive a time domain material response function to the optical input. Scaling and saturation of radiated power from large aperture PCAs at high optical fluences have been discussed in [27–29]. Gap spacings of about 100 μm - 1 mm on the detector PCA were compared in experiments and a gap of 0.5 mm was found to be very sensitive. Expression for radiated near and far electric fields, derived from the first principles, have been presented. However, a thorough model of the semiconductor dynamics had not been addressed adequately. Effects of the spatial distributions of the bias voltage and carrier concentrations on the performance of THz PCAs has been discussed in [30]

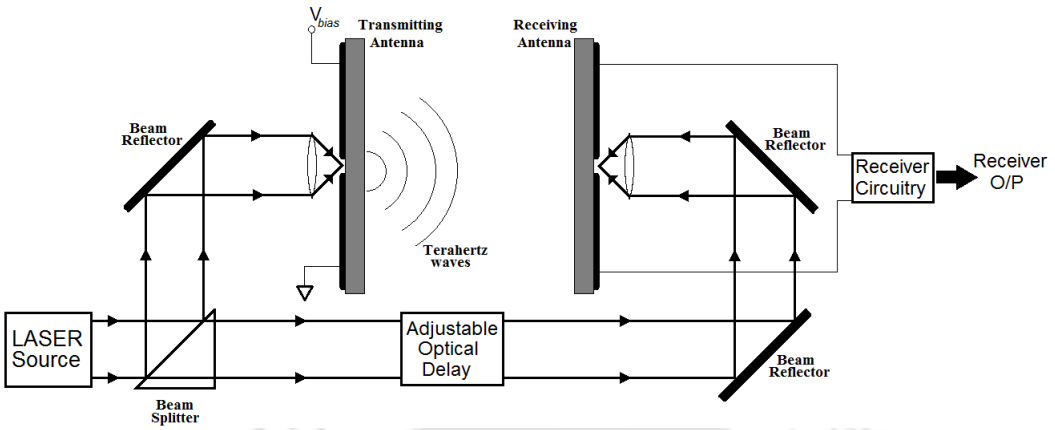

Figure 1.4: The Transmitter-Receiver set-up for experiments.

Use of optical heterodyning for emission of continuous wave THz emission have been reported in [21, 31] wherein the authors have demonstrated the use of interdigitated photomixers to emit continuous wave THz signals. Analytical treatment and optimization of THz PMA design have been carried out in [32]. The authors also carry out investigation of emission from different antenna geometries and find that antenna design dominates the output only upto a frequency of 0.6 THz, beyond which, the emission depends predominantly on the geometry of the active region. Advantages of using a continuous wave THz emitter over a pulsed type have also been highlighted. The factors that affect the optical to electrical power conversion efficiency has been discussed. The input impedance and the resonant frequency of a PCA has been discussed in [33, 34]. Due to the multi-physical phenomena involved in the operation of these antennas, the analytical model for evaluating the input impedance and resonant frequency differs from that of a conventional antenna and has to be evaluated for each antenna and its operating conditions. A comparison of the conventional RF/Microwave antenna technology with photoconductive antenna technology has been discussed in [35]. The authors have also presented expressions for the antenna efficiency which has been expressed as a product of three distinct efficiencies viz. laser-to-electrical power conversion, impedance matching and radiation efficiencies.

The accumulation of charge carriers near the electrodes of the antenna, sets up a screening electric field which directed opposite to the direction of the bias electric field. Another well-known phenomenon that occurs in accelerated motion of charged carriers is the carrier scattering due to collisions with neighbouring carriers and phonons. The screening electric field and

carrier scattering inherently limits the magnitude of current density on the antenna and therefore at higher optical fluences, a saturation effect is seen in the radiation from the photoconductive antenna. Investigation of the effect of screening electric filed and carrier scattering on the performance of the antenna has been discussed in [36, 37]. These studies have, however, been carried out for PCA and can be extended to the continuous wave PMA with some modification in the mathematical treatment. The radiated power from the THz PCA has been well studied as a function of the bias voltage, incident optical power, antenna geometry and other relevant parameters [38, 39].

One of the primary bottlenecks of THz PCAs and PMAs is their low efficiency (reportedly 0-1%). Several attempts at increasing the efficiency of these structures have been reported in literature. In [40,41], the authors present various factors that impact the overall efficiency of the PCA. On account of the similarities in the mechanism of operation, some of these factors are common in case of the efficiency of PMA as well. A comparison, however, of the two antenna technologies has been discussed in [42]. In order to have a clear understanding of the efficiency, a detailed model of the energy transformations in the PCA is necessary which can be obtained through an analytical model of the antenna, which has been attempted in [43, 44]. However, the model contained few inconsistencies which have been subsequently reported and improved upon in our recent work [45,46]. In [47,48], the authors attempt to model the photoconductance in the PCA and identify possible parameters that can be controlled in order to enhance the optical to electrical power conversion efficiencies. In [49], an interesting technique using steady magnetic field for increasing the amount of photocurrent and thereby the efficiency of the PCA has been reported.

1.4.1 Simulation of Photoconduction based antennas

Simulation of PCAs and PMAs in commercially available EM solvers have been limited due to two primary reasons. Firstly, due to the multi-physics involved in the operation of the photoconductive antenna, commercial EM solvers are not able to model such antennas accurately. Secondly, dispersive properties of a material that occur at THz frequencies cannot be specified in

most of these solvers [50] and therefore, the results produced would be unreliable. A few interesting ways to identify and work around the latter limitation have been reported [51,52] wherein the authors present intuitive boundary and constitutive parameter definitions which indirectly account for the dispersive nature of the materials at THz frequencies. However, owing to the internal solution subroutines of the commercial solvers, such results couldn't always be relied upon. The authors also present a comparative study about the prominent EM solvers used for THz band simulations. Owing to two aforesaid limitations, researchers have attempted to resort to the well-known and relatively easier-to-code method of solution, the Finite Domain Time Domain (FDTD) method for a computational solution of these novel antenna technologies [53,54]. Using the same procedure the authors have also investigated the other related aspects of the THz PCA [55,56] such as the influence of the different geometries of the electrode-gap, as shown in Figure 1.5 and 1.6, on the antenna performance. The 'Interdigitated' geometry in Figure 1.6 is, however, used in THz PMAs. An alternate method of solution of THz PCAs has been reported in [57] wherein the authors use the Fast-Fourier transform (FFT), of the time domain model of the generated photocurrent, and a full-wave simulation of the same antenna in a commercial EM solver to convolute the FFT of the photocurrent with the antenna transfer function and then find the radiated field of the antenna for the particular photocurrent.

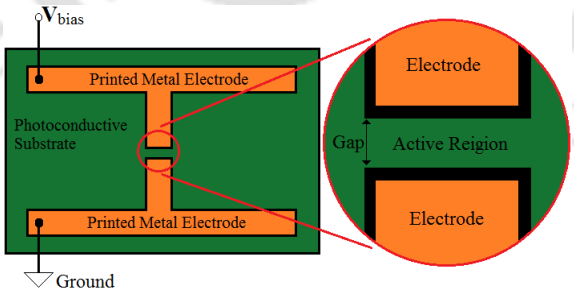

Figure 1.5: Basic PCA Electrode-gap geometry

1.4.2 Novel Materials for the THz band

As discussed earlier, after its discovery, Graphene [22] has shown lot of potential applications in several important areas owing to its remarkable physical, mechanical and electrical

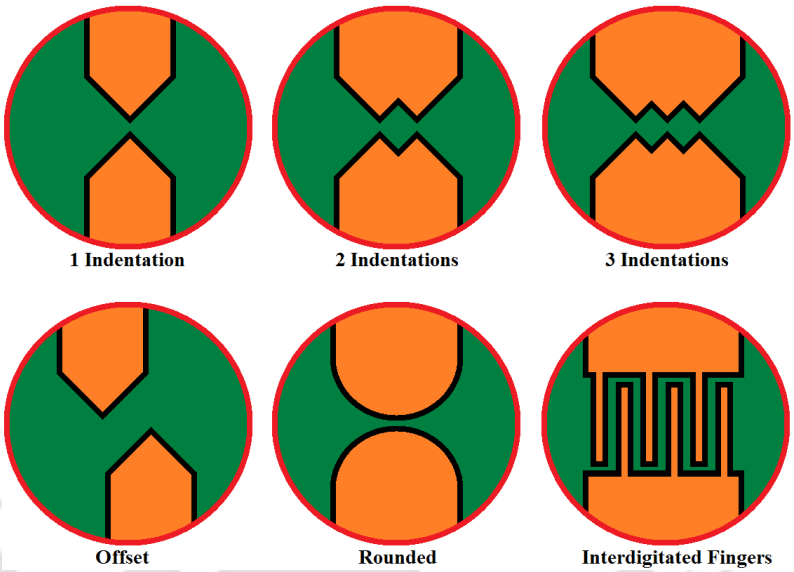

Figure 1.6: Other studied electrode-gap geometries

properties. Use of Graphene in antenna applications is, however, a relatively new direction [58] with the advent of micro and nano sized antennas based on Graphene, "Graphenna" [15, 59]. Especially at the THz band, the main advantages of Graphene over metals for antenna applications are: (a) Graphene supports transverse magnetic (TM) resonant surface plasmon polariton (SPP) modes even at lower THz frequencies unlike their metallic counterparts [60], (b) the electron mobility in Graphene, even at nano-dimensions is about 10^5 times higher than that in copper [61], (c) the current carrying capacity of Graphene is almost 2-3 orders of magnitude higher than metals, (d) the electrical characteristics of Graphene can be varied dynamically presenting potential for plethora of applications. Antennas based on Graphene are still within the research phase and little or no measurement data, especially at the THz band, are available.

Due to the lack of efficient THz signal sources, in recent years, investigations into feeding techniques for "Graphennas" [62] [63] have gained impetus. Literature reports the application of THz Photoconductive antenna (PCA) mechanism to feed a Graphenna. However, to the best of our knowledge little or no literature exists for the application of THz PMA to excite a Graphenna. PCAs and PMAs are essentially THz sources and do not require separate THz signal generators.

1.5 Motivation and Problem Formulation

From the preceding discussion, it has been realised that there is still a persistent need of efficient sources and antennas for THz band applications, especially from a perspective of wireless communication. The potential of the THz band of frequencies for wireless communication is immense and can be utilized beneficially with the availability of appropriate signal sources and channels. On the basis of the exhaustive survey of existing literature, we find that a lot of scope exists in proper analytical modelling and investigation of radiation from photoconductivity based THz antennas, especially PMAs, which would be a popular choices for THz band sources. Several issues related to antenna design for practical PMAs are still being investigated in the research community. In the present research endeavour, we would direct our attention more towards the topics related to the modelling and analysis of THz band PMAs, and also look into study and application of Graphene in relation to antennas in the THz and the ISM band. The following topics, which have surfaced from a voracious review of existing literature, shall be taken up for a detailed investigation in subsequent works:

- Investigation of the issues and limitations of the conventional microstrip antenna technology to be used for THz band applications
- Analytical modelling of carrier generation and current density in THz band PMAs .
- Analytical investigation of radiation from THz PMAs.
- Investigations on Graphene and its applications to the antenna technology.

The above list is, however, an abridged form of the actual content of the present research work which shall be discussed in more detail in the subsequent chapters of the thesis. In the subsequent sections, we present a gist of the contributions of this thesis and its organization.

1.6 Major Thesis Contributions

In a broad sense, the contributions of the present research endeavour can be listed as follows:

- Investigated the issues that arise in extending microstrip antenna design-practices at THz frequencies.
- Analytical model for carrier generation and conductance of PMAs.
- Derivation of Expressions for the current density and the radiated fields from a PMA.
- Application of Graphene to THz band and low frequency antennas and systems.
- Extraction of GNPs from Graphite and preparation of GNP based conductive ink.
- Fabrication and measurement of GNP based ISM band antenna.

1.7 Thesis Organization

The thesis is organized in six chapters. The content of individual chapters are detailed below:

In Chapter 1 we provide a general introduction on the THz frequency band and discuss the significance and potential applications of this frequency band. We present a review of the relevant literature and emphasize on the motivation and the problem statement of the research work presented in this thesis. We highlight the major contributions of this research endeavour and, in conclusion, describe the organization and outline the individual chapters in this thesis.

In Chapter 2, we highlight the issues and limitations of the conventional microstrip antenna technology and the contemporary commercially available materials when desired for use at THz frequencies. We present an analysis of conductor properties at THz and the highest frequency of reliable operation that can be designed with commercially available materials. We also discuss some of the limitations of the commercial EM solvers in performing THz band simulations.

In Chapter 3, we introduce an alternate, simple and generalized analytical model for radiation from a PMA which combines the multiphysical phenomena occurring in the operation of the PMA. We discuss, in detail, ways to produce modulation in the output of a PMA. We also introduce various factors that influence the efficiency of the PMA.

In Chapter 4, we discuss Graphene, its characteristics and application to the existing antenna technology. We propose a basic microstrip transmission line with Graphene, as a switch to control the signal flow, and a semi-circular antenna design with Graphene as a coplanar juxtaposed element to control the radiation characteristics of the antenna. We propose antenna array design using Graphene as a switch in a hybrid coupler to cause various phase shifts between the antenna elements and discuss it in Appendix B.

In Chapter 5, we investigate and analyse the application of Graphene in a THz PMA and extend our earlier analysis to model this antenna and the radiated fields as well. We discuss the advantages of using Graphene over metals at THz frequencies. We discuss techniques of extraction of Graphene nano-particles (GNP) from commercially available Graphite. We present material characterization results of the extracted GNPs and also investigate optimal techniques of preparation of GNP based conductive inks. These inks can also be made inkjet printable which can be used in a commercial inkjet printer to print conductive patterns on paper. However, we introduce an alternate and low cost method of forming conductive patterns on paper which we have used to design an ISM band antenna on a paper substrate. We fabricate the antenna and also measure it and present the return loss of this GNP based antenna Appendix C.

In Chapter 6, we conclude our investigations and highlight multiple potential directions for future research work.

2

Microstrip Design Issues at THz Frequencies

In this Chapter, we revisit the topic of constitutive parameters of material media and generalize the definitions of these parameters to understand the dispersion behaviour of materials at THz frequencies and possibly identify new physical phenomena that might occur at THz frequencies. With the aid of this discussion, we highlight the implicit limitations of commercial EM solvers in dealing with assuming material parameters suitably, for THz band simulations, which limits the reliability of results produced from such simulations. We discuss ways to get around these limitations reported in literature. We plot the constitutive parameters at THz frequencies for commonly used metals using the analytical model.

In the subsequent part of the chapter, we investigate the feasibility of practical implementation of a rectangular microstrip antenna (RMSA), reported in literature, at THz frequency band. We highlight the issues with the design of RMSA at THz frequencies and also present results of our simulations of two RMSA, one fed at the edge and the other fed inset.

2.1 Material Characterization at Terahertz Frequencies

In the general sense, matter is characterized in terms of three main parameters: permittivity 'ϵ', permeability 'μ' and conductivity 'σ'. Materials with large values of σ are termed as conductors and those with low values of σ are termed as semiconductors or insulators. For perfect conductors, $\sigma = \infty$ and for perfect dielectrics $\sigma = 0$. The permittivity parameter 'ϵ' of a material signifies its ability to capture electric fields within itself. The ratio $\frac{\epsilon}{\epsilon_0}$ is termed as the relative permittivity or dielectric constant of the material; where the parameter ϵ_0 is the permittivity of vacuum. Although meta-materials have been engineered to have desired values of dielectric constants, yet no naturally occurring matter having dielectric constant smaller than unity has been discovered so far. The dielectric constant of good conductors is unity. In case of most linear matter, the inductivity or the permeability parameter μ is approximately equal to that of free space inductivity 'μ_0'. The ratio $\frac{\mu}{\mu_0} = \mu_r$ is called the relative inductivity or the relative permeability of the material. For diamagnetic material $\frac{\mu}{\mu_0} \simeq 0.01\%$; for paramagnetic material '$\mu_r \geq 1$'. Ferromagnetic materials are non linear materials which have relative inductivity much greater than unity. In general, materials other than ferromagnetic materials are treated as non

magnetic and their relative inductivity is approximated to be equal to unity for the convenience of analysis.

In case of general linear matter in an electromagnetic field, we can write the constitutive relations as follows [64]:

$$\overrightarrow{D} = \epsilon_0 \cdot \overrightarrow{E} + \epsilon_1 \cdot \frac{\partial}{\partial t}\overrightarrow{E} + \epsilon_2 \cdot \frac{\partial^2}{\partial t^2}\overrightarrow{E} + \cdots \tag{2.1}$$

$$\overrightarrow{B} = \mu_0 \cdot \overrightarrow{H} + \mu_1 \cdot \frac{\partial}{\partial t}\overrightarrow{H} + \mu_2 \cdot \frac{\partial^2}{\partial t^2}\overrightarrow{H} + \cdots \tag{2.2}$$

$$\overrightarrow{J} = \sigma_0 \cdot \overrightarrow{E} + \sigma_1 \cdot \frac{\partial}{\partial t}\overrightarrow{E} + \sigma_2 \cdot \frac{\partial^2}{\partial t^2}\overrightarrow{E} + \cdots \tag{2.3}$$

where $\overrightarrow{E}\,\overrightarrow{H}$ represent general time varying electric and magnetic fields, respectively, and $\epsilon_n, \mu_n, \sigma_n$ are weights of higher order terms in Equations (2.1),(2.2) and (2.3). For time-harmonic electromagnetic fields with an angular velocity of ω rad/sec, the above equations may be written as:

$$\overrightarrow{D}(\omega) = \epsilon_0 \cdot \overrightarrow{E} + j\omega\epsilon_1\overrightarrow{E} + (j\omega)^2\epsilon_2\overrightarrow{E} + \cdots \tag{2.4}$$

$$\overrightarrow{B}(\omega) = \mu_0 \cdot \overrightarrow{H} + j\omega\mu_1\overrightarrow{H} + (j\omega)^2\mu_2\overrightarrow{H} + \cdots \tag{2.5}$$

$$\overrightarrow{J}(\omega) = \sigma_0 \cdot \overrightarrow{E} + j\omega\sigma_1\overrightarrow{E} + (j\omega)^2\sigma_2\overrightarrow{E} + \cdots \tag{2.6}$$

We segregate the real and imaginary parts in the above equations and rewrite them as follows:

$$\overrightarrow{D}(\omega) = (\epsilon'(\omega) - j\epsilon''(\omega))\overrightarrow{E} \tag{2.7}$$

$$\overrightarrow{B}(\omega) = (\mu'(\omega) - j\mu''(\omega))\overrightarrow{H} \tag{2.8}$$

$$\overrightarrow{J}(\omega) = (\sigma'(\omega) - j\sigma''(\omega))\overrightarrow{E} \tag{2.9}$$

As evident, both real and imaginary parts are functions of frequency. The value of the bulk conductivity of a material is an important parameter that determines its behaviour in an electromagnetic field. In the next section, we discuss the intrinsic bulk conductivity of materials.

2.2 Intrinsic Bulk Conductivity Model

The bulk conductivity of a material determines the nature of the nature of EM wave propagation in the material. Using Equations (2.7), (2.8) and (2.9) in Maxwell's equation, we can write:

$$\begin{aligned}\nabla \times \overrightarrow{H} &= [(\sigma'(\omega) + \omega\epsilon''(\omega)) - j(\sigma''(\omega) - \omega\epsilon'(\omega))]\overrightarrow{E} \\ &= [\sigma'_{eff}(\omega) - j\sigma''_{eff}(\omega)]\overrightarrow{E} \\ &= j\omega[(\epsilon'(\omega) - \frac{\sigma''(\omega)}{\omega}) - j(\epsilon''(\omega) + \frac{\sigma'(\omega)}{\omega})]\overrightarrow{E} \\ &= j\omega[\epsilon'_{eff}(\omega) - j\epsilon''_{eff}(\omega)]\overrightarrow{E} \\ &= j\omega\epsilon_0[\epsilon'_{r,eff}(\omega) - j\epsilon''_{r,eff}(\omega)]\overrightarrow{E}\end{aligned} \tag{2.10}$$

From the 2^{nd} and 5^{th} steps in the above simplifications, we can write:

$$\sigma_{eff}(\omega) = j\omega\epsilon_0\epsilon_{r,eff}(\omega) \tag{2.11}$$

where

$$\sigma_{eff}(\omega) = \sigma'_{eff}(\omega) - j\sigma''_{eff}(\omega) \tag{2.12a}$$

$$\epsilon_{r,eff}(\omega) = \epsilon'_{r,eff}(\omega) - j\epsilon''_{r,eff}(\omega) \tag{2.12b}$$

An accurate model of the behaviour of the frequency dispersion in normal materials is given by the Classical Relaxation Effect (CRE) model. In this model, the intrinsic bulk conductivity of normal metals at room temperature is given by [50]:

$$\begin{aligned}\sigma(\omega) &= \frac{\sigma(\omega = 0)}{1 + j\omega\tau} \\ &= (\frac{\sigma(\omega = 0)}{1 + \omega^2\tau^2}) - j(\frac{\omega\tau\sigma(\omega = 0)}{1 + \omega^2\tau^2}) \\ &= \sigma'(\omega) - j\sigma''(\omega)\end{aligned} \tag{2.13}$$

where τ is the scattering (or, relaxation) time for free electrons in the metal (i.e. mean time between collisions).

In commercial EM solvers such as HFSS^{TM} and CST-MWS^{TM}, two other models are employed which are indeed simplified versions of the CRE model viz.: the "simple relaxation effect model" and the "classical skin effect model". The simple relaxation effect model does not take into account the imaginary part $\sigma''(\omega)$ of the CRE model in Equation (2.13). The classical skin effect model takes only the DC intrinsic bulk conductivity $\sigma(\omega = 0)$ into consideration. Thus using both these approximate models at higher frequencies may lead to inaccurate results. Further, both the EM solvers do not provide means to directly provide user defined complex intrinsic bulk conductivity values into the solver. Although the software accepts complex values, but during solution process the imaginary part of the values are ignored leading to inaccurate results.

In order to incorporate the CRE model into HFSS^{TM}, [50] came up with a logical way, termed as the "effective relaxation effect model", in which the imaginary part of the complex conductivity is entered along with the real part of the complex effective dielectric constant using Equation (2.11) as follows:

$$\epsilon'_{r,eff}(\omega) = 1 - \frac{\sigma''(\omega)}{\omega\epsilon_0} \tag{2.14}$$

Using Equations (2.10),(2.11) and (2.12), we can write the expressions for the effective permittivity $\epsilon_{eff}(\omega)$ and the loss tangent $tan\delta_e(\omega)$ as [52]:

$$\epsilon_{eff}(\omega) = \epsilon'_{eff}(\omega)(1 - jtan\delta_e(\omega)) \tag{2.15}$$

$$tan\delta_e(\omega) \equiv \frac{\epsilon''_{r,eff}(\omega)}{\epsilon'_{r,eff}(\omega)} = \frac{\sigma'_{eff}(\omega)}{\sigma''_{eff}(\omega)} \tag{2.16}$$

2.3 Surface Impedance and Skin Depth Calculations

In general, the characteristic impedance (for eg. surface impedance of a metal Z_s) of a material is defined as:

$$\eta = \sqrt{\frac{\mu(\omega)}{\epsilon_{eff}(\omega)}} = \sqrt{\frac{j\omega\mu(\omega)}{\sigma_{eff}(\omega)}} = \sqrt{\frac{j\omega\mu(\omega)}{\sigma(\omega) + j\omega\epsilon(\omega)}} \equiv Z_s \tag{2.17}$$

where $\mu(\omega) = \mu'(\omega) - j\mu''(\omega)$ and $\epsilon_{eff}(\omega)$ has been defined in Equation (2.11). With normal materials, the frequency dispersion in magnetization can be neglected such that $\mu'(\omega) = \mu_0\mu'_r$ and $\mu''(\omega) = 0$. At terahertz frequencies, $\mu'_r \sim 1$ [52]. If the conductivity of the metal is assumed to be sufficiently high such that $\sigma_{eff} \cong \sigma(\omega)$, Equation (2.17) can be written as:

$$Z_s = R_s + jX_s = \sqrt{\frac{j\omega\mu_0\mu'_r}{\sigma(\omega)}} \tag{2.18}$$

Using the CRE model mentioned above, we calculate the surface impedance and skin depth as follows [50]:

$$Z_s(\omega) = \sqrt{\frac{j\omega\mu_0\mu'_r}{\sigma(\omega = 0)}}\sqrt{1 + j\omega\tau} \tag{2.19}$$

Skin Depth:

$$\begin{aligned}\delta_s &= \frac{1}{\text{Attenuation Constant}, \alpha_s} \\ &= \sqrt{\frac{2}{\omega\mu_0\mu'_r\sigma(\omega = 0)}}\sqrt{1 + \omega^2\tau^2}\sqrt{\sqrt{1 + \omega^2\tau^2} - \omega\tau}\end{aligned} \tag{2.20}$$

For typical metals such as Gold, Silver, Copper and Aluminium, the value of scattering life-time τ is of the order of 10^{-15} seconds. Using the above relations, we can calculate the intrinsic bulk conductivity, effective dielectric constant and surface impedance from the CRE model and incorporate the calculated values as user-defined inputs into the EM solvers for THz band simulations.

2.4 Plots of THz material parameters

Below we show the variation of the effective bulk conductivity, effective dielectric constant and loss tangent of four metals calculated on the basis of CRE model at terahertz frequencies:

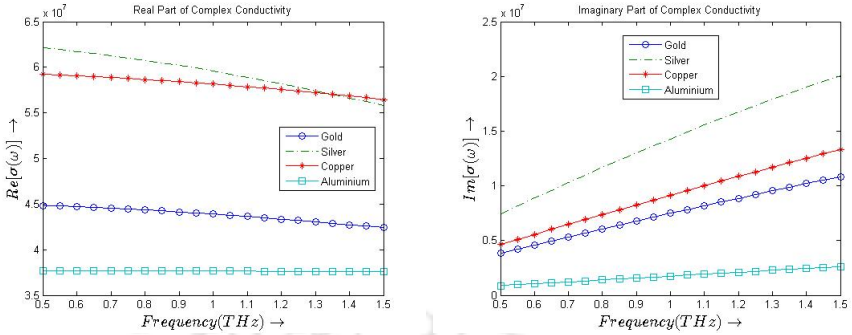

Figure 2.1: Real and Imaginary Parts of Complex Intrinsic Bulk Conductivity

In the plots, we can clearly see the increase of the imaginary part of the conductivity with frequency. Therefore at higher frequencies such as THz, neglecting the imaginary part of the conductivity in simulations could yield unreliable results. The increase in the imaginary part of the conductivity contributes to the real part of the effective dielectric constant and the loss tangent which are shown in the figures below:

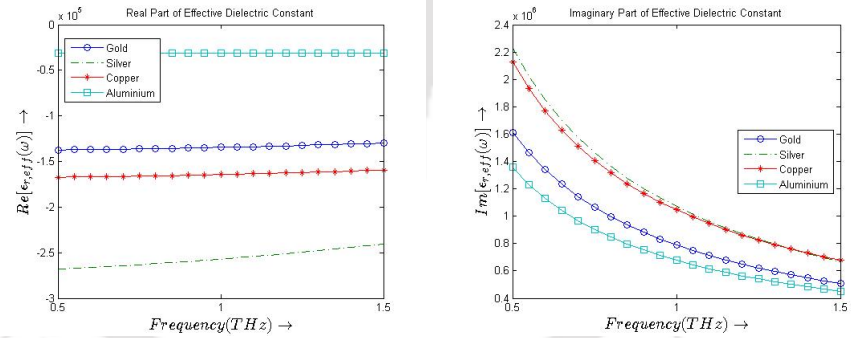

Figure 2.2: Real and Imaginary Parts of Complex Effective Dielectric Constant

One important point to note here is that practical measurements on the electromagnetic fields, yield the effective values of the constitutive parameters from which the absolute parameters need to be derived using the equations presented above.

2.5 Rectangular Microstrip Antenna at Terahertz Frequency

Since the ambit of terahertz frequency overlaps with the microwave and visible-optics regions, an extension of the antenna technology in the either of the two bounding regions would a plausible idea. Intuitively, RMSA with microstrip feed, which have proved to be successful

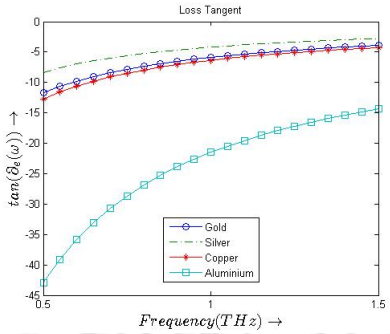

Figure 2.3: Loss Tangent

radiators in the millimeter wave region, can be scaled appropriately to be used as antennas at sub-millimeter wavelengths. Recent works [65] show the simulation results of RMSAs on commercially available substrates for a frequency range of 0.7-0.85 THz. The substrate used for the simulation is Rogers RT/Duroid 6006 substrate with a dielectric constant of 6.15 and a loss tangent of 0.0019. Before proceeding to design considerations of RMSAs in the sub-millimeter wave region, let us first revisit the basic structure and principle of operation of a RMSA.

2.6 Basic Structure and Operation of RMSA

A RMSA, in its most basic form, consists of a rectangular metallic patch printed onto a dielectric substrate with a ground plane printed onto the other side of the substrate as shown in Figure (2.4) below. 'L' and 'W' are the length and the width of the microstrip patch respectively. As shown in the Figure, the height of the dielectric substrate is 'h' and the thickness of

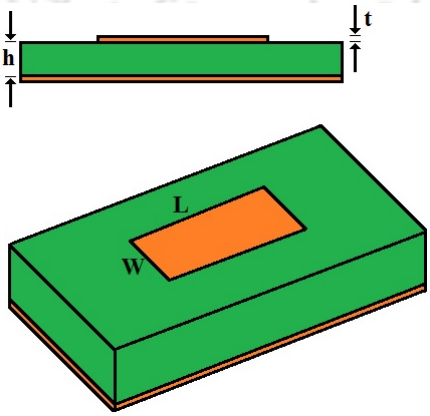

Figure 2.4: Basic Structure of RMSA

the metallization is 't'.Several feeding techniques to excite the RMSA have already been well discussed in literature [66]. Also, analytical modelling and standard design procedure for a RMSA have also been formulated.

The length 'L' of a RMSA is determined by the desired resonant frequency for which the RMSA is designed. The width 'W' of the RMSA, however, mainly determines the gain, bandwidth and the input impedance of the antenna. The bandwidth of the RMSA is inversely proportional to the square-root of the dielectric constant of the substrate. Therefore a thick substrate with low dielectric constant is usually preferred to obtain a wider bandwidth. The RMSA can be, in other terms, visualized as $\frac{\lambda}{2}$ section of a wide microstrip line. At a particular instant of time the field distribution for the fundamental TM_{10} mode in the patch is given as shown in the Figure (2.5) below. In the next half cycle of operation, the fringing fields will invert their

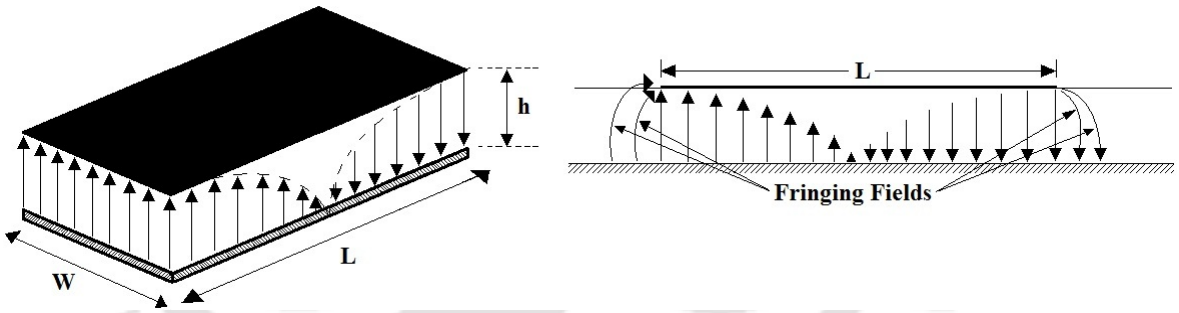

Figure 2.5: TM_{10} mode field configuration in the RMSA [64] [67]

direction. If the fringing fields are decomposed into their vertical and horizontal components in a rectangular coordinate system, we observe that the vertical components are always opposite in direction to each other and hence cancel out. However, the horizontal components are parallel at all instants but only vary in magnitude. This change in the fields cause radiation from a RMSA. Thus, in effect, the radiation from the RMSA can be visualized as due to two narrow radiating slots/windows along its width 'W' as shown in the Figure (2.6).

2.7 Design Considerations for RMSA

Conventional RMSA design has been standardized for the microwave frequency range of upto a few tens of Gigahertz where the designed RMSA performs desirably. The different

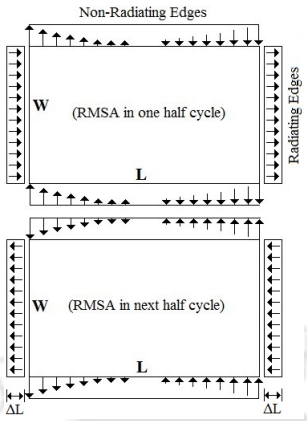

Figure 2.6: Radiating and Non-radiating edges in RMSA

design parameters for the RMSA are discussed below.

2.7.1 Substrate selection

The first and one of the crucial steps in any microstrip antenna design is the choice of proper antenna substrate. The substrate in any microstrip antenna is provided to offer mechanical support to the antenna element. The presence of the substrate beneath the patch metallization affects the radiation properties as well as the input impedance of the antenna. Thus a substrate material which satisfies both the electrical as well as the mechanical requirement criteria has to appropriately chosen. The dielectric constant of the substrate ϵ_r is an important parameter in that determines the dimensions of the microstrip antenna.

Once a proper substrate is selected, the first step is to determine the effective dielectric constant ϵ_{eff} of the microstrip configuration with the selected substrate. This quantity is of extreme importance due to the fact that the fringing fields at the microstrip edges do not entirely lie in the dielectric substrate and a portion of these fields lie in the air medium. The effective dielectric constant expression for the RMSA structure is an empirical relation given by [68]:

$$\epsilon_{eff} = (\frac{\epsilon_r + 1}{2}) + (\frac{\epsilon_r - 1}{2})[\sqrt{\frac{W}{W + 12h}}] \tag{2.21}$$

Here the RMSA width 'W' is determined using Equation (2.22).The above equation for determination of effective dielectric constant is valid for $\frac{W}{h} > 1$.

2.7.2 RMSA Dimensions

The width and length of RMSA patch element required to resonate at a frequency f_r is calculated using the following equations:

$$W = \frac{c}{2f_r\sqrt{\frac{\epsilon_r+1}{2}}} \tag{2.22}$$

$$L = L_e - 2\Delta L \tag{2.23}$$

In Equation (2.22), 'c' is the velocity of electromagnetic waves in free space. Fringing of the electric field lines along the edges of the patch causes the effective length of the microstrip patch to be apparently longer than physical length of the patch on both the radiating edges. The quantity L_e is, hence, the effective length of radiating patch which determines the resonant frequency f_r and so has to be equal to half of the wavelength corresponding to f_r in the substrate. The value of the effective length is the given by:

$$L_e = \frac{c}{2f_r\sqrt{\epsilon_{eff}}} \tag{2.24}$$

The quantity $2\Delta L$ is the total extension in the physical length due to the fringing fields on both the radiating edges. This extension depends on the width-to-height ratio of the substrate and is calculated using Equation (2.25).The actual length of the designed RMSA is, hence, the shortened by $2\Delta L$.

$$\frac{\Delta L}{h} = 0.412 \cdot \frac{(\epsilon_{eff}+0.3)}{(\epsilon_{eff}-0.258)} \cdot \frac{(W+0.264h)}{(W+0.8h)} \tag{2.25}$$

2.8 Issues at Terahertz Frequencies

The above standard design procedure gives RMSAs with desired performance with an error as low as ±1.2% [66]. Although the above procedure gives desired antenna performance upto few tens of gigahertz, as the frequency is increased to few hundreds of gigahertz, several issues have to be further considered for a RMSA design and the design considerations become more subtle and counter-intuitive. We discuss the different design considerations to be taken care of

for design of RMSAs at higher frequencies below.

2.8.1 Substrate Selection

A careful selection of substrate with appropriate dielectric constant is crucial at higher frequencies of the order of THz (10^{12}Hz). The dielectric constant of the substrate material stated in the data-sheet of the material is often the one measured within a frequency range of 10Ghz-40GHz at room temperature. Hence, using such a substrate for antenna design at resonance frequencies more than 40GHz would give erroneous results in practice, although simulation results would show no effect because the validity of the value of ϵ_r is not checked in any of the commercially available EM Solvers (HFSS^{TM}, CST-MWS^{TM} etc.). In [65], the author uses the value of $\epsilon_r = 6.15$ for RT/Duroid 6006 in their design at a resonant frequency of 742.15GHz. However, this value of ϵ_r is measured at 10 GHz, 23^oC as per standard data-sheets from Rogers Corporation. As per the data-sheet of RT/Duroid 6006, the measured dielectric constant in the range from 8 GHz-40 GHz is $\epsilon_r = 6.45$ which is still lower than the desired resonant frequency of the RMSA thereby bringing potential uncertainty in the simulated results.

RT/Duroid 6006 laminates are Ceramic-PTFE composites designed for electronic and microwave circuit applications requiring a high dielectric constant. In [69] [70], PTFE has been found to have almost constant values of $\epsilon_r = 2.06$ and $tan\delta_e = 0.0004$ upto a a frequency of about 3THz as shown in Figure(2.7). However, Rogers Co. does not provide any data

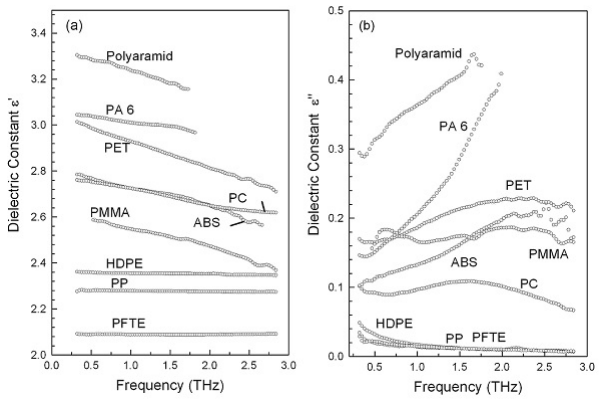

Figure 2.7: ϵ_r and $tan\delta_e$ of PTFE at Terahertz Frequencies [69]

for Ceramic-PTFE composites at higher frequencies than 40GHz. So use of Ceramic-PTFE composites for antenna design at higher frequencies are prone to uncertain practical performance. [70], for the first time, characterizes few high frequency laminates (RO3003,RO3006 and RO3010) manufactured by Rogers Co. and reports that due to high ceramic filling and possible void spaces in the material the dielectric constant as well as the loss tangent values of these ceramic-PTFE composites are high at high frequencies. Figure (2.8) shows their results: Therefore, the choice of substrate material should be such that the values of ϵ_r and $tan\delta_e$ are

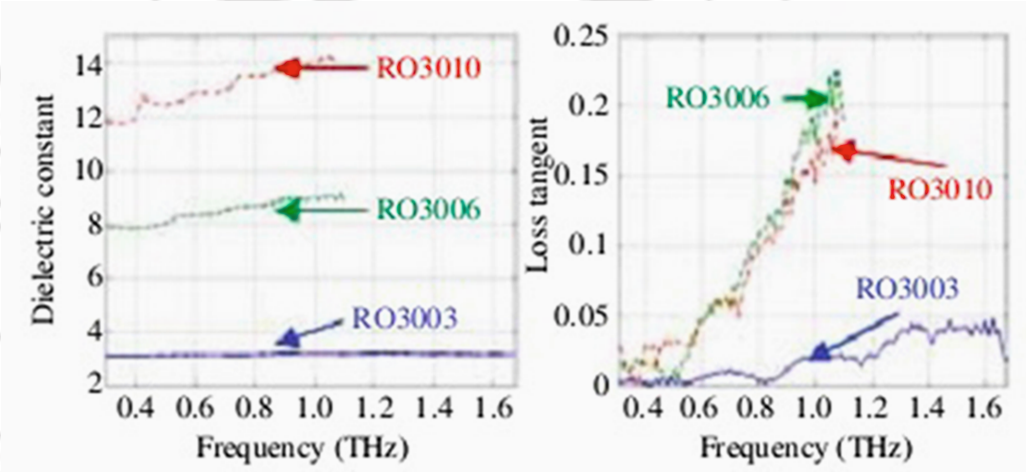

Figure 2.8: ϵ_r and $tan\delta_e$ of RO3003,RO3006 and RO3010 at Terahertz Frequencies [70]

available at/around the desired design frequency of the antenna. If the values of ϵ_r and $tan\delta_e$ are frequency dependent, care has to be adopted to provide these values to the EM Solver at the time simulations. Most of the commercial EM solvers allow user defined data entries to be adopted during simulations.

2.9 Height of the substrate of the RMSA

As the height of the substrate increases, the fringing of the fields from the edges increase. This increase in the fringing effect increases the length extension, ΔL and the effective length L_e, which decreases the resonance frequency for the dominant TM_{10} mode. On the other hand, as 'h' increases, the $\frac{W}{h}$ ratio reduces, which reduces ϵ_{eff} and hence increases the resonance frequency. However, the effect of the increase in ΔL on the change in the resonant frequency is

Table 2.1: Details of Rogers High Frequency Laminates

Dielectric Materials	ϵ_r	$tan\delta$	**Thickness (mm)**	**Highest Operating Frequency (THz)**
RO 4730JXR	3.00	0.0033	0.780	0.1359
RO 4725JXR	2.55	0.0026	0.780	0.1442
RO 3210	10.80	0.0027	0.250	0.2468
RO 3206	6.60	0.0027	0.250	0.3076
RT/Duroid 6035HTC	3.60	0.0013	0.254	0.3891
RO 3203	3.02	0.0016	0.250	0.4229
RO 3010	11.20	0.0023	0.130	0.4669
RT/Duroid 5880LZ	1.96	0.0027	0.254	0.4851
RT/Duroid 6010.2LM	10.70	0.0023	0.127	0.4880
RO 4003C	3.55	0.0027	0.203	0.4896
RO 3006	6.50	0.0020	0.130	0.5954
RT/Duroid 6006	6.45	0.0027	0.127	0.6115
RO 3035	3.60	0.0017	0.130	0.7603
RO 3003	3.00	0.0013	0.130	0.8153
RT/Duroid 6002	2.94	0.0012	0.127	0.8409
RT/Duroid 6202	2.90	0.0015	0.127	0.8452
RT/Duroid 5870	2.33	0.0012	0.127	0.9147
RT/Duroid 5880	2.20	0.0009	0.127	0.9331
RO 4350B	3.66	0.0037	0.101	0.9723

dominant over that due to a reduction in ϵ_{eff}. Therefore, an increase in 'h' effectively reduces the resonant frequency of the RMSA. Using the discussion presented in [67], we can, in a way, determine an upper bound on the operating frequency of the RMSA, whilst being good radiator, for a given height of the substrate as follows: as mentioned earlier, Equation (2.21) is valid if the width-to-height ($\frac{W}{h}$) ratio is greater than unity. In the limiting case, i.e. when $\frac{W}{h} = 1$, we obtain the maximum resonating frequency for a given substrate material using Equation (2.22) as follows [67]:

$$f_{r,max} = \frac{c}{2h\sqrt{\frac{\epsilon_r+1}{2}}} \tag{2.26}$$

Clearly, thinner substrates would offer higher resonant frequencies. We use the smallest possible thickness given in the data-sheets of several High-Frequency laminates provided by Rogers Co. and calculate the upper bound on the operating frequency that can be obtained using that laminate. The results are shown in Table (2.1) below:

Table (2.1) is important because antenna designs carried out without due consideration of the upper limit of the resonant frequency may lead to designs which are not practically valid. For example, in [65], the author uses a 200μm thick dielectric RT/Duroid 6006 substrate with antenna dimensions of 600μm $\times$ 400μm. The following points are worth noting:

- As per Equation (2.26), for a chosen thickness, the upper bound on the operating frequency for a satisfactory operation is=0.3964 THz. However, simulation results by the author show resonance at 742.15 GHz. This discrepancy is not addressed by the author.
- If in case we assume the antenna to show a resonance at 742.15 GHz, the half-wavelength dimension which, in fact must be the effective length of the RMSA , is given by Equation (2.24) = 94.753μm. The physical length of the antenna, which when calculated using Equation (2.23), must be= -55.907μm. Clearly, this does not lead to a valid design.

2.10 Design of Coplanar Antenna Feed at Terahertz Frequencies

In conventional RMSAs designed at lower GHz frequencies, the width of a feed line, on a substrate with thickness 'h', with a given characteristic impedance Z_0 can be calculated using [71]:

$$\frac{W}{h} = \begin{cases} \frac{8e^A}{e^{2A}-2} & \frac{W}{h} < 2 \\ \frac{2}{\pi}[B - 1 - ln(2B-1) + \frac{\epsilon_r - 1}{2\epsilon_r}\{ln(B-1) + 0.39 - \frac{0.61}{\epsilon_r}\}] & \frac{W}{h} > 2 \end{cases} \tag{2.27}$$

Where the parameters A and B are given by:

$$A = \frac{Z_0}{60}\sqrt{\frac{\epsilon_r + 1}{2}} + \frac{\epsilon_r - 1}{\epsilon_r + 1}(0.23 + \frac{0.11}{\epsilon_r}) \tag{2.28}$$

$$B = \frac{377\pi}{2Z_0\sqrt{\epsilon_r}} \tag{2.29}$$

Conventionally, characteristic impedance of standard transmission line sources are generally 50Ω, 75Ω, 100Ω, 150Ω etc. At high frequencies in the order of THz, conventional feed design strategies for designing feed lines at lower characteristic impedances on commercially available high-frequency laminates lead to a condition where the width of the feed line almost approaches the width of the antenna or even more. For example, in order to design a standard 50Ω feed

line on RT/Duroid 6006(ϵ_r = 6.15), the width of the line on the commercially available 127μm substrate is 187.02μm. If we want to design a RMSA resonant at 0.6THz on this substrate, the width of the antenna is 132.13μm. Clearly, the width of the antenna is smaller than the width of the feed line thereby rendering the design ineffective. On the other hand, if we design a feed line at 100Ω on the same substrate, the width of the line is 7.52μm. Thus, at high frequencies, coplanar feeding is feasible at higher characteristic impedances. Further, a high impedance feed line can directly be edge-fed to the RMSA as the impedance at the edges of the patch is usually high.

Although the design of feed lines with lower characteristic impedances is difficult on commercially available substrates, custom made thinner substrate could always be used which are thinner than the commercially available ones. For example, width of a 50Ω line on a 10μm thick RT/Duroid 6006(ϵ_r = 6.15) substrate is around 15μm, which is well acceptable for RMSA design at 0.6THz.

2.11 Effect of Metallization Thickness

The thickness of metallization 't' in RMSA design is taken into consideration during calculation of effective width of the radiating edge of the patch antenna. The effective width of a patch is given by the following relations [67]:

$$W_e = \frac{2\pi h}{\ln[\frac{hF}{W'} + \sqrt{1 + (\frac{2h}{W'})^2}]} \tag{2.30}$$

where

$$F = 6 + (2\pi - 6)\exp\frac{-4\pi^2}{3}(\frac{h}{W'})^{\frac{3}{4}} \tag{2.31}$$

and

$$W' = W + (\frac{t}{\pi})[1 + \ln\{\frac{4}{\sqrt{(\frac{t}{h})^2 + \frac{(\frac{1}{\pi})^2}{(\frac{W}{t}+1.1)^2}}}\}] \tag{2.32}$$

Here W is the initial width of the patch calculated using Equation (2.22). The above equations are ±0.2% accurate for $0.01 \leq W/h \leq 100$ and $\epsilon_r \leq 50$. It can be easily predicted from Equation (2.32) that with increasing value of 't', the contribution from the second term in the

equation increases, signifying the effect of the metallization thickness in calculation of the effective patch width. For $\frac{t}{h} \sim 0$, we have $W' = W$ i.e. at very low values of metallization thickness, its effect can be ignored in the calculations.

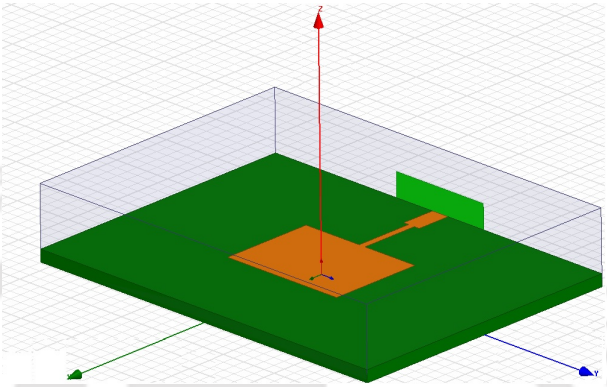

Figure 2.9: Geometry of the Edge-Fed Antenna

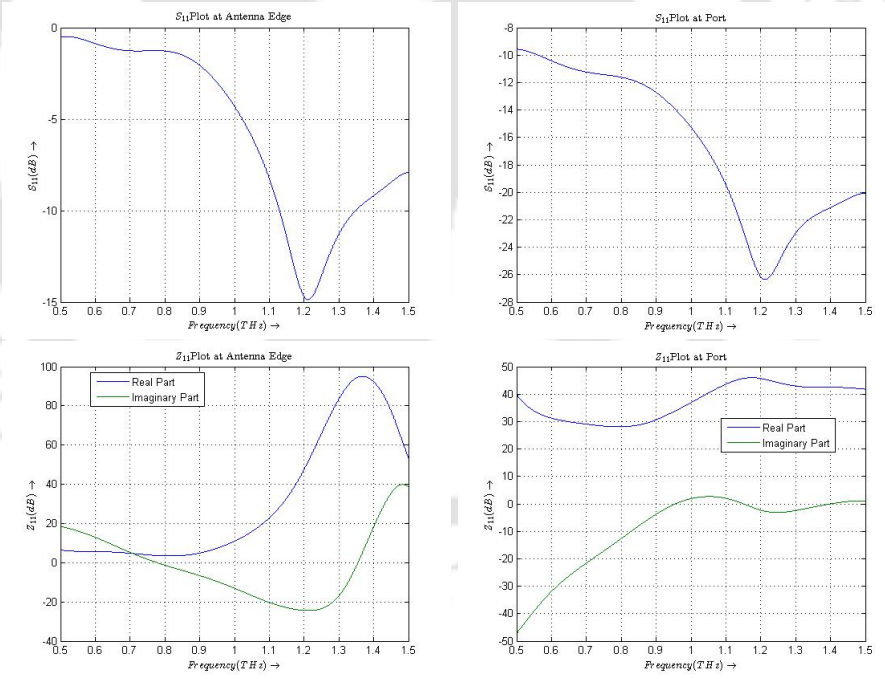

Figure 2.10: S-parameters and Z-parameters for the edge-fed antenna geometry

2.12 Simulation of Rectangular Microstrip Antenna

On the basic of the logical reasons forwarded in the preceding section, we try to design and simulate a RMSA with the following specifications:

- Resonant Frequency: 742.15GHz.

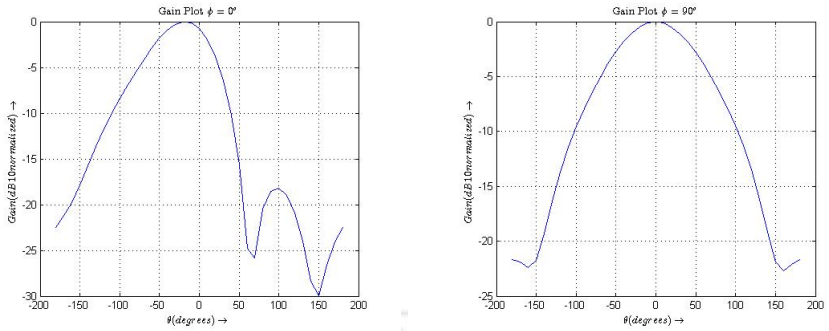

Figure 2.11: Gain Plots for the edge-fed antenna geometry

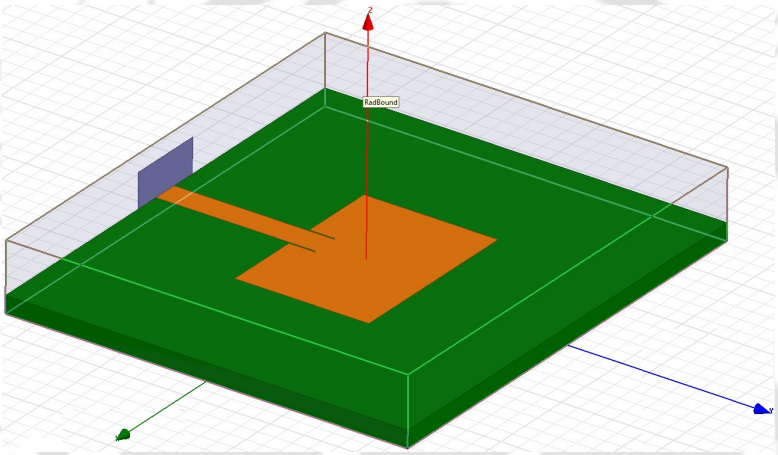

Figure 2.12: Geometry of the Inset Fed Antenna

- Substrate Material: RT/Duroid 6006.
- Substrate Dielectric Constant: 6.15.
- Width of Antenna: 106.896μm.
- Length of Antenna: 78.744μm.
- Width of substrate: 3 times antenna width.
- Length of Antenna substrate: 3 times antenna length.
- Height of Substrate: 10μm.
- Thickness of Metallization: 0.0025μm.
- Simulation Platform: HFSS^{TM} Version 15

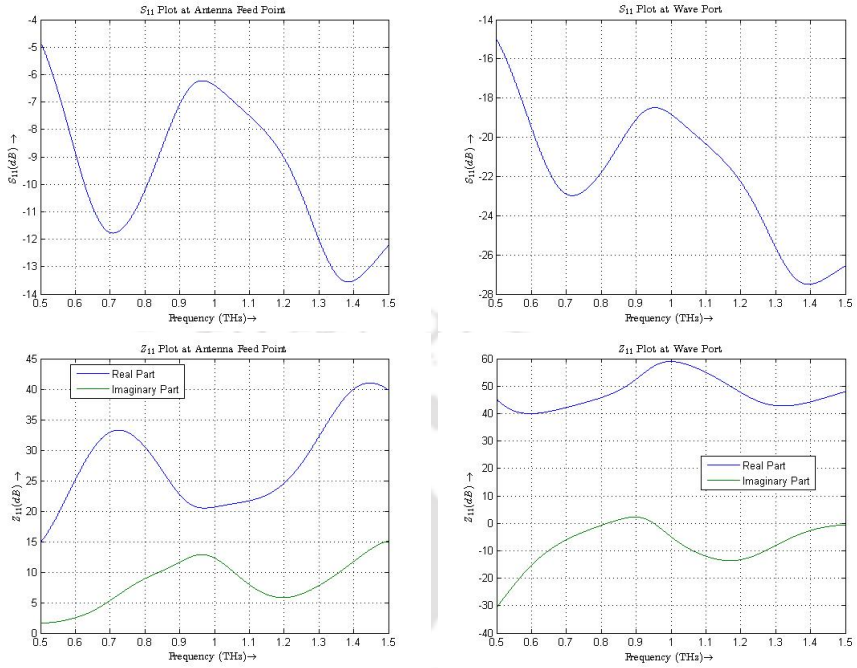

Figure 2.13: S-parameters and Z-parameters for the inset-fed antenna geometry

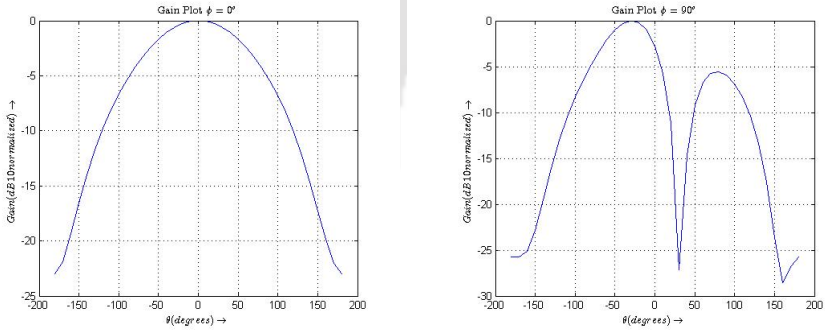

Figure 2.14: Gain Plots for the inset-fed antenna geometry

- Type of Feed: Wave Port.

We adopt two different feeding strategies: Edge feeding and Inset Feeding. The geometries of the antennas using the two feeds are shown in Figures 2.9 and 2.12 respectively. In the next section, we present the results of simulating these two antenna geometry and also discuss the inferences.

2.13 Edge and Inset Fed Antenna Simulations

From the various plots, it can be clearly seen that impedance matching at high frequencies is quite difficult and new strategies have to be improvised for a good match. The gain of the antenna is low although it shows resonant behaviour. From the Z_{11} parameter plots, it is evident that the antenna is exhibiting a series R-L-C resonant circuit behaviour with the reactive part crossing over from capacitive to inductive at resonance.

2.14 Conclusion

In this chapter, we have presented a revisit on the constitutive relations of matter and generalize them to be suitable for extension to the THz frequency band as well. We also discuss the issues regarding implementation of microstrip antenna technology at THz band.

3

Terahertz Photomixing Antenna

In this chapter, we introduce and discuss an alternate and simple generalized electromagnetic wave based model of THz radiation from PMAs combining a basic 2-ray model, semiconductor device physics and EM model. We derive analytical expressions that model the current densities set-up in the antenna and deduce expressions for radiated fields due to these currents. Extending our analytical model, we further introduce and investigate a technique for producing signal modulation in the PMA to make it suitable for application in wireless communications. We compare the results obtained from our model with available measured results, reported in literature, and find reasonably close agreements.

In the rise of novel materials, suitable for THz applications, Graphene has been identified as a potential choice for antenna applications in the THz band. We present a basic introduction to Graphene and its characteristics in Chapter 4. Due its preferability for THz applications, we extend the analysis presented in this chapter and propose a novel Graphene based PMA in Chapter 5 and present useful simulation results of the PMA therein.

3.1 Motivation

As highlighted in Chapter 1, THz PMAs are amongst the promising devices that can generate CW radiation in the THz frequency range. The popularity of PMAs, from a wireless communication perspective, can be attributed to the two facts that no separate signal generators are required for obtaining The working principle of these antennas has been explained in detail in the subsequent section.

Although THz PMAs have been significantly investigated [21, 32, 72, 73], these analyses have, predominantly, dealt with equivalent circuit models of PMAs. An analytical model of radiated fields, incorporating the multi-physical phenomena, in the THz PMA has not been addressed adequately. Furthermore, the feasibility of signal modulation, which is an inextricable part of any communication link, on a THz PMA has not been investigated aptly. Signal modulation on a PMA is critical for the PMA to be suitable for wireless communications.

In the subsequent sections, we shall begin with an introduction to the basic geometry and operation of a PMA and then proceed to present its analytical model.

3.2 Geometry of Inter-digitated THz PMA

A conventional PMA geometry consists of metallic electrodes with inter-digitated pattern over a photoconductive substrate, most commonly Low-Temperature Grown Gallium Arsenide (LTG-GaAs) [74], as shown in Figure 3.1 below. For the purpose of our analysis, we show the geometry of a single finger in the inter-digitated structure of the PMA in the inset of Figure 3.1.

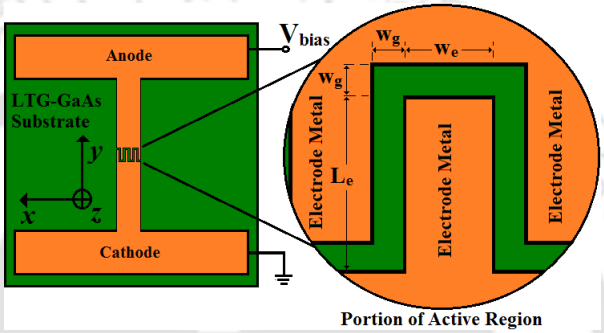

Figure 3.1: Geometry of a THz PMA. *(Inset)* Enlarged view of a portion of the active region.

The metallic electrodes are connected to a DC bias source (V_{bias}) which creates an electric field within the gaps of the inter-digitated fingers of the PMA. The minimum thickness of the LTG-GaAs substrate is determined by the maximum penetration depth of the laser wavelength in the material of the substrate. Usually, substrate thicker than the maximum penetration depth is used. Additionally, for collimation of the output radiation, a silicon lens is used on the rear side of the substrate, *i.e.* surface opposite to the one containing the electrodes [75].

3.3 Working Principle of PMA

The operation of a PMA utilizes the phenomenon of optical heterodyning. Two laser sources impinge onto the inter-digitated region of the PMA and give rise to electron-hole pairs, in the substrate, at the beat frequency which is the difference between the two incident laser frequencies. The region of the photoconducting substrate within the inter-digitated finger-gaps, uncovered by the metallic electrodes, is exposed to incident optical fluence and takes part in the carrier generation process. This region in the substrate is called the *active region* of the PMA. For N_e inter-digitated electrode fingers (anode + cathode fingers), assuming a laser penetration

depth of $L_{LTG-GaAs}$ ($\approx$ 1 μm at $\lambda \sim$ 800 nm), we find the volume of the active region in the substrate as

$$V = A \times L_{LTG-GaAs} = w_g L_{LTG-GaAs}(N_e w_e + (N_e - 1)(L_e + w_g)) \tag{3.1}$$

where A is the total surface area of the substrate which is illuminated by incident phonons. The total area of illumination being relatively small compared to a typical laser spot size, we assume a uniform illumination over the entire active region. The parts of the LTG-GaAs covered by metallic electrodes at the inter-digitated region would not be exposed to the illumination and we exclude these in the expression for A. The contributions from the corner regions, however, have been included in Equation (3.1). In case of very wide electrodes *i.e.* for $w_e/w_g \gg 1$, the contribution from the corners can be neglected.

The optically generated charge carriers, in the active region, are then accelerated due to the field generated by the application of V_{bias}. The acceleration of the charge carriers in the field gives rise to time varying currents densities. These time varying current densities at the active region in the PMA gives rise to the EM radiation from the PMA. Due to the presence of the substrate, which has $\epsilon_r > 1$ most of the radiated energy is directed into the substrate which then gets collimated by the use of a silicon lens as discussed above.

3.4 2-Ray Model of laser incidence

As discussed in the previous subsection, two above band-gap, continuous-wave (CW) and moderate-power laser beams, with average powers P_{L1} and P_{L2} respectively, are focused to illuminate the active region of the LTG-GaAs substrate. The angles of incidence (AOI) of the two beams are θ_1 and θ_2 respectively, as shown in Figure 3.2. The angular frequencies, $\omega_1 = 2\pi f_1$ and $\omega_2 = 2\pi f_2$, of the two laser sources, are chosen appropriately to produce a beat frequency in the THz region.

We assume the incident beams of the lasers at the point of incidence (z=0), to be plane waves, as used in the analysis of photodetectors [76]. We analyse two distinct cases in which we consider the beams to be linearly polarized: case (a) "normal" (s-polarized) and case (b)

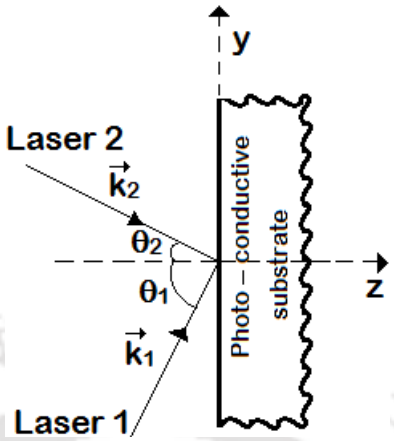

Figure 3.2: 2-Ray model for AOI of the two laser sources.

"parallel" (*p*-polarized) to the plane of incidence (*y*-*z* plane in Figure 3.2). Any arbitrary polarization may be expressed as an apt superposition of the above cases. For the cases (a) and (b), with respect to Figure 3.2, we obtain the following expressions for electric fields

$$\vec{E}_i^a = \hat{a}_x |\vec{E}_i^a| e^{j(i-1)\zeta} e^{-j|\vec{k}_i|((-1)^{(i-1)} y sin\theta_i + z cos\theta_i)} e^{j\omega_i t}; i = 1, 2 \tag{3.2}$$

$$\vec{E}_i^b = |\vec{E}_i^b|(-\hat{a}_y cos\theta_i + (-1)^{(i-1)} \hat{a}_z sin\theta_i) e^{j(i-1)\zeta} e^{-j|\vec{k}_i|((-1)^{(i-1)} y sin\theta_i + z cos\theta_i)} e^{j\omega_i t}; i = 1, 2 \tag{3.3}$$

For additional generalization, in the above equations, we include a relative phase difference of ζ between the laser beams. Also, $|\vec{k}_1|$ and $|\vec{k}_2|$, are the wave-numbers of the two laser sources. The *z-component* (with respect to Figure 3.2) of the Poynting vector determines the amount of the instantaneous optical power incident onto the photoconductor. The component of the Poynting vector parallel to the interface does not contribute to the carrier generation process and hence is not a part of the present model.

In both cases (a) and (b), using equations (3.2) and (3.3), we can calculate the instantaneous incident optical power density at the active region which results to the same expression, given as

$$P_{inc} = P_{L1} cos\theta_1 + P_{L2} cos\theta_2 + \sqrt{P_{L1} P_{L2}} (cos\theta_1 + cos\theta_2) cos(\omega t - y(|\vec{k}_1| sin\theta_1 + |\vec{k}_2| sin\theta_2) - \zeta) \tag{3.4}$$

The term ω in Equation (3.4) is the difference between the two laser angular frequencies, *i.e.* $\omega = |\omega_1 - \omega_2|$. The frequency of the term containing $(\omega_1 + \omega_2)$, obtained in optical heterodyning [76], would be too high to effectively modulate the carrier density of the photoconductive material and so, it has been dropped in Equation (3.4). Although the net electric and magnetic fields at the point of incidence would depend on the polarization of the incident beam, the average power incident onto the photoconductor surface is independent of the polarization.

The radiated electric and magnetic fields from the PMA involves equations (3.2) and (3.3). The and are presented in Section 3.9.

3.5 Formulation of the Carrier Concentration and Conductance

The charge carrier concentration in the active volume changes with the variations in $P_{inc}(t)$. The conductance of the active volume, which depends on the mobile charge carrier concentration, also varies with $P_{inc}(t)$. At any time instant t, the average concentration of mobile charge carriers $n(t)$ in the active volume of the photoconducting substrate material follows the continuity equation given as [45, 46],

$$\frac{dn(t)}{dt} = \frac{\eta_e(1 - |\Gamma|^2)AP_{inc}}{h\nu V} - \frac{n(t)}{\tau} \tag{3.5}$$

where η_e is the wavelength dependent external quantum efficiency (number of photo-carriers generated per incident photon), Γ is the wavelength dependent reflectivity at the air–LTG-GaAs interface ($\Gamma = 0.318$ [44]), τ is the average carrier lifetime in the photoconducting substrate ($\tau \approx 0.6$ps [72]) of the PMA and ν is the beat frequency component *i.e.* $\nu = |f_1 - f_2|$. We neglect the spatial variations of η_e assuming it to be uniform over the effective area of illumination. We solve Equation (3.5) for $n(t)$ by substituting the power density given by Equation (3.4) and obtain:

$$n(t) = KP_0\left[1 + \frac{m}{\sqrt{1+\omega^2\tau^2}} sin\left\{\omega t - \phi - \zeta + tan^{-1}\left(\frac{1}{\omega\tau}\right)\right\}\right] + n_{int}e^{\frac{-t}{\tau}} \tag{3.6}$$

where

$$K = \frac{\eta_e(1-|\Gamma|^2)\tau}{h\nu L_{LTG-GaAs}} \tag{3.7a}$$

$$\phi = y(|\overrightarrow{k}_1|sin\theta_1 + |\overrightarrow{k}_2|sin\theta_2) \tag{3.7b}$$

$$P_0 = P_{L1}cos\theta_1 + P_{L2}cos\theta_2 \tag{3.7c}$$

$$m = \frac{\sqrt{P_{L1}P_{L2}}(cos\theta_1 + cos\theta_2)}{P_0} \tag{3.7d}$$

n_{int} is the intrinsic carrier concentration of LTG-GaAs at room temperature (for GaAs, $n_{int} = 2.25 \times 10^{12}$ m^{-3} at 300K [77]). Using the expression for carrier concentration in Equation (3.6), we express the time varying conductance of the active volume as

$$G_p(t) \approx Me(\mu_e + \mu_h)KP_0[1 + \frac{m}{\sqrt{1+\omega^2\tau^2}}sin\{\omega t - \phi - \zeta + tan^{-1}\left(\frac{1}{\omega\tau}\right)\}] \tag{3.8}$$

where $\mu_e \approx 1.6$ m^2/Vs and $\mu_h \approx 0.01$ m^2/Vs are average electron and hole mobility in LTG-GaAs, respectively, and $M = L_{LTG-GaAs}(N_e w_e + N_g(L_e + w_e))/w_g$The contribution from the second term on the right-hand-side of Equation (3.6) is negligible and decays exponentially with time and so, we exclude it in Equation (3.8) and the remaining analysis.

Using the value of $G_P(t)$ from Equation (3.8), we can calculate the current density at the active region in the PMA and the corresponding radiated electric fields which are proportional to the time derivatives of the current densities on the antenna [20]. From the working principle of the PMA, we can present a simple equivalent circuit of the THz PMA as shown in Figure 3.3 [21, 78].

Using the Kirchhoff's Current Law (KCL) on the circuit in Figure 3.3, we obtain an expression for the circuit current $I_p(t)$:

$$I_p(t) = C\frac{dV_c(t)}{dt} + \frac{V_c(t)}{G_p^{-1}(t)} \tag{3.9}$$

As suggested in [21] and discussed in [78,79], we assume a broadband nature for the radiating element and so the equivalent circuit of the antenna in the PMA lacks reactive elements and this broadband nature is represented by the load resistance R_A. The resistance R_A comprises of

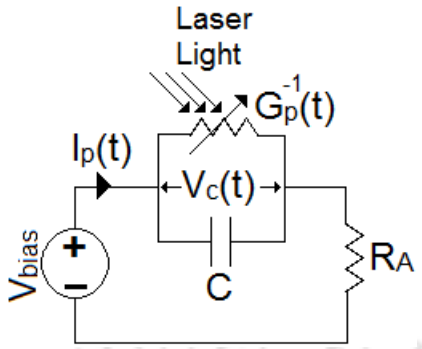

Figure 3.3: Equivalent Circuit of PMA.

the radiation resistance and conduction losses of the antenna.

The value of the inter-electrode capacitance C corresponding to a particular inter-digitated configuration can be calculated from [80] and we use a value of 6.1 fF [21] in our calculations. In order to validate our analysis, we plot the output power ($I_P(t)^2 R_A$), obtained using Equation (3.9), along with experimental results, reported in [21], under similar conditions, in Figure 3.4. We see a reasonably close congruence to experimental results at lower pump-powers. The deviating trend of the analytical results, at higher pump powers, is apparently due to the changes in the substrate properties with the heating effect of the laser irradiation, which has not been considered in the present model. The total incident optical power or the pump power is the sum of the average powers of the two laser sources. The low efficiency of the optical to the electrical power conversion process is one of the factors contributing to typically low output power levels from a THz PMA. A detailed study of the various factors influencing the efficiency of such antennas can be found in [33, 35, 47].

We calculate the output power from the PMA as a function of the bias voltage and plot it with experimental results reported in [31] in Figure 3.5. The analytical results follow identical trend to the measured results for lower values of beat frequencies and approach the measured results at higher beat frequencies.

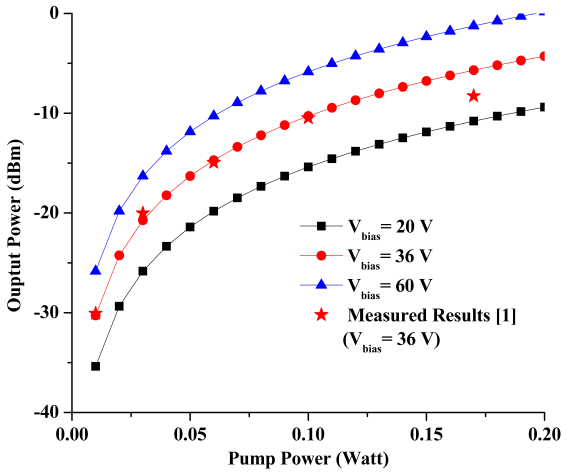

Figure 3.4: Output power as function of pump power at various bias voltages for $R_A = 50\ \Omega$, $C = 6.1$ fF, at $f_1 - f_2$ =200 MHz comprised of ten 1 μm electrodes and nine 1 μm gaps, with $\theta_1 = \theta_2 = \zeta = 0^o$. Measured Results [21]

3.6 Incorporation of Modulating Signal $m(t)$

As discussed in Section 3.1, modulation on a PMA has not been addressed adequately in available literature. Signal modulation on an antenna is a critical part of any communication link. In an attempt to incorporate modulation into a PMA, we extend our analysis to model a scenario as shown in Figure 3.6 where we introduce a signal source $m(t)$ along the path of any one of the two laser beams. The signal $m(t)$ is used as source of modulating signal intended to produce modulation in the output of the PMA. The nature of the signal $m(t)$ and its effect on the output power is discussed in subsequent sections.

Incorporating $m(t)$, as shown in Figure 3.6, into the electric field expressions in Equation (3.2) and (3.3), we obtain the following expression for the instantaneous optical power density incident on the substrate

$$P_{inc}(t) = P_{L1}cos\theta_1 + |m(t)|^2 P_{L2}cos\theta_2 + \sqrt{P_{L1}P_{L2}}(cos\theta_1 + cos\theta_2)m(t)cos(\omega t - y(k_1 sin\theta_1 + k_2 sin\theta_2) - \zeta) \tag{3.10}$$

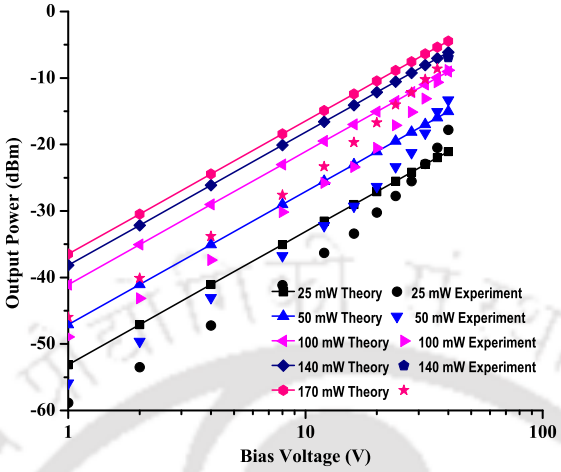

Figure 3.5: Output power as function of bias voltage at various pump powers for $R_A = 50\ \Omega$, $C = 6.1$ fF, at $f_1 - f_2$ =200 MHz comprised of ten 1 μm electrodes and nine 1 μm gaps, with $\theta_1 = \theta_2 = \zeta = 0^o$. Measured Results [31]

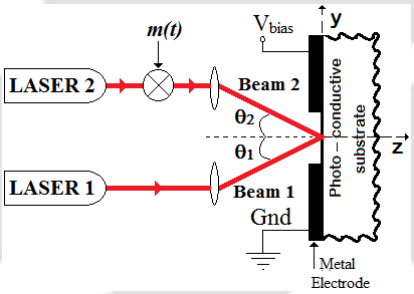

Figure 3.6: System-Model under investigation

3.6.1 Carrier Concentration and Conductance

As discussed above, the mobile charge carrier concentration in the active region depends on the incident optical intensity. However, in this case, the nature of signal $m(t)$ would also influence the average carrier concentration at the active region. We obtain an expression for the average concentration of mobile charge carriers in the active volume, in presence of $m(t)$, by integrating Equation (3.5) as:

$$n(t) = e^{-\frac{t}{\tau}} \int_0^t K e^{\frac{t'}{\tau}} P_{inc}(t')dt' \tag{3.11}$$

The variation in the average carrier concentration in the active region of the PMA causes variations in the conductance, $G_p(t)$, of the active region, which is expressed as

$$G_p(t) \approx Me(\mu_e + \mu_h)e^{-\frac{t}{\tau}} \int_0^t Ke^{\frac{t'}{\tau}} P_{inc}(t')dt' \tag{3.12}$$

where the remaining terms retain their meanings from Equation (3.7). The reducibility of Equation 3.11 to a closed form expression would depend on the nature of the signal $m(t)$. In our model, we assume a basic simple nature for signal $m(t)$ which is discussed in a subsequent section.

3.7 Modulation of THz PMA output

The output signal from a THz PMA is a function of several key parameters of the PMA such as the total incident optical power, AOIs $\{\theta_1, \theta_2\}$, relative phase ζ, beat frequency ω and bias voltage V_{bias}. The signal $m(t)$, in the system, provides additional factor to modulate the output of the PMA. A variation in these parameters would produce a change in the nature of output either in magnitude or in phase.

In the subsequent discussions we investigate the effect of the variations in the key parameters of the PMA on the output of the PMA. We also introduce the nature of $m(t)$ and study its effect on the PMA output.

3.7.1 Pump Power

The pump power incident at the active region of the photoconductive substrate in the PMA determines the amount of photons available for carrier generation. The amount of incident optical power absorbed by the photoconductive substrate is governed by the absorption efficiency of the substrate material which is a function of the wavelength of the incident light. The quantum efficiency of the material, which is also a wavelength dependent quantity, determines the non-equilibrium charge carrier concentration at the active region. We show this dependence for normal incidence at various bias voltages in Figure 3.7.

The ~20 dB/decade slope of the curve suggests that the amplitude of the PMA output can be

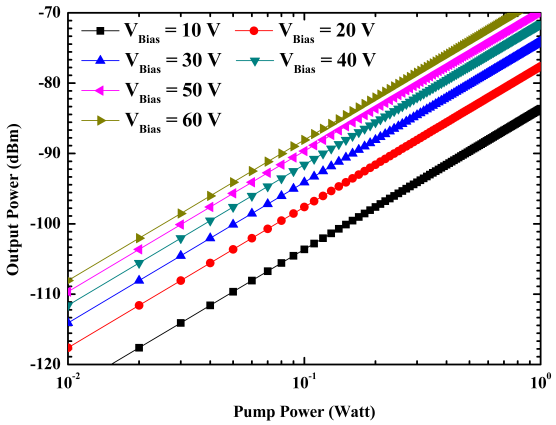

Figure 3.7: Output Power of the PMA as a function of Pump powers and bias voltages at $\theta_1 = \theta_2 = \zeta = 0^o$, $|f_1 - f_2| = 1$ THz

modulated by varying the incident optical power. The incident power can be varied by installing optical intensity modulators along the way of the laser beams. A basic way of implementing this, is the introduction of $m(t)$ in Figure 3.6. The nature of $m(t)$ is expressed in Equation (3.13). The ON/OFF power ratio is determined by the amplitude of the signal $m(t)$ and can be used for improving the received bit error rate in the transmission link. With proper calibration, the fluctuations in the output power in Figure 3.7 can be utilized in sensing as well as communication applications.

3.7.2 Beat Frequency, ω

The charge carrier generation at the active region of the PMA depends on the beat frequency produced in the material during the mixing of the two incident wavelengths. The output of the PMA is dependent on the charge carrier concentration through the current I_p(t) which is expressed in Equation (3.9). We can, therefore, vary the wavelengths of the two lasers to cause modulations in the PMA output which is shown in Figure 3.8.

The ~19 dB/decade decay in the output power closely resembles the roll of characteristics of a first order low-pass filter suggesting the presence of a low pass effect in the PMA. The carrier lifetime limits the response of the material as the frequency increases which creates this effect. Variation in the beat frequency is, thus, another strategy for signal modulation in the

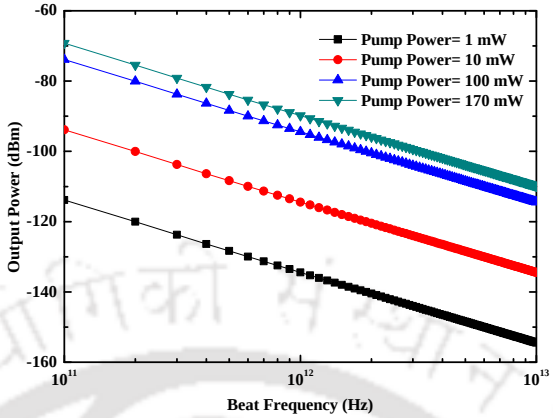

Figure 3.8: Output power as a function of beat frequency at V_{bias} = 40 V at different pump powers.

PMA, which is useful especially in frequency-hopping type wireless communication links.

3.7.3 Bias Voltage, V_{bias}

The net electric field in the gap, which creates the current in the PMA, depends on the bias voltage V_{bias}. The current I_p(t) determines the output power of the PMA. The dependence of PMA output on V_{bias} is shown in Figure 3.9.

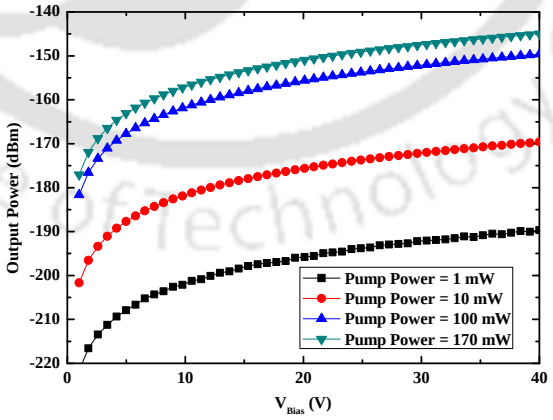

Figure 3.9: Variation in the PMA Output power, at $|f_1 - f_2| = 1$ THz, with V_{bias} ($\theta_1 = \theta_2 = \zeta = 0^o$)

The positive ~3.52 dB/volt slope in the characteristics present the variation in the bias voltage as another viable option of producing modulation in the PMA output. Voltage fluctuations

are common in sensors and can make the PMA effective as a wireless sensor node.

3.7.4 Relative Phase ζ

In time domain, a variation in ζ, as in Equation (3.4), would produce a phase shift in PMA output. Phase modulation is another well known technique in communications. We plot the circuit current I_p as a function of ζ in Figure 3.10.

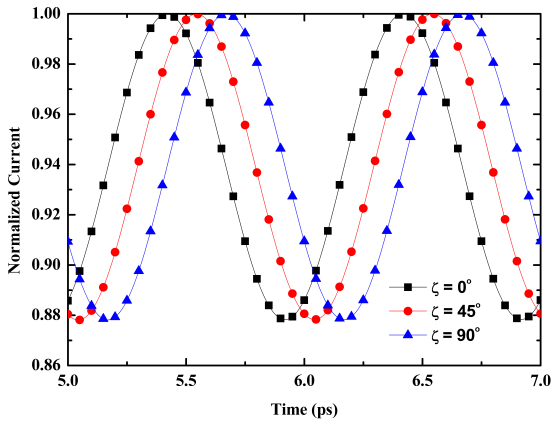

Figure 3.10: Circuit current I_p as a function of ζ ($\theta_1 = \theta_2 = 0^o$) for 1 THz beat frequency at V_{bias}=30 V and $P_{L1} + P_{L2} = 50\ mW$

Variations in ζ can be obtained by using an optical phase modulator and such phase differences in the output can be used in PMA arrays. PMA array is another topic where not much investigation has been reported. A good array would enable high gain radiators which enhances the range in wireless communications. In sensing applications, phase change of the incident laser beam may be used as the sensed parameter with proper calibration.

3.7.5 Angle of Incidence θ_1 and θ_2

As seen in Equation (3.11), the charge carrier concentration in the active region is a function of the pump power which is in-turn a function of the AOIs of the two laser beams. We plot the temporal evolution of the carrier concentration as a function of angle of incidence in Figure 3.11. At a given angle of incidence, the carrier concentration initially increases from its intrinsic value and then oscillates around a saturating value which is dependent on the angle of incidence and

other parameters.

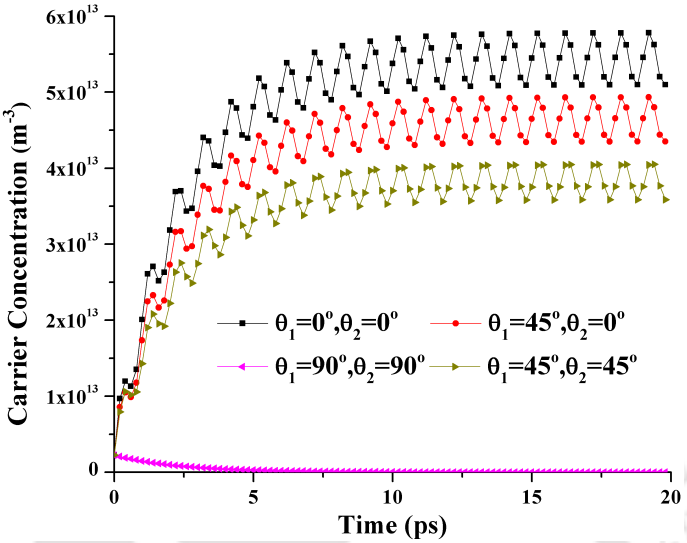

Figure 3.11: Temporal evolution of $n(t)$ in the active region as a function of AOIs for $|f_1 - f_2| = 1THz$; $P_{L1} + P_{L2} = 0.1W$; $\phi = 0^o$; $\zeta = 0^o$

The change in the carrier concentration with AOI varies the circuit current I_p(t) which leads to changes in the output power of the PMA. The output power of the PMA as a function of the AOIs is shown in Figure 3.12.

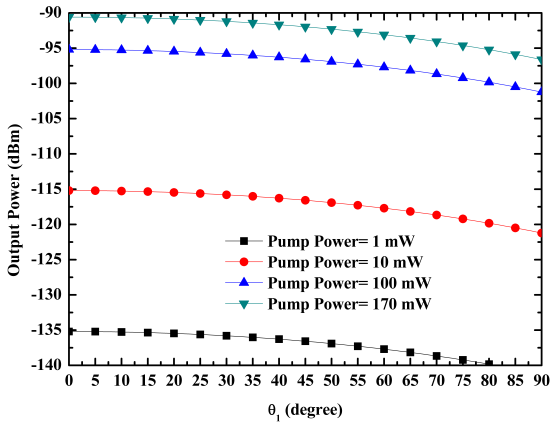

Figure 3.12: Effect of AOI on PMA Output power at 1 THz beat with $\theta_2 = \zeta = 0^o$ and V_{bias} = 30 V

From the plots, we can infer deduce that, with effective calibration, keeping one beam at a fixed AOI and varying the AOI of the other would enable tracking of the AOI of the latter. This

shows the utility of the PMA in detection and tracking of motion which is integral to many field applications.

Inspite of being initially very small, as seen in Figure 5.12, the slope increases beyond 45^o to $\sim$ 0.15 dB per degree. Thus varying the AOIs can also be used to modulate the PMA output to a small extent. On the contrary, we can also say that applications where the tolerance in the output is more than $\sim$ 0.15 dB per degree, PMA would be a good choice for providing a reasonably stable output.

3.7.6 Signal $m(t)$

In Figure 3.6, we introduced a signal $m(t)$ into the conventional PMA model to incorporate additional degree of freedom to modulate the PMA output. In order to demonstrate this, we choose a basic binary nature for $m(t)$, defined as

$$m(t) = \begin{cases} 1 & t \leq \alpha_D T \\ 0 & t \geq \alpha_D T \end{cases} ; \; m(t+T) = m(t) \tag{3.13}$$

where the duty cycle α_D and the time period T $(2\pi/\omega)$ determine the nature of the PMA output signal. The nature of the signal $m(t)$ expressed in Equation (3.13) is chosen, assuming $m(t)$ to be a basic ON/OFF keying element. If $m(t)$ is assumed to be a phase modulating element, the nature of the expression in Equation (3.13) would be different. However, for a non-constant value of $m(t)$, analytical solution of equation (3.11) would be quite involved and perhaps analytically intractable. We solve equations (3.11) and (3.12) numerically and obtain the output power by applying Kirchhoff's Voltage Law (KVL) to Figure 3.3.

3.7.7 Duty cycle α_D

Assuming the pulsed nature of the signal $m(t)$ expressed in Equation (3.13), the duty cycle α_D is indicative of the maximum data rate that can be achieved using a PMA in a wireless communication link. The width of the pulse controls the envelope of the PMA output signal which we show in Figure 3.13.

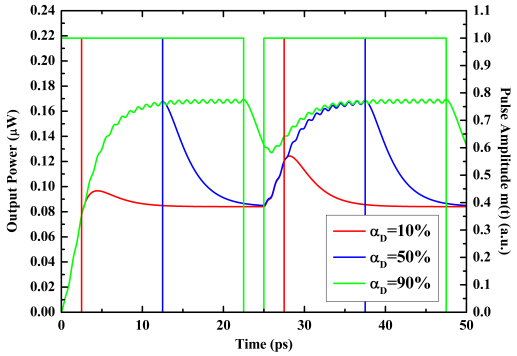

Figure 3.13: Impact of α_D on the PMA output at 1 THz beat with AOIs = 0^o, V_{bias} = 30 V and 100 mW pump power

As seen in the Figure 3.13, a change in the pulse width of $m(t)$ would vary the level to which the output signal decays and thereby determines the minimum time between two consecutive pulses in a symbol in digital transmission. This indirectly sets a limit on the maximum allowable data rate that can be achieved in a digital transmission using the PMA. Lower the value of α_D, better would be the data rate but shorter would be the sampling interval which would lead to rise in bit error rate. A higher value of α_D, would provide ample sampling interval but at the cost of a lower data rate.

3.8 PMA Current Density

The charge carriers generated at the active region of the PMA, accelerate under the effect of the net electric field across the electrode gap. This acceleration of charge carriers creates a time varying current density across the active region. The components of this current density across the active region of the PMA generated due to the net electric field $\overrightarrow{E}_{net}^{a,b}$, created by the bias voltage, V_{bias} (across $V^+ - V^-$ in Figure 3.1) are shown in Figure 3.14.

As per the assumed geometry (in Figure 3.2), the horizontal (x-components) components of the current density are directed opposite to each other. The radiated fields from these components would cancel out in the far field. Therefore, radiation from the PMA would be mostly due to the vertical (y-component) components of the current density which add up in the far field

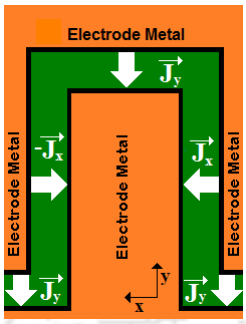

Figure 3.14: Components of the current density in a PMA.

region. Using Figure 3.1, we obtain:

$$\vec{J}^{a,b}(t) = \sigma(t)\vec{E}^{a,b}_{net}(t) = \sigma(t)(\vec{E}_{bias} + \vec{E}^{a,b}_{1y}(t) + \vec{E}^{a,b}_{2y}(t)) \tag{3.14}$$

The indices a and b, in Equation (3.14), represent the two general cases of optical polarization as discussed earlier. The terms $\vec{E}_{bias}$, $\vec{E}_{1y}$ and $\vec{E}_{2y}$ are respectively the electric field due to bias and the tangential electric field components at the air–LTG-GaAs interface. Without significant loss of generality for a small aperture PMA, we assume the following: (a) uniform illumination over the active region and (b) $\partial\vec{E}_{bias}/\partial x \equiv 0, \partial\vec{E}_{bias}/\partial y \equiv 0$ over w_e and w_g respectively.

Using Equations (3.2) and (3.3), in presence of $m(t)$ under cases (a) & (b), we can write:

$$\vec{E}^{a}_{net} = -\hat{a}_y \frac{V_{bias}}{w_g} \tag{3.15}$$

$$\begin{aligned}\vec{E}^{b}_{net}(t) = -\hat{a}_y \Big[&\sqrt{2P_{L2}\eta_0}m(t)cos\theta_2 cos(\omega_2 t + \zeta + k_2 y sin\theta_2) \\ &+ \sqrt{2P_{L1}\eta_0}cos\theta_1 cos(\omega_1 t - k_1 y sin\theta_1) + \frac{V_{bias}}{w_g}\Big]\end{aligned} \tag{3.16}$$

As discussed earlier, THz radiation from the PMA occurs only for $m(t)$=1 and so, we present the expressions for the current density at the active region for $m(t)$=1 only. The corresponding expressions for the current densities in the two cases (a) and (b) (discussed in Section 3.4) are as follows:

For $m(t) = 1$,

$$\vec{J}^{a}_{1}(t) = -\hat{a}_y eK\tau\mu_e \frac{V_{bias}}{w_g} P(\omega) \tag{3.17}$$

$$\overrightarrow{J}_1^b(t) = -\hat{a}_y eK\tau\mu_e P(\omega)Q(\omega_1, \omega_2, V_{bias}) \tag{3.18}$$

The expressions for $P(\omega)$ and $Q(\omega_1, \omega_2, V_{bias})$ are provided Appendix A. In order to present a

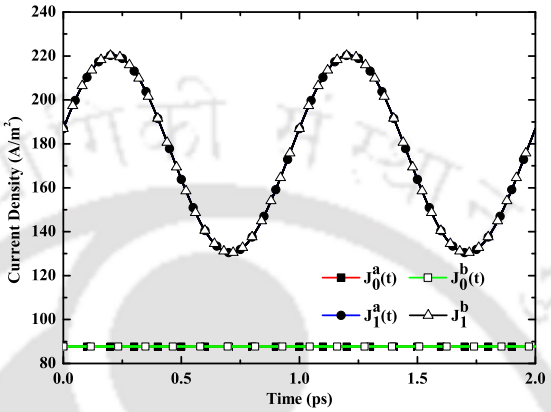

Figure 3.15: PMA current densities for $\theta_1 = \theta_2 = \zeta = 0^o$, $|f_1 - f_2| \approx 1THz$, $P_{L1} + P_{L2} = 150mW$ and $V_{bias} = 36V$.

qualitative feel of the nature of the current densities for $m(t)$=0, we plot the current densities for both $m(t)$=0 and $m(t)$=1 in Figure 3.15. Due to the absence of beating phenomenon for $m(t) = 0$, we observe almost a time independent nature of the current density because $f_{1,2} \gg 1/\tau$. The congruence $J_1^a \approx J_1^b$ observed in Figure 3.15 can be attributed to the predominance of the beat frequency mode contribution over that of the modes with higher frequencies in Equation (3.18). Intuitively, we may assume this mode to be the predominant radiated component in the PMA output.

3.9 Radiated Fields from the PMA

Radiation from a PMA occurs from the time varying current densities expressed in Equations (3.17) and (3.18). These current densities are separated in space both horizontally as well as vertically by the subsequent electrode widths w_e and gaps w_g and the electrode lengths L_e respectively. If $L_e \ll \lambda_\omega$ (λ_ω being the radiated wavelength), the spatial phase difference between the current densities would be very small and may be ignored in the far field. Otherwise, the spatial phase has to be considered in the far field by modelling the location of individual

current elements as that from a two-dimensional antenna array. Here, we present the radiated fields in the first scenario and present the antenna factor expression for the second scenario. The radiated fields in the latter scenario can be derived from the product of the antenna factor and the radiated field of a single radiating element.

To obtain the radiated fields from the PMA, we assume the current densities to be along the air–LTG-GaAs interface such that they can be treated as interfacial currents. If we solve the Helmholtz's equation appropriately for the Hertz potentials [81], we can derive the corresponding electric and magnetic field expressions.

In the present case, we have two distinct regions in space. The air region (on the side of incident beams) is termed as Region 1 and the semiconductor region is termed as Region 2. As pointed out earlier, we only present expressions for $m(t)$=1 in both cases (a) and (b). The contribution from the multiple frequency components in the current density expressions are assumed to be superimposed in the far field. In the subsequent equations we use the spherical coordinate (r, θ, ϕ) and the geometry shown in Figure 3.1 to express the far fields of the PMA.

In Region 1, *i.e.* for $\pi/2 \leq \theta \leq \pi$, components $\overrightarrow{J}_1^a$ and $\overrightarrow{J}_1^b$ generate the following expressions of the radiated fields :

$$E_{1\theta}^a = \frac{jk\eta_0 V_{bias}}{2\pi w_g} Ke\tau\mu_e P(\omega) \frac{e^{jkr}}{r} F_{1\theta}(\theta, \phi) \tag{3.19}$$

$$E_{1\phi}^a = -\frac{jk\eta_0 V_{bias}}{2\pi w_g} Ke\tau\mu_e P(\omega) \frac{e^{jkr}}{r} F_{1\phi}(\theta, \phi) \tag{3.20}$$

$$H_{1\theta}^a = -\frac{1}{\eta_0} E_{1\phi}^a \tag{3.21}$$

$$H_{1\phi}^a = \frac{1}{\eta_0} E_{1\theta}^a \tag{3.22}$$

$$E_{1\theta}^b = \frac{jk\eta_0}{2\pi} Ke\tau\mu_e P(\omega) Q(\omega_1, \omega_2, V_{bias}) \frac{e^{jkr}}{r} F_{1\theta}(\theta, \phi) \tag{3.23}$$

$$E_{1\phi}^b = -\frac{jk\eta_0}{2\pi} Ke\tau\mu_e P(\omega) Q(\omega_1, \omega_2, V_{bias}) \frac{e^{jkr}}{r} F_{1\phi}(\theta, \phi) \tag{3.24}$$

$$H_{1\theta}^b = \frac{1}{\eta_0} E_{1\theta}^b \tag{3.25}$$

$$H_{1\phi}^b = -\frac{1}{\eta_0} E_{1\phi}^b \tag{3.26}$$

Here, k and n are respectively the free-space wavenumber and the refractive index of the PMA substrate. For Region 2, *i.e.* $0 \leq \theta\pi/2$, we have two subranges separated by the critical angle of the substrate material: $0 \leq \theta \leq \theta_c$ and $\theta_c < \theta \leq \pi/2$. The expressions for the fields in the two subranges differ by the pattern factor term. For subrange-1, *i.e.* $0 \leq \theta \leq \theta_c$, we have:

$$E_{2\theta}^{a,1} = \frac{j\mu_s k\eta_0 V_{bias}}{2\pi w_g} Ke\tau\mu_e P(\omega)\frac{e^{j\mu_s kr}}{r}F_{2\theta}^{1}(\theta,\phi) \tag{3.27}$$

$$E_{2\phi}^{a,1} = \frac{j\mu_s k\eta_0 V_{bias}}{2\pi w_g} Ke\tau\mu_e P(\omega)\frac{e^{j\mu_s kr}}{r}F_{2\phi}^{1}(\theta,\phi) \tag{3.28}$$

$$H_{2\theta}^{a,1} = -\frac{\mu_s}{\eta_0}E_{2\phi}^{a,1} \tag{3.29}$$

$$H_{2\phi}^{a,1} = \frac{\mu_s}{\eta_0}E_{2\theta}^{a,1} \tag{3.30}$$

$$E_{2\theta}^{b,1} = \frac{j\mu_s k\eta_0}{2\pi} Ke\tau\mu_e P(\omega)Q(\omega_1,\omega_2,V_{bias})\frac{e^{j\mu_s kr}}{r}F_{2\theta}^{1}(\theta,\phi) \tag{3.31}$$

$$E_{2\phi}^{b,1} = \frac{j\mu_s k\eta_0}{2\pi} Ke\tau\mu_e P(\omega)Q(\omega_1,\omega_2,V_{bias})\frac{e^{j\mu_s kr}}{r}F_{2\phi}^{1}(\theta,\phi) \tag{3.32}$$

$$H_{2\theta}^{b,1} = \frac{\mu_s}{\eta_0}E_{2\theta}^{b,1} \tag{3.33}$$

$$H_{2\phi}^{b,1} = -\frac{\mu_s}{\eta_0}E_{2\phi}^{b,1} \tag{3.34}$$

For subrange-2, *i.e.* $\theta_c \leq \theta \leq \pi/2$, we have:

$$E_{2\theta}^{a,2} = \frac{j\mu_s k\eta_0 V_{bias}}{2\pi w_g} Ke\tau\mu_e P(\omega)\frac{e^{j\mu_s kr}}{r}F_{2\theta}^{2}(\theta,\phi) \tag{3.35}$$

$$E_{2\phi}^{a,2} = \frac{j\mu_s k\eta_0 V_{bias}}{2\pi w_g} Ke\tau\mu_e P(\omega)\frac{e^{j\mu_s kr}}{r}F_{2\phi}^{2}(\theta,\phi) \tag{3.36}$$

$$H_{2\theta}^{a,2} = -\frac{\mu_s}{\eta_0}E_{2\phi}^{a,2} \tag{3.37}$$

$$H_{2\phi}^{a,2} = \frac{\mu_s}{\eta_0}E_{2\theta}^{a,2} \tag{3.38}$$

$$E_{2\theta}^{b,2} = \frac{j\mu_s k\eta_0}{2\pi} Ke\tau\mu_e P(\omega)Q(\omega_1,\omega_2,V_{bias})\frac{e^{j\mu_s kr}}{r}F_{2\theta}^2(\theta,\phi) \tag{3.39}$$

$$E_{2\phi}^{b,2} = \frac{j\mu_s k\eta_0}{2\pi} Ke\tau\mu_e P(\omega)Q(\omega_1,\omega_2,V_{bias})\frac{e^{j\mu_s kr}}{r}F_{2\phi}^2(\theta,\phi) \tag{3.40}$$

$$H_{2\theta}^{b,2} = \frac{\mu_s}{\eta_0}E_{2\theta}^{b,2} \tag{3.41}$$

$$H_{2\phi}^{b,2} = -\frac{\mu_s}{\eta_0}E_{2\phi}^{b,2} \tag{3.42}$$

The expressions for $P(\omega)$, $Q(\omega_1,\omega_2,V_{bias})$ and the pattern factor terms in the above expressions are presented in Appendix A.

3.9.1 Poynting Vector

From the above expressions, we can derive the expressions for the Poynting vector, in all regions, for both cases ((a) and (b)). For the Region 1, we obtain:

$$\overrightarrow{S}_1^a = \hat{a}_r\frac{k^2\eta_0 V_{bias}^2}{8\pi^2 w_g^2 r^2}K^2e^2\tau^2\mu_e^2P(\omega)^2\left[\{F_{1\theta}(\theta,\phi)\}^2 + \left\{F_{1\phi}(\theta,\phi)\right\}^2\right] \tag{3.43}$$

$$\begin{aligned}\overrightarrow{S}_1^b = \hat{a}_r\frac{k^2\eta_0 K^2e^2\tau^2\mu_e^2}{8\pi^2 r^2}P(\omega)^2Q(\omega_1,\omega_2,V_{bias})^2\\ \left[\{F_{1\theta}(\theta,\phi)\}^2 + \left\{F_{1\phi}(\theta,\phi)\right\}^2\right]\end{aligned} \tag{3.44}$$

For $0 \le \theta \le \theta_c$ in Region 2, we have:

$$\begin{aligned}\overrightarrow{S}_2^{a,1} = \hat{a}_r\frac{n^2k^2\eta_0 V_{bias}^2}{8\pi^2 w_g^2 r^2}K^2e^2\tau^2\mu_e^2P(\omega)^2\\ \left[\left\{F_{2\theta}^1(\theta,\phi)\right\}^2 + \left\{F_{2\phi}^1(\theta,\phi)\right\}^2\right]\end{aligned} \tag{3.45}$$

$$\begin{aligned}\overrightarrow{S}_2^{b,1} = \hat{a}_r\frac{n^2k^2\eta_0 K^2e^2\tau^2\mu_e^2}{8\pi^2 r^2}P(\omega)^2Q(\omega_1,\omega_2,V_{bias})^2\\ \left[\left\{F_{2\theta}^1(\theta,\phi)\right\}^2 + \left\{F_{2\phi}^1(\theta,\phi)\right\}^2\right]\end{aligned} \tag{3.46}$$

The Poynting vector expression for the subrange 2 in Region 2 can be derived similarly.

For the case when L_e is comparable to λ_ω, the individual elements would behave as a part

of a spatially distributed 2-dimensional array of elemental radiators. We have derived the array factor (A.F.) for such a distribution of antenna elements which is given as:

$$|A.F.| = |\frac{sin(N_e u/2)sin((u+2v)/2)}{sin(u/2)sin((u+2v)/4)}| \tag{3.47}$$

Here, $u = 2nk(w_g + w_e)sin\theta cos\phi$ and $v = L_e knsin\theta sin\phi$. The array factor multiplied with the pattern of a single element gives the pattern of the array. The product of this array factor with the radiation of a single radiating element provides the radiation due to the array of the radiating elements.

3.10 Efficiency of PMAs

Due to the multi-physics involved in the operation of a PMA, the efficiency of a PMA is a function of several intermediate efficiencies. Figure 3.16 describes the different efficiencies involved in the total antenna efficiency of the PMA.

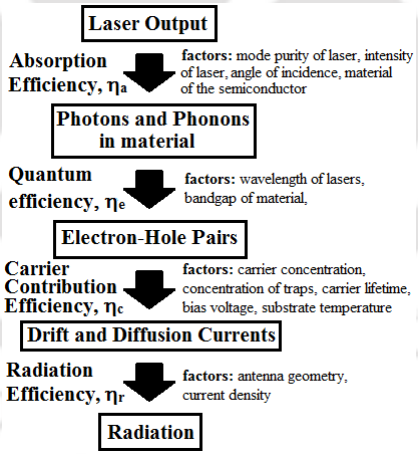

Figure 3.16: Various efficiencies in a PMA

The overall antenna efficiency η can hence be written as the product $\eta_a\eta_e\eta_c\eta_r$ of the intermediate efficiencies in the PMA. The material of the semiconductor and the angle of incidence determines the reflection coefficient at the air semiconductor interface. The reflection of light for oblique incidence can be reduced further by application of anti-reflecting material layer at the active region of the PMA. The above figure presents qualitatively the various factors that

can be controlled to enhance the efficiency of the PMA.

3.11 Conclusion

In this Chapter, we have presented a simple, preliminary yet generalized analytical model for the carrier generation and conductance in a THz PMA under two distinct cases on incident beam polarization along with the presence of an binary state signal source along one of the laser beams. We found reasonably close agreement between analytical and measured results in literature. Strategies of modulating the PMA output have been proposed and the effect of these techniques have been studied. Analytical expressions for radiated fields from the PMA have been derived for the generalized cases of beam polarization. A qualitative discussion on the efficiency of PMA and the various factors involved has been discussed. The present analysis reasonably models the multi-physical scenarios in the PMA operation and is surely a preliminary step towards design of such antennas.

4

An Introduction to Microwave Applications of Graphene

In this chapter, we begin with a brief introduction to Graphene and its basic electrical characteristics. We implicitly emphasize the preference of Graphene for THz band applications by proposing novel voltage controlled transmission line and antenna designs for the THz band employing Graphene. These designs produce interesting as well as important results. In order to comprehend the scope of applicability of Graphene, we also propose and discuss a 2-element antenna array design at the Ka-band employing Graphene in the Appendix B.

4.1 Introduction

Graphene [22] is a mono-atomic lattice of tessellated hexagonal rings of sp^2- hybridized carbon atoms, as shown in Figure 4.1. Its quasi-2D structure endows Graphene with unique and remarkable electronic properties such as ballistic electronic transport, negative differential resistance etc., which can be put to applications in various important fields such as medicine, biology and defence. Because of its interesting and useful propeties and potential applications, Graphene has even been claimed to be "the silicon of the 21st century" [12].

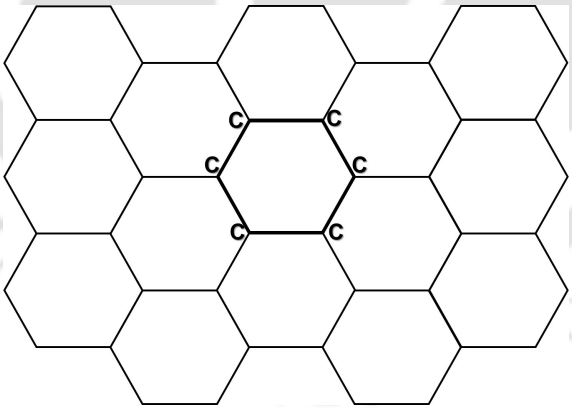

Figure 4.1: Structure of Graphene

One of the interesting properties of Graphene is the change in its conductivity due to application of a transverse electric field [82]. This property of Graphene nano-ribbons has been utilized in design and operations of Graphene Field effect transistors and related devices such as LNAs, mixers, frequency multipliers etc. Its high conductivity and ability to support surface plasmon polariton (SPP) waves at lower Terahertz (THz) frequencies makes it a good choice for

coplanar waveguides, Nano Ribbons [83], Nano-patch antennas [82, 84], beam re-configurable antennas [85] etc. Research and development of novel devices employing Graphene are at a rapid progress with the impetus coming from the potential of Graphene for high frequency electromagnetic applications.

4.2 Surface Conductivity of Graphene

Graphene, being a one-atom thick layer of carbon rings, has a thickness of about 0.345 nm. However, for most practical purposes it has been modelled as quasi 2D surface with a surface conductivity expressed as [60]:

$$\sigma(\omega,\mu_c,\Gamma,T)=\frac{je^2(\omega-j2\Gamma)}{\pi\hbar^2}\left[\frac{1}{(\omega-j2\Gamma)^2}\int_0^\infty \varepsilon\left(\frac{\partial f_d(\varepsilon)}{\partial\varepsilon}-\frac{\partial f_d(-\varepsilon)}{\partial\varepsilon}\right)d\varepsilon-\int_0^\infty\frac{f_d(-\varepsilon)-f_d(\varepsilon)}{(\omega-j2\Gamma)^2-4(\varepsilon/\hbar)^2}d\varepsilon\right] \tag{4.1}$$

where ω is the angular frequency (rad/s), μ_c is the chemical potential, Γ is the phenomenological scattering rate which has been assumed to be independent of energy ε, $-e$ is the charge of an electron, $\hbar = h/2\pi$ is the reduced Planck's constant, $f_d(\varepsilon) = (e^{(\varepsilon-\mu_c)/k_BT}+1)^{-1}$ is the Fermi-Dirac distribution, k_B is the Boltzmann's constant and T is the absolute temperature. The above expression assumes an absence of any external magnetic field.

Equation (4.1) contains contributions from inter-band and intra-band transitions, $\sigma(\omega,\mu_c,\Gamma,T) = \sigma_{intra} + \sigma_{inter}$. In the absence of any external magnetic field, σ_{intra} and σ_{inter} can be expresses as [60]:

Intra-Band Contribution

$$\sigma_{intra}(\omega,\mu_c,\Gamma,T) = -\frac{je^2k_BT}{\pi\hbar^2(\omega-j2\Gamma)}\left(\frac{\mu_c}{k_BT}+2ln(1+e^{-\frac{\mu_c}{k_BT}})\right) \tag{4.2}$$

Inter-Band Contribution

$$\sigma_{inter}(\omega,\mu_c,\Gamma,T) \simeq -\frac{je^2}{4\pi\hbar}ln\left(\frac{2|\mu_c|-(\omega-j2\Gamma)\hbar}{2|\mu_c|+(\omega-j2\Gamma)\hbar}\right) \tag{4.3}$$

At microwave and millimetre waves, the intra-band contribution to the conductivity is predominant. Instances of the typical inter-band and intra-band complex conductivity of Graphene as a

function of frequency at different values of μ_c are shown in Figure 4.2 and 4.3 respectively.

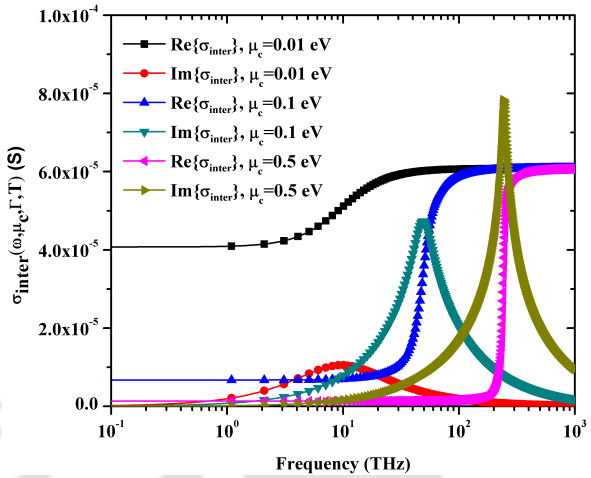

Figure 4.2: Real and Imaginary parts of Inter-band conductivity

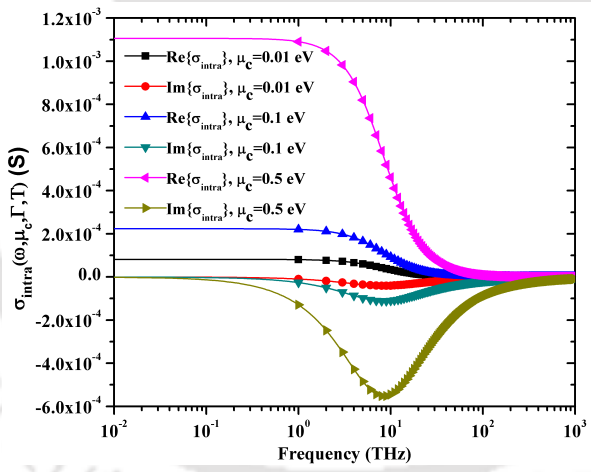

Figure 4.3: Real and Imaginary parts of Intra-band conductivity

The surface conductivity of Graphene as a function of frequency at different chemical potentials is shown in Figure 4.4

The predominance of the intra-band term can be clearly seen in the behaviour of the curves in Figure 4.4. However, at even higher THz frequencies, the inter-band contribution dominates which is shown in Figure 4.5.

The surface resistivity of Graphene as a function of frequency is shown in Figure 4.6. As seen in the figure, the Graphene in the simulations can be modelled as a finite conductivity (or

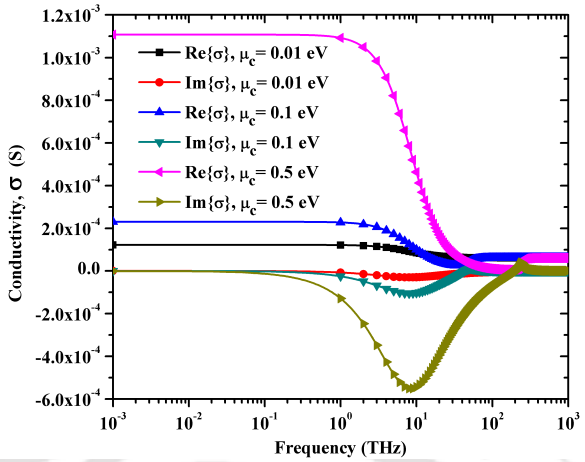

Figure 4.4: Surface conductivity of Graphene as function of frequency at various chemical potentials

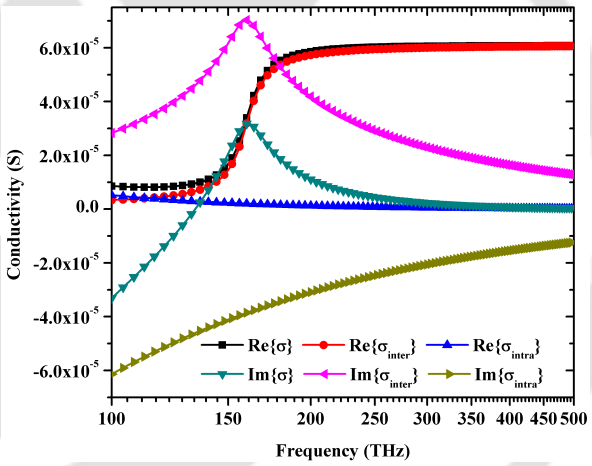

Figure 4.5: Surface conductivity of Graphene as function of higher THz frequency at μ_c= 0.5 eV

resistivity) surface in the PMA geometry.

The chemical potential μ_c for an isolated Graphene sheet is determined by the carrier density n_s which is derived as [60]:

$$n_s = \frac{2}{\pi\hbar^2 v_F^2}\int_0^\infty \varepsilon[f_d(\varepsilon) - f_d(\varepsilon + 2\mu_c)]d\varepsilon \tag{4.4}$$

where, $v_F \simeq 9.5\times10^5 m/s$ is the Fermi velocity. The carrier density function can be controlled by the application of a bias voltage and/or chemical doping which, in turn, changes the conductivity of the Graphene layer. The conductivity of Graphene is about 666.67 S/m at 0V (OFF state) and about 10^7S/m at 15V (ON state), as demonstrated in [82]. To provide transverse electric

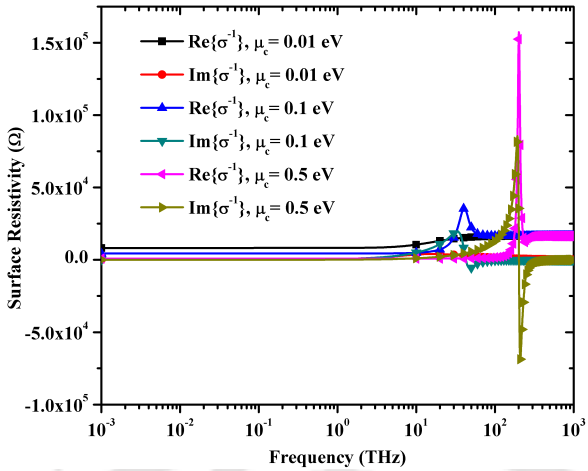

Figure 4.6: Surface resistivity of Graphene as function of frequency at different chemical potential.

bias fields to the Graphene layer, electrodes on methyl methacrylate (100nm thick) layer above the Graphene layer [82] and grounded polysilicon gating pads may be embedded beneath the Graphene layer in the substrate [85]. The controllable dynamic change in the conductivity of Graphene makes it suitable for potential applications in the field of electromagnetic waves and antennas as well. In the subsequent discussions, we introduce and discuss few such potential applications. For the purpose of our simulations, the two states of Graphene, 'ON' and 'OFF', are accounted for by defining two separate materials with the corresponding conductivity values. The simulations have been performed using Ansys HFSS^{TM} Version 15.

4.3 Voltage controlled transmission line employing Graphene

A voltage controlled transmission line, in principle, is one in which the the power transfer characteristics from source to destination can be controlled by application of a control voltage signal. These transfer characteristics can be magnitude, phase, polarization etc. Based on the type of variation produced, voltage controlled transmission lines may be identified with different nomenclatures. A voltage-controlled transmission line geometry can be viewed as a very basic, simple and fundamental microwave structure or component that forms a part of more complex switching components or systems, one of which is presented in Appendix B. Therefore, as a start, it would be worthwhile to investigate this basic structure before moving on to its applications.

Table 4.1: Microstrip Transmission Line Geometry

λ	114.4 μm	B	L
d	0.5λ	h	5μm
s	0.25λ	t	0.06 μm
L	2d+s	w	4.72 μm

4.3.1 Transmission Line Geometry

In our application, a gap discontinuity is created on a 50Ω conventional microstrip transmission line of width 'w' is printed on a Arlon AR1000 substrate (ϵ_r = 10) of thickness 'h'. The choice of the substrate comes from the discussions in Chapter 2 The '$s \times w$' gap in the line is filled in with Graphene. The geometry of the transmission line is given in Figure 4.7.

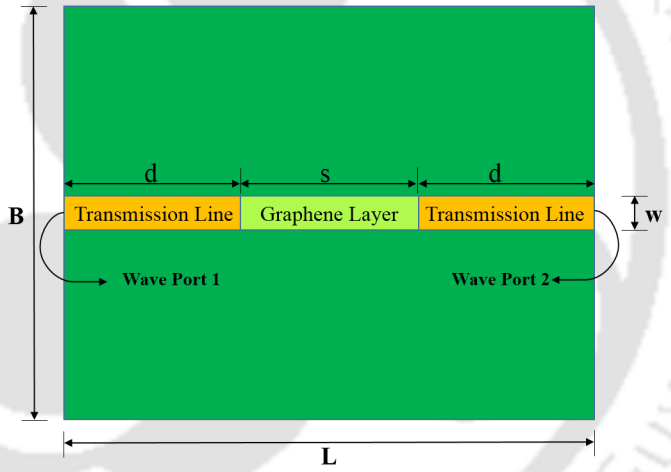

Figure 4.7: Geometry of Microstrip Line with Graphene

The thickness 't' of the metal and the Graphene layer are kept equal for convergence and optimal results. The geometrical dimensions of the transmission line structure in Figure 4.7 are given in the Table 4.1.

4.3.2 Operation of the Line

The transmission line is fed at Port 1 and the conductivity value of the Graphene layer is toggled between ON and OFF states. In the OFF state, the conductivity of the Graphene layer is low and little or no power from the energization at port is detected at at Port 2. For the ON state, the conductivity of the Graphene layer is high and it conducts the signal across to Port 2.

This operation can be observed in Figure 4.8 where we show the current distribution along the transmission line in the ON and OFF states.

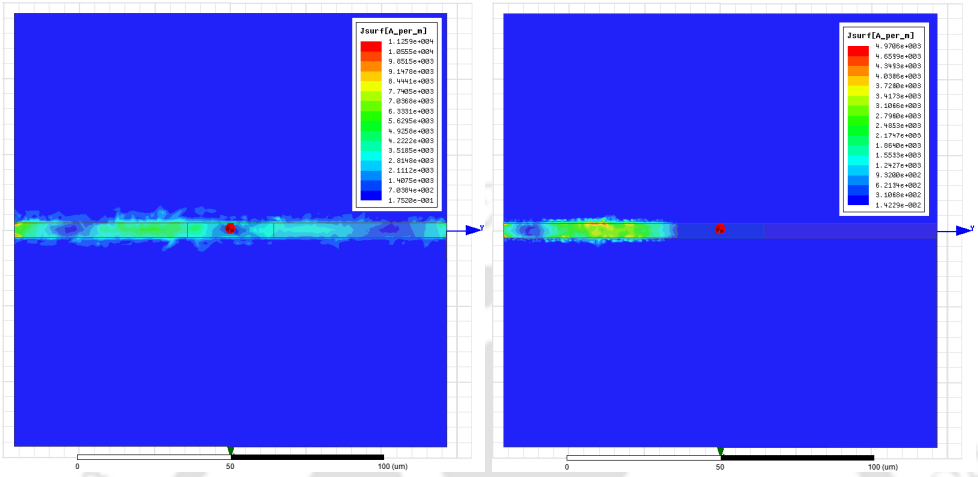

Figure 4.8: Current Distribution on the Microstrip Line in the ON and OFF states of the Graphene

4.3.3 Results

The Graphene layer, essentially, acts as voltage-controlled switch in the transmission line structure. The insertion and return loss of the Graphene layer can be determined from Figure 4.9 where we plot the S_{11} and S_{21} parameters of the transmission line geometry in the ON and OFF states.

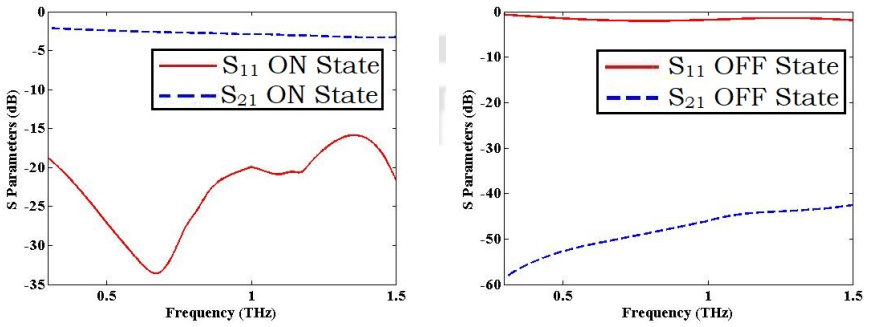

Figure 4.9: S-Parameters of the Microstrip Line in the ON and OFF states of the Graphene

Figure 4.9 shows a good isolation between the two ports during the OFF state and a good power coupling to the output, in the ON state.

4.4 Beam Switching Beam Employing Graphene

4.4.1 Antenna Geometry

In this application of Graphene to antenna technology, we place a 60 nm thick '+' (plus) shaped layer of Graphene coplanarly next to a semicircular microstrip antenna as shown in Figure 4.10. The semicircular antenna is printed on a grounded Silicon Dioxide ($SiO_2, \epsilon_r = 4$) substrate. For additional strength of the structure a silicon backing may also be used. However, for the purpose of our investigation, the silicon backing has been excluded from the geometry.

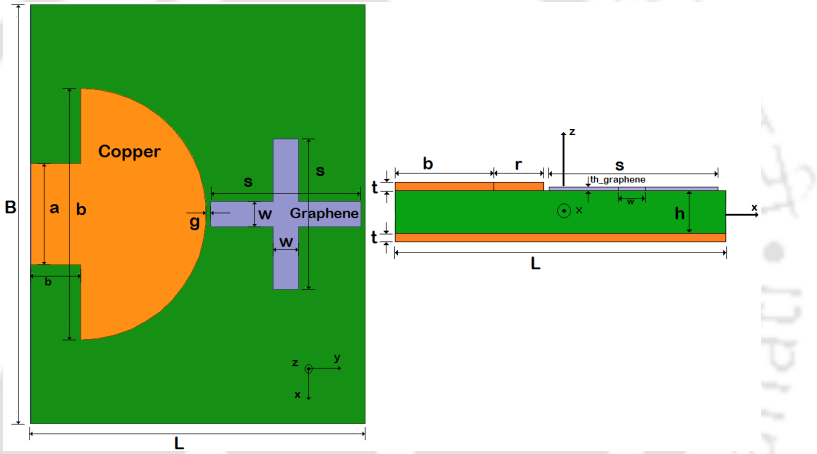

Figure 4.10: Geometry of the Semicircular Disk Antenna (a) Top-view (b) Cross-sectional View

The values of the various geometrical parameters have been tabulated in Table 4.2.

Table 4.2: Dimension of Antenna Geometry

L	400 μm	t	0.2 μm	a	120.77 μm
B	500 μm	th_Graphene	60 nm	b	60 μm
h	43 μm	d	150 μm	g	5 μm
s	180 μm	r	d/2		

4.4.2 Antenna Operation

A 50Ω microstrip line feeds into the semicircular antenna which is designed at 0.80 THz. As discussed in the case of the microstrip line, the Graphene layer is toggled between the ON and OFF states by application of transverse bias. Figure 4.11 shows the current distribution on the patch antenna in the ON and OFF states of the Graphene.

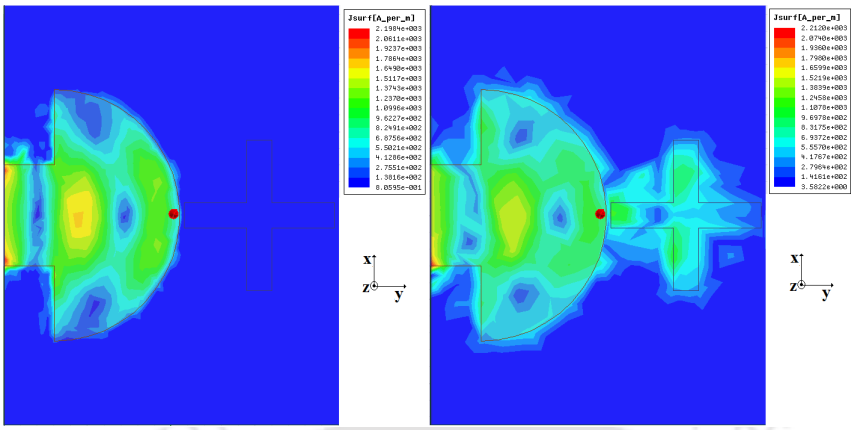

Figure 4.11: Current Distribution on the Antenna in both OFF and ON states of Graphene layer

In the ON state, the conductivity of the Graphene layer is high and the Graphene layer behaves as a neighbouring parasitic patch. Electromagnetic coupling takes place between the main patch and the Graphene layer an sets up a current distribution in the Graphene layer which can be seen in Fig 4.11. This influences the radiation characteristics of the semicircular patch. In the OFF state, there is relatively little or no coupling of energy into the Graphene layer as visible in Figure 4.11. The radiation in the OFF state can, hence, be considered only due to the main antenna.

4.4.3 Results

The variation in the surface current distribution on the antenna due to the coupling in the ON state causes a shift in the principal antenna beam from $\theta = 40^o$(OFF) to $\theta = -40^o$ in the $\phi = 90^o$ plane pattern of the antenna. Moreover, an enhancement of gain by $\sim 4dB$ along $\theta = \pm 50^o$ direction, in the ON state occurs in the $\phi = 0^o$ plane pattern. These variations in the antenna gain can be seen in the plot of the gain patterns in the $\phi = 0^o$ and $\phi = 90^o$ planes in figure 4.

With proper design of parasitic elements and patches, such antenna configurations can be used for beam-forming applications [85], sensor networks and also in medical applications such as in-vivo imaging. Antenna directivity is an important parameter aimed at in 5^{th} Generation (5G) Multiple Input Multiple Output (MIMO) Communication networks. With proper design and placement of parasitic Graphene patches, antenna directivity and beam-control may be

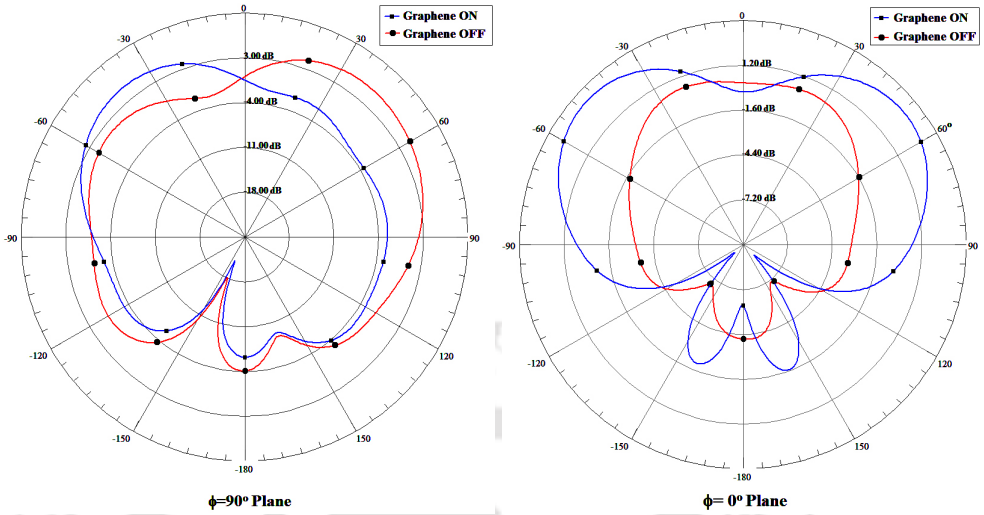

Figure 4.12: Plot of Antenna Gains in the $\phi = 90^o$ and $\phi = 0^o$ planes

achieved as required for a specific application.

4.5 Application of Graphene to Antenna Arrays

Graphene layer as a switch can also find application in antenna arrays. They can be used to create configurable phase shifts in antenna arrays which can be used to control the radiation characteristics of the array. Once such application is a novel 2-element RF level switched beam antenna array system realized through the application of Graphene. The proposed antenna system is designed to operate at 30 GHz. In this design, using Graphene, we try to realize an enhanced, 2x2 Butler matrix based switch beam antenna where the beam switching can be controlled through applied DC voltages. The various issues related to design of such antennas are investigated. The proposed antenna system may find applications in emerging 5G millimeter wave communication technologies such as beam-spaced MIMO and also in wireless sensor networks. A detailed description on the geometry and operation of the 2-element antenna array employing Graphene has been provided in the Appendix B

4.6 Graphene as an RF Switch

Our work utilises the voltage controlled variable conductivity property of Graphene for application as a RF switch. To get an understanding of how voltage controlled Graphene switch

Table 4.3: Insertion Loss and Isolation of Graphene and commercially available switches

Switch Type / Model Number	**IL (dB)**	**Iso. (dB)**
Graphene Patch (here) (30 GHz)	0.087	44.55
Pasternack Enterprises Inc. PE71S2020 [86] (2 GHz - 40 GHz)	5 (Typ.)	30 (Typ.)
Macom-MA4AGSW1A [87] AlGaAs PIN Diode (18 GHz - 50 GHz)	1.2 (Typ.)	~40 (Typ.)
RF-MEMS Metal-Contact Switch [88] (1 GHz - 110 GHz)	0.1-1 (Typ.)	20-56 (Typ.)
RF-MEMS Capacitive Switch [88] (1 GHz - 60 GHz)	0.01-3.1 (Typ.)	5.2-36 (Typ.)

performs as compared to the RF switches used in practice, in Table 4.3, the insertion loss and isolation provided by the Graphene switch are presented along with the values of same parameters as reported in the Data-sheets of PIN diodes used commercially.

Another class of RF switches which are expected to be popular choices for 5G Applications are the RF microelectromechanical system (RF-MEMS) based switches [88]. Broadly, there are two main categories of RF-MEMS switches, metal contact and capacitive. Both of these types have been further sub-divided into series and shunt types. Several interesting structures and geometries of both kinds of RF MEMS switches have been reported in literature. There are a lot of research efforts going on in the area of RF-MEMS switches. A detailed study of the performance and suitability of the state-of-the art RF-MEMS switches for 5G applications has been reported in [88]. In order to understand the performance of the Graphene based switch in comparison to the RF MEMS switches, typical range of values of the isolation and the insertion loss of several of these switches in the specified frequency ranges are presented in Table 4.3.

As seen in the table, Graphene based series switch employed in our application offers good and comparable insertion loss (IL) and isolation values. The Graphene based RF switch does not have the flow of any bias currents due to its voltage controlled nature thereby requiring lower operating power consumptions. It must be pointed out here that the values of the isolation

and insertion loss of Graphene have been calculated based on the present dimensions of the patch used in the present application. Also, additional RF choke elements might be required to protect the DC bias source from spurious RF signals which might get generated during operation of the Graphene switch. The effect of these chokes have not been included in the calculation of isolation and insertion loss values of the Graphene switch. However, Table 4.3 presents the designer with a preliminary qualitative estimate, which would facilitate the choice of such Graphene based RF switches over other options for appropriate applications.

4.7 Conclusion

In this chapter, we presented a brief introductions to Graphene and its important properties in connection to its applications to the field of antennas and electromagnetic waves. Using the dynamic variation in the surface conductivity property of Graphene, we proposed designs for voltage controlled microstrip transmission line and novel antenna designs with desirable characteristics for practical applications.

भारतीय प्रौद्योगिकी संस्थान गुवाहाटी
Indian Institute of Technology Guwahati

5

A Novel Graphene based PMA and Fabrication strategies for Graphene based antennas

In this chapter we propose a novel Graphene based design of a PMA for THz band applications. The analytical model for this Graphene based PMA is similar to that of a conventional PMA, presented in Chapter 3 with the physical parameters of metal replaced by those of Graphene. We use Ansys HFSS^{TM} Version 15 to simulate the proposed antenna and present some important results. We compare the radiation pattern of the PMA, obtained from simulations, with that obtained from the analytical model and find reasonably close agreements in the trend of the radiation patterns. We also simulate variations in the geometrical parameters of the antenna and present the results here. We investigate the effect of electrode shape on the performance of our proposed antenna.

In this chapter, we also look into the aspect of fabrication of Graphene based antennas and present in detail a cost-effective and simple procedure of extracting Graphene nano-particles for use in fabrication of Graphene based antennas. For the purpose of illustration of our proposed technique, we fabricate and measure an ISM band antenna which we present in Appendix C.

5.1 Introduction

Graphene [22], as highlighted in Sections 1.3.2 and 1.4.2, is one of the popular choices in RF and antenna applications at the THz frequency band. Owing to its important and desirable mechanical, physical and electrical properties and the limitations of metallic antennas for THz applications, several new THz band applications employing Graphene have been investigated [89]. Due to the lack of efficient THz signal sources, in recent years, investigations into feeding techniques for "Graphennas" [62] [63] have gained impetus. Literature reports the application of phenomenon of photoconductivity to excite tunable Graphennas for THz band applications [90] which provide a pulsed output. However, to the best of our knowledge little or no literature exists for the application of the phenomenon of optical heterodyning to excite a Graphenna which would provide a more useful continuous wave output. PCAs and PMAs are essentially THz sources and do not require separate THz signal generators.

The proposed design in this work, functions as a basic PMA at the THz band, wherein the Graphene electrodes have been employed to work as tunable voltage-controlled antenna arms

by application of suitable DC bias normal to the Graphene layer [22]. The width, the edge geometry and the doping of the Graphene may be chosen appropriately to avail its variable bandgap property. The dynamic conductivity property of Graphene can be availed to transform the typical PMA into a voltage controlled antenna. Additionally, since Graphene is transparent to the incident laser wavelengths, the overall efficiency of the antenna would be increased when compared with that using copper or other metallic electrodes which are opaque to visible spectrum.

5.2 Antenna Geometry

The geometry of our proposed Graphene based THz PMA, is shown in Figure 5.1. The photoconductive substrate used in the antenna is the LTG-GaAs which has average carrier lifetimes of the order of picoseconds. The LTG-GaAs substrate is typically backed by a normal-GaAs or Silicon layer for additional mechanical strength. To collimate the output beam a silicon lens may be used on the rear side of the substrate *i.e.* the side without the electrodes, as shown in Figure 5.2. Two inter-digitated Graphene electrodes are considered to be deposited onto the LTG-GaAs layer as shown in Figure 5.1. We show a portion of the inter-digitated finger pattern of the proposed antenna in Figure 5.3.

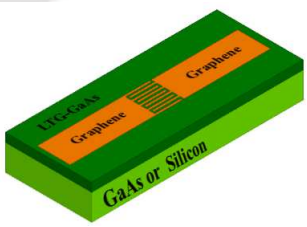

Figure 5.1: Geometry of PMA employing Graphene electrodes

In order to minimize remote phonon scattering in the Graphene layer, in our proposed design, we may use Graphene electrodes deposited over geometrically identical, very thin hexagonal Boron Nitride (h-BN) layer [91]. We show the geometry of the antenna with the h-BN layer in Figure 5.4. Remote phonon scattering is a limiting mechanism which occurs when the dynamics of mobile carriers in Graphene are influenced by the phonons in the substrate [92,93].

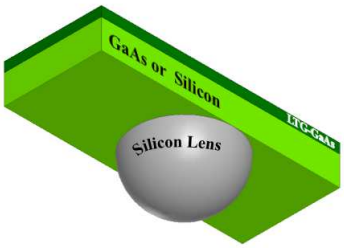

Figure 5.2: Geometry of the PMA with silicon lens

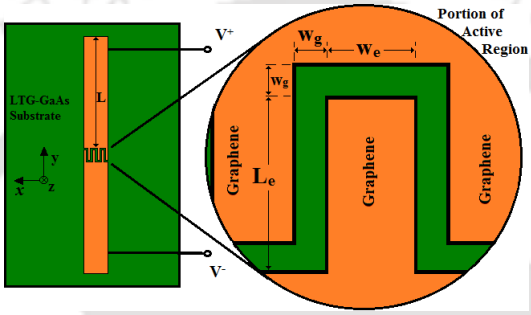

Figure 5.3: Geometry of a single finger in the Graphene PMA

The presence of h-BN enhances the electronic conductivity of Graphene by reducing the remote phonon scattering.

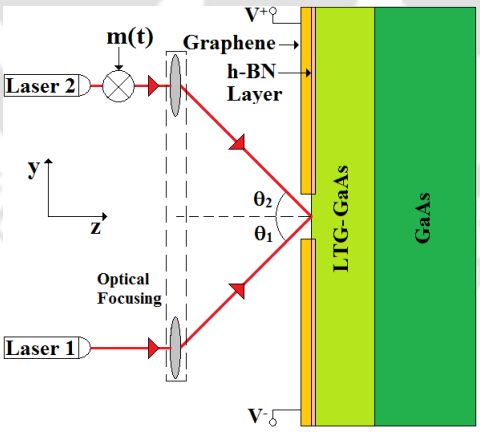

Figure 5.4: Geometry of PMA employing Graphene electrodes over h-BN

It is important to note here that, unlike the conventional metallic PMA, the Graphene inter-digitated electrode fingers are not completely opaque to the incident laser beams. The regions covered by the Graphene, at the inter-digitated electrodes, could also potentially contribute in the photogeneration of carriers and increase the number of charge carriers and the current in the

active region. The increased current results in enhanced efficiency of the antenna.

5.3 Operation of the Antenna

The proposed Graphene based PMA uses the phenomenon of optical heterodyning for its operation. Electron-hole pairs in the LTG-GaAs substrate at the active region are formed as a result of incidence of laser beams from two above-bandgap, moderate power laser sources. The DC bias applied to the Graphene electrodes accelerates these charge carriers in the substrate and gives rise to a time varying current density at the active region. This time varying current density results in radiation from the antenna. We present a pictorial description of the system in Figure 5.5 to depict the operation of the PMA.

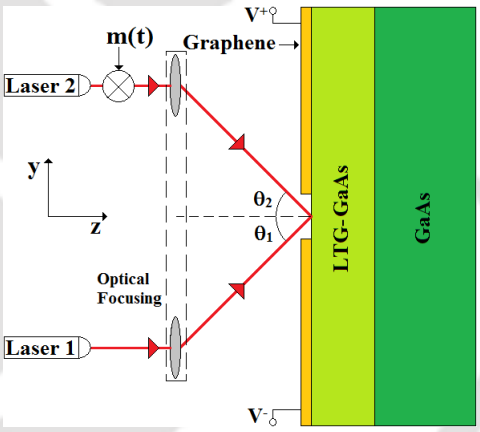

Figure 5.5: Graphene based PMA system Operation

5.4 Analytical model of the antenna

The structure and the operation of our proposed antenna, as described above, is similar to that of a typical PMA with metal electrodes. Owing to this similarity, the analytical model of the metallic PMA can be extended to model the Graphene based antenna. We use the basic 2-ray optical model for the laser incidence, with the basic '*s*' and '*p*' polarized beams, and basic semiconductor device physics to model the carrier generation in the photoconductive substrate. Using the equivalent circuit of the PMA we calculate the output power and investigate its relation to its various geometrical and system parameters shown in Figure 5.5. We derive

the the expressions for the current density and corresponding radiated fields of the Graphene based PMA. Since we have already addressed the analytical model for the conventional PMA in Chapter 3, we shall only present the results for the Graphene based PMA in this chapter.

5.5 Effect of system parameters on output

The output power of a THz PMA is a function of several system parameters such as the total pump power, the beat frequency, $\{\theta_1, \theta_2\}$, ζ and the bias voltage V_{bias}. In similarity to the conventional PMA, described in Chapter 3, the signal source $m(t)$, in Figure 5.5, introduces additional degree of modulation to the output of our proposed design. In Figures 5.6,5.7,5.8,5.9,5.10 and 5.13, we present the influence of these system parameters on the modulation of the output signal of the PMA.

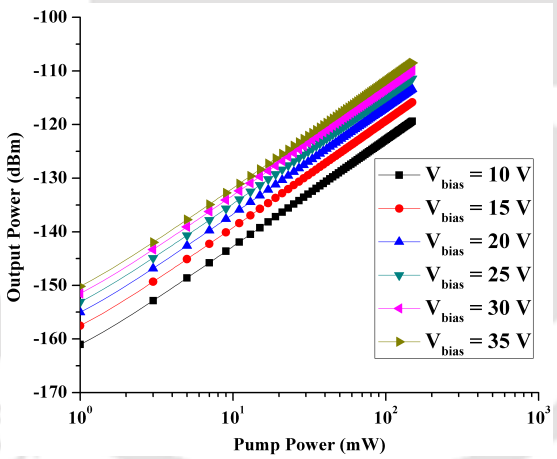

Figure 5.6: Output Power of the PMA at different Pump powers for different bias voltages and $\theta_1 = \theta_2 = \zeta = 0^o, |f_1 - f_2| = 1$ THz

However, for the purpose of modulation of output, we can say that variation in the beat frequency is another significant strategy especially in frequency-hopping type wireless communication links. As seen in the figure, the output power shows significant difference in values for different bias voltages. The plot being at 1 THz beat frequency, the variation of the output with ζ are not discernible as indicated in Figure 5.9. Additionally, we plot the variations in the PMA versus ζ at different pump powers for a beat frequency of 1 THz in Figure 5.11.

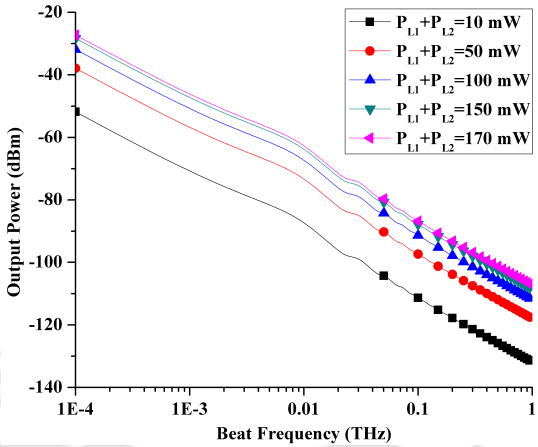

Figure 5.7: Output power as a function of beat frequency at V_{bias} = 35 V at different pump powers.

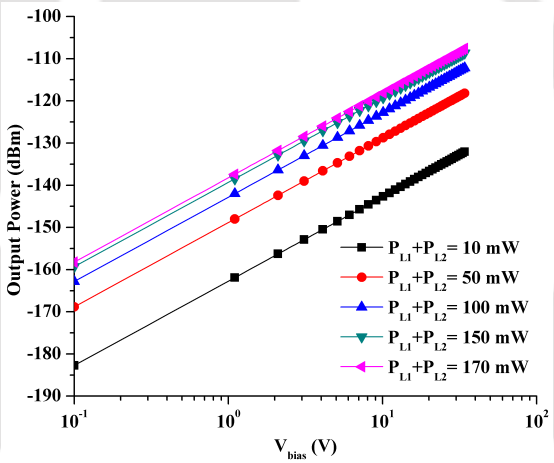

Figure 5.8: Output power as a function of V_{bias} ($\theta_1 = \theta_2 = \zeta = 0^o$) for different pump powers at $|f_1 - f_2|$ = 1 THz

5.6 Simulation of PMA employing Graphene

In order to validate our analytical model of our proposed Graphene based PMA, we simulate the antenna geometry shown in Figure 5.1 using Ansys HFSS Version 15 at a beat frequency of 1 THz. As highlighted in Chapter 4, the Graphene is modelled as a 2-sided conductive surface. The conductivity of the surface can be varied between high (ON state) and low(OFF state) values by application of a transverse DC bias. In the simulations, however, two separate instances of Graphene, with the corresponding values of conductivity, were used to emulate the ON and the OFF states. Graphene in its OFF state would not be sufficiently conductive for

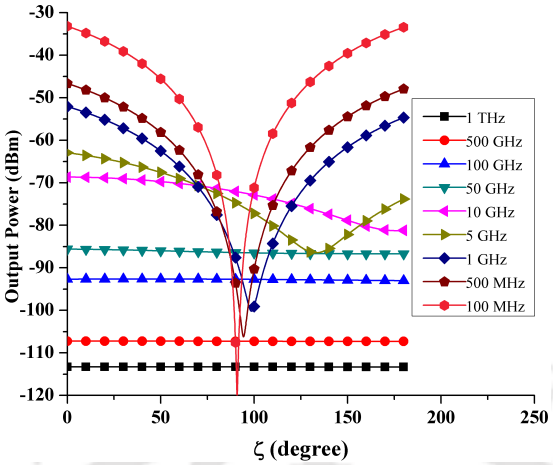

Figure 5.9: Output power as a function of ζ ($\theta_1 = \theta_2 = 0^o$) for different beat frequencies at V_{bias}=30 V and $P_{L1} + P_{L2} = 100\ mW$

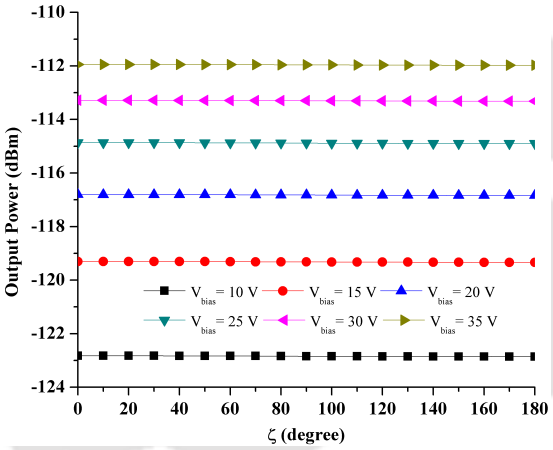

Figure 5.10: Output power as a function of ζ ($\theta_1 = \theta_2 = 0^o$) for different bias voltages at 1 THz with $P_{L1} + P_{L2} = 100\ mW$

application as an effective antenna and so all the presented simulation results are for the ON state of Graphene. We model the photomixing element to be a current source in the simulation and use the value of Graphene conductivity as given in [94].

5.6.1 Antenna geometry used in simulations

We consider a 10-finger and 9-gap [21] inter-digitated pattern of Graphene deposited over the LTG-GaAs grown over gallium arsenide (GaAs). The dimensions of the structure are provided in Table 5.1 The thickness of the LTG-GaAs substrate is taken to be 1μm throughout the study which is reasonably more than the skin depth of LTG-GaAs at 1 THz.

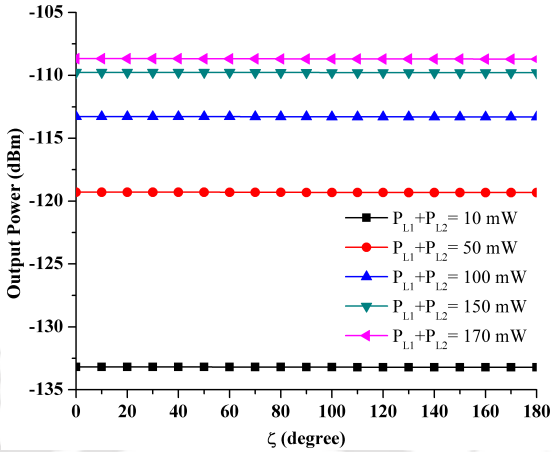

Figure 5.11: Output power as a function of ζ ($\theta_1 = 0^o, \theta_2 = 0^o$) for different pump powers at 1 THz with $V_{bias} = 30V$

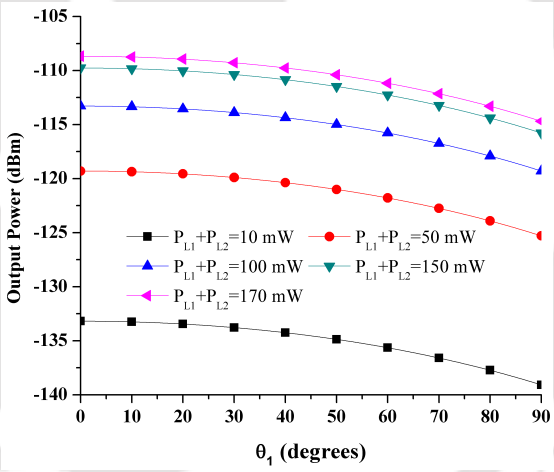

Figure 5.12: Output power as a function of θ_1 at $|f_1 - f_2| = 1$ THz with $\theta_2 = \zeta = 0^o$ and $V_{bias} = 30$ V

5.6.2 Radiation Pattern of the PMA

Calculating the radiated fields, using the analytical model, we plot the normalized radiation patterns, in the principal planes, obtained from simulation and the analytical model, in Figure 5.14 and 5.15

The asymmetry in the shape of the ϕ-plane pattern, is due to the presence of the photoconducting substrate ($\epsilon_r > 1$) beneath the Graphene electrode. The 3dB beamwidth for the above PMA is $\sim 100^o$. We can obtain similar patterns for the "parallel" (p-polarized) polarized laser beams. The phase of the current density and the radiation would depend on the phase of the

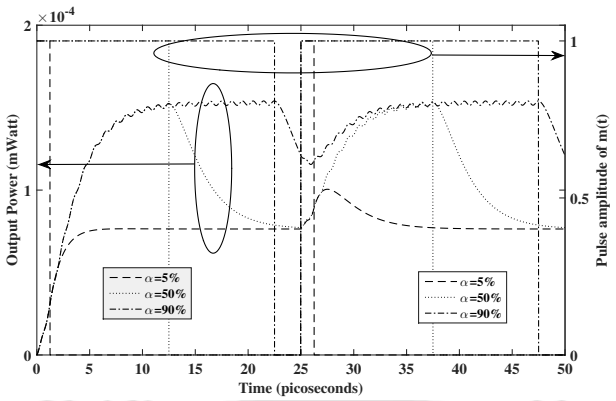

Figure 5.13: Output power as a function of time for different α at $|f_1 - f_2|$=1 THz with $\theta_1=\theta_2=\zeta=0^o$ and V_{bias}=30 V and $P_{L1}+P_{L2}$=100 mW

Table 5.1: Dimensions of the simulated PMA geometry

Dimension	Value (μm)
Length of Electrode	19
Width of Electrode	36
Length of finger in inter-digitated geometry	20
Width of finger in inter-digitated geometry	1
Gap between fingers in inter-digitated geometry	1

incident beams.

5.6.3 Effect of 'w_g' and 'w_e'

The width of the electrodes and the gap between the electrodes in the active region are key parameters which determine the amount of unobstructed light entering into the substrate and thus influences the performance of the antenna. Figure 5.16 and 5.17 show the return loss of the PMA as a function of the finger gap and finger width respectively.

From the similarity in the trend of variation in the return loss it is obvious that the performance of the PMA is a function of the ratio of 'w_e' and 'w_g' rather than the absolute values of the quantities. This inference can be also intuitively drawn from the operating mechanism of the PMA. It can be seen that for higher w_e/w_g ratios, the return loss decreased towards the lower THz frequencies. That is, for a fixed gap, wider electrodes show better matching towards

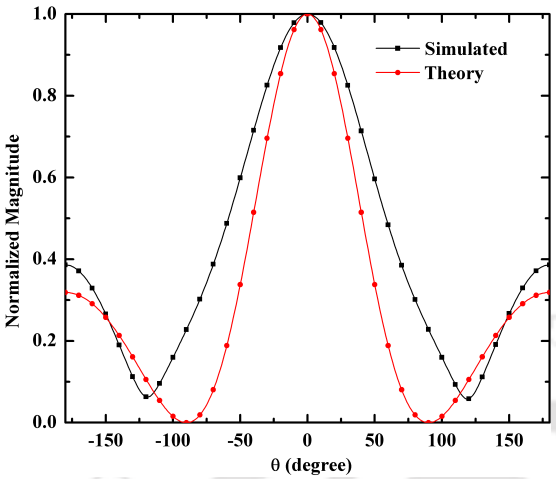

Figure 5.14: Radiation Pattern of THz PMA on $\phi = 90^o$ plane for laser light polarized "normal" (*s*-polarized) to the plane of incidence

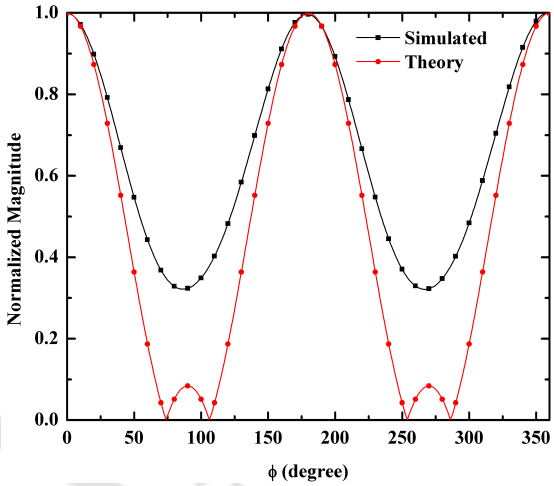

Figure 5.15: Radiation Pattern of THz PMA on $\theta = 90^o$ plane for laser light polarized "normal" (*s*-polarized) to the plane of incidence

the lower THz frequencies. Similarly, for a fixed electrode width, larger gaps improve matching towards the lower THz frequencies.

5.6.4 Effect of the length of the antenna arms 'L'

The purpose of the arm of length 'L' is to provide the bias voltage across the active region of the PMA. The length of this arm plays a role in the performance of the antenna. The return loss of the PMA has been plotted in Figure 5.18 as a function of the ratio L/l_e.

Figure 5.19 shows the radiation efficiency of the antenna as a function of the arm length. From the figures, it is observed that for very long arm lengths, the matching improves but at the cost of significantly low radiation efficiency. Additionally, the PMA shows a wideband behaviour at lower THz frequencies for longer lengths.

These two contradicting scenarios indicate that a trade-off between L and the radiation efficiency has to be ascertained by the designer to achieve the requirements of the desired application.

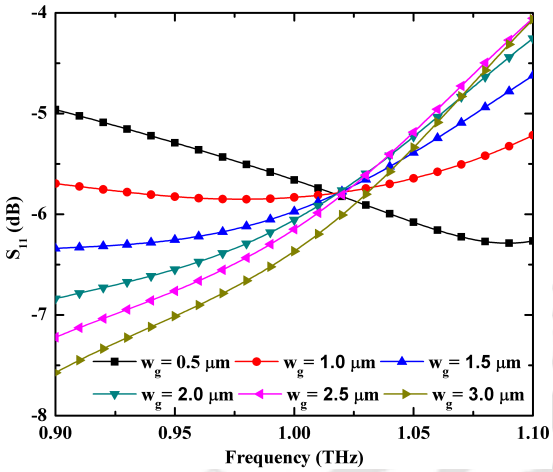

Figure 5.16: S_{11} parameter of the PMA as a function of finger gap w_g

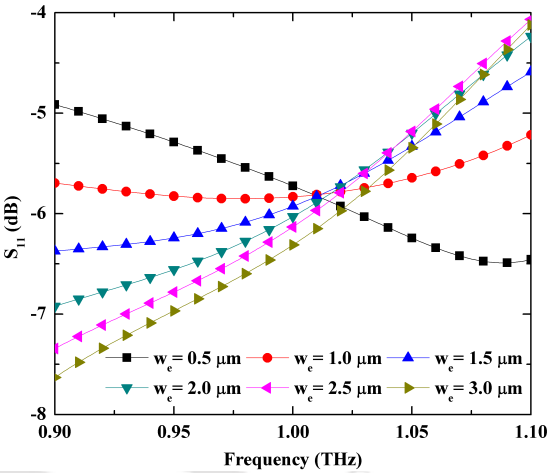

Figure 5.17: S_{11} parameter of the PMA as a function of finger width w_e

5.6.5 Shape of electrodes in the PMA

We investigate the influence of the shape of the electrode in the PMA on the performance of the antenna. The geometries of the PMA assumed for the purpose of the present study are shown in Figure 5.20. The different shapes of the Graphene electrodes are considered to be deposited on the surface of the substrate. The present study being about the influence of electrode shape, we keep the geometry of the inter-digitated region and the substrate dimensions constant throughout the study. Additionally, we also keep the same total length of the PMA for ease of analysis. In these simulations, we use lumped port across the inter-digitated region on the surface of the substrate to extract return loss and input impedance characteristics. However, due to the obvious differences in a conventional antenna and a PMA, the return loss and input impedance need to be redefined for the PMA. Therefore the return loss and input impedance obtained from simulations would provide a qualitative picture rather than a quantitative.

In the circular geometry, the diameter of the circle is equal to the electrode length in the rectangular geometry as given in Table 5.1. Similarly, in the triangular and the trapezoidal geometries, the height is equal to the electrode length in the rectangular geometry.

The dimensions of the substrate considered throughout the study are 110 x 50 x 1 μm and the dimensions of the inter-digitated fingers as in [21]. We perform the simulations for the

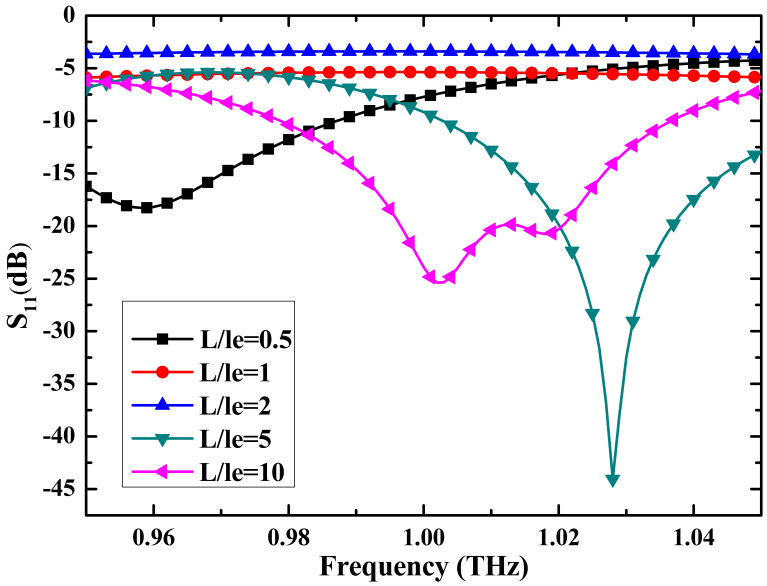

Figure 5.18: S_{11} of the PMA as a function of $\frac{L}{l_e}$

geometries, shown in Figure 5.20 at 1 THz.

5.6.5.1 Return Loss

Since the operation of PMA includes optical excitation in presence of DC bias, scattering parameters may not be a true measure of impedance matching in the PMA. However, assuming a given electrical power to have been available to the antenna, a plot of the S_{11} would be indicative of the performance of the antenna. The return loss characteristics of the various geometries can be determined from Figure 5.21. Slight variations in S_{11} is observed for the different electrode shapes.

The impedance bandwidth of all the structures are almost comparable with the circular geometry showing a slight higher bandwidth.

5.6.5.2 Input Impedance

As in case of the return loss, the true input impedance of a PMA must incorporate the multi-physical scenario in the PMA operation. However, assuming the given electrical input power to be available at the resonant frequency, a plot of the real and imaginary parts of the different geometries would provide a qualitative evaluation of performance of the PMA geometry. A plot

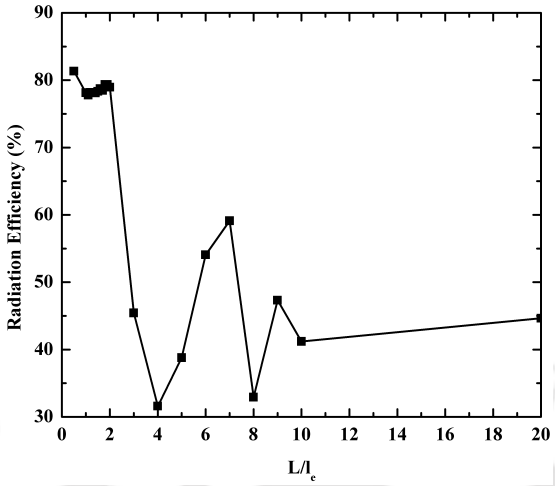

Figure 5.19: Radiation Efficiency of the PMA as a function of the arm length L

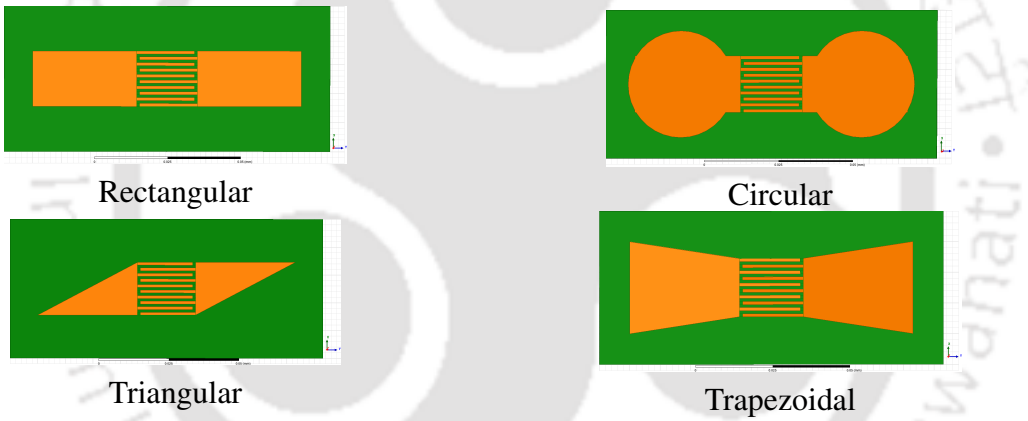

Figure 5.20: Antenna geometries of the different shape of PMA electrodes considered for investigation.

of Z_{11} for the various PMA electrode geometries are shown in Figure 5.22.

The effective length of the path of current increases in case of the trapezoidal and circular geometries than that in rectangular geometry. Therefore, a slight decrease in the resonant frequency can be observed for the trapezoidal and the circular geometries. The resonance condition for the triangular geometry occurs at higher frequency indicating a shorter current path.

5.6.5.3 Directivity

We tabulate the directivity values of the different geometries in Table 5.2. We observe that the directivity values are very close to each other which indicates that variations in the antenna geometry has low influence on the directivity of the antennas.

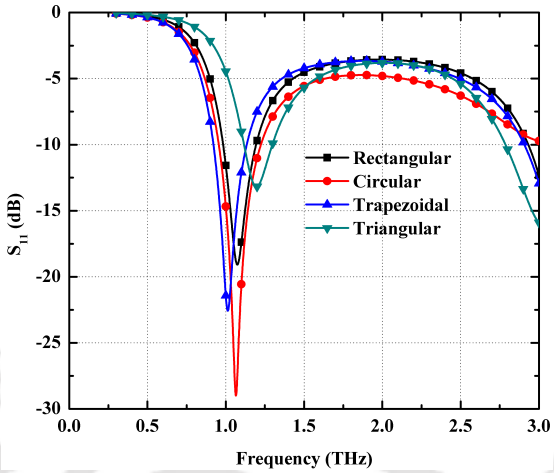

Figure 5.21: S_{11} parameters for various antenna geometries

5.6.5.4 Radiation Efficiency

We show the antenna radiation efficiencies of the PMA geometries in Table 5.2. The trapezoidal geometry shows the highest radiation efficiency. The trapezoidal geometry has the lower resonant frequency and higher resistance at resonance than the other geometries as can be seen from Figure 5.22.

Table 5.2: Radiation efficiencies of the different PMA geometries

Geometry	Directivity (dB)	Radiation Efficiency (%)
Rectangular	2.43	70.27
Circular	2.37	69.82
Trapezoidal	2.29	82.48
Triangular	2.40	59.40

5.6.5.5 Principal Plane Patterns

The co-polarized and cross-polarized components in the radiation pattern of the antenna geometries in the E and H planes are shown in Figure 5.23.

From the figure it can be observed that the radiation pattern remains unchanged for the different antenna geometries which reiterates the fact that radiation occurs from the variation in current density at the inter-digitated region of the PMA and that the electrode geometry contributes predominantly towards impedance matching. This is also obvious in the different amplitude levels in the principal plane patterns. Also, it is observed that the triangular geometry

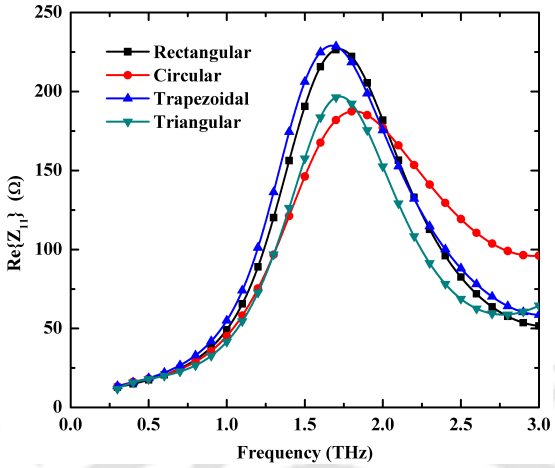

(a)

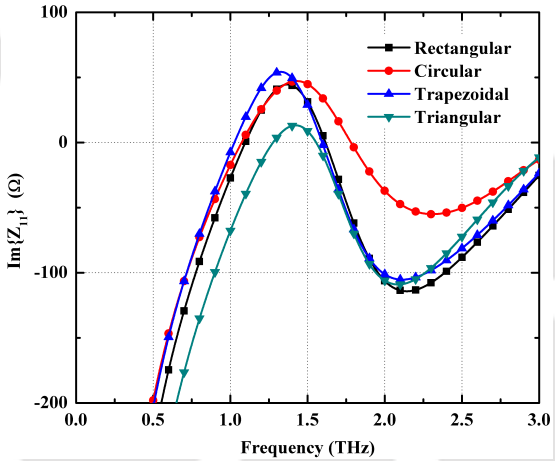

(b)

Figure 5.22: Input Impedance of the various geometries.

shows a higher cross-polarized component in the radiation which can be attributed to the asymmetrically assumed electrode geometry. Simulations were carried out to verify this fact and it was found that cross-polarization levels reduced by a factor of ≥ 2 for symmetrical triangular electrode geometry.

5.6.5.6 Influence of Electrode Width

An investigation on the influence of the width of the electrode was also carried out. Different widths of the electrode were considered and analysed. These widths were increased by a factor of 'r' ($0 \leq r \leq 1.2$) times the basic electrode width which is equal to the total width of 10 fingers and 9 gaps of the inter-digitated electrode structure of the PMA. The return loss and input impedance characteristics for different widths are shown in Figure 5.24

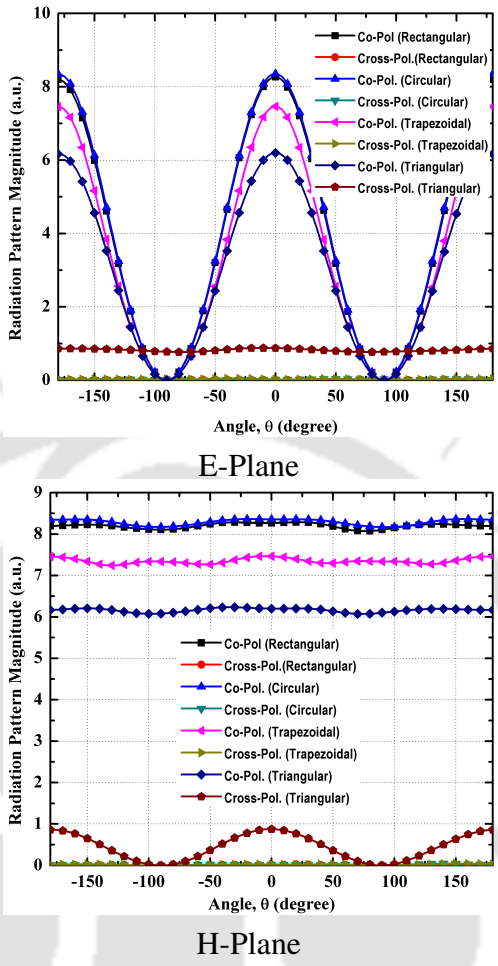

Figure 5.23: Principal plane patterns of the Co-Pol. and Cross-Pol. components of the various geometries.

It can be observed from the figure that increasing the width of the electrode improves the matching at the resonant frequency of the dominant mode. However, the resonant frequency of the next higher order mode is decreased with increasing width.

The radiation efficiency of the PMA is a direct function of the radiation resistance which is dependent on the antenna geometry [34]. Any change in the antenna geometry therefore, influences the radiation efficiency of the antenna. The co-polarized and cross-polarized components of the radiation in the principal planes at various electrode widths are shown in Figure 5.25. Increase in the electrode width improves the directivity and gain of the antenna. This fact if also observed in the values of the directivity and radiation efficiency presented in Table 5.3.

For the purpose of fabrication, Graphene has to be extracted from Graphite using any one of the several reported methods such as mechanical exfoliation, electrochemical exfoliation,

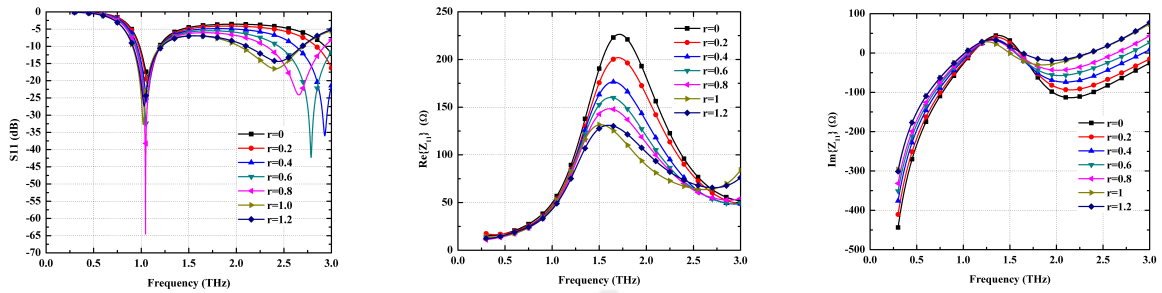

S_{11} $\quad$ $\mathrm{Re}\{Z_{11}\}$ $\quad$ $\mathrm{Im}\{Z_{11}\}$

Figure 5.24: Return Loss and Input impedance of the PMA for different widths

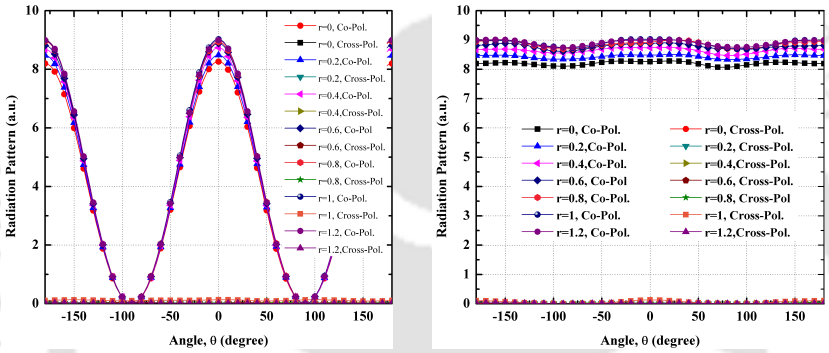

E-Plane $\quad$ H-Plane

Figure 5.25: Principal plane patterns of the Co-Pol. and Cross-Pol. components at various widths.

Hummer's method, liquid phase exfoliation etc. The electrode geometry for the different shapes has to be fabricated either using Graphene printing or direct deposition using chemical vapour deposition (CVD). However, CVD allows limited control on the thickness of the deposition. Biasing connections have to be made and the Lasers have to be positioned as per Figure 5.5 before the measurements. Additionally, proper cooling arrangements for the substrate have to be made using efficient heat sinks since irradiation with two laser sources would generate considerable heat in the substrate.

In the preceding discussions and results, we present the analytical modelling and simulation of a proposed Graphene based PMA. In the following part of the chapter, we shall investigate and present various discussions on the methodologies for obtaining and Graphene and fabrication of antennas using Graphene.

Table 5.3: Directivity and Efficiency variation with PMA electrode width

Factor (r)	Directivity (dB)	Radiation Efficiency (%)
0	2.43	70.27
0.2	2.41	73.46
0.4	2.42	75.79
0.6	2.44	76.95
0.8	2.46	77.87
1	2.45	77.62
1.2	2.41	78.31

5.7 Extraction of Graphene from Graphite

Graphene, in its pristine form, has several potential applications in different fields and, with respect to the electronics industry, it has been claimed to be "the silicon of the 21st century" [12]. However, single-layer Graphene (SLG) is of limited advantage to antenna applications due to two main reasons: (a) the SPP modes on SLG are tightly bound to the Graphene layer [60] and (b) SLG antennas have very low gain. Due to these reasons, we would carry out our investigations with multi-layer Graphene (MLG). Also, almost all practical reported applications have been reported with MLG as the preferred material rather than SLG. Actually, it is inappropriate to call it multi-layer Graphene because Graphene has, conventionally, been defined to be a single layer of Graphite. Therefore we shall refer to the MLG as few layer graphite (FLG) which seems more appropriate.

FLG based antennas are still in the nascent stages of research. The most popular form of FLG used for these applications is a conductive ink which contains FLG flakes in suspensions. These inks can also be used in commercial ink-jet printers to directly print out circuits and components. Such capabilities of these kind of inks have given rise to a new paradigm, "ink-jet" printed electronics [95, 96] based on FLG. We present a discussion on low-cost and effective methodology of extraction of FLG from bulk Graphite. We also propose cost-effective techniques of fabrication of FLG based antennas. To validate our proposal, we fabricate an ISM band microstrip patch antenna on paper substrate using FLG conductive ink and measure its return loss and present the results in Appendix C.

5.8 Methodology

In this section, we highlight the adopted methodology in obtaining the FLG from Graphite and also its characterization using Raman spectroscopy and Field emission-Scanning electron Microscopy (FE-SEM) on Gemini 300 Electron Microscope. A flow-chart outlining the methodology is shown in Figure 5.26.

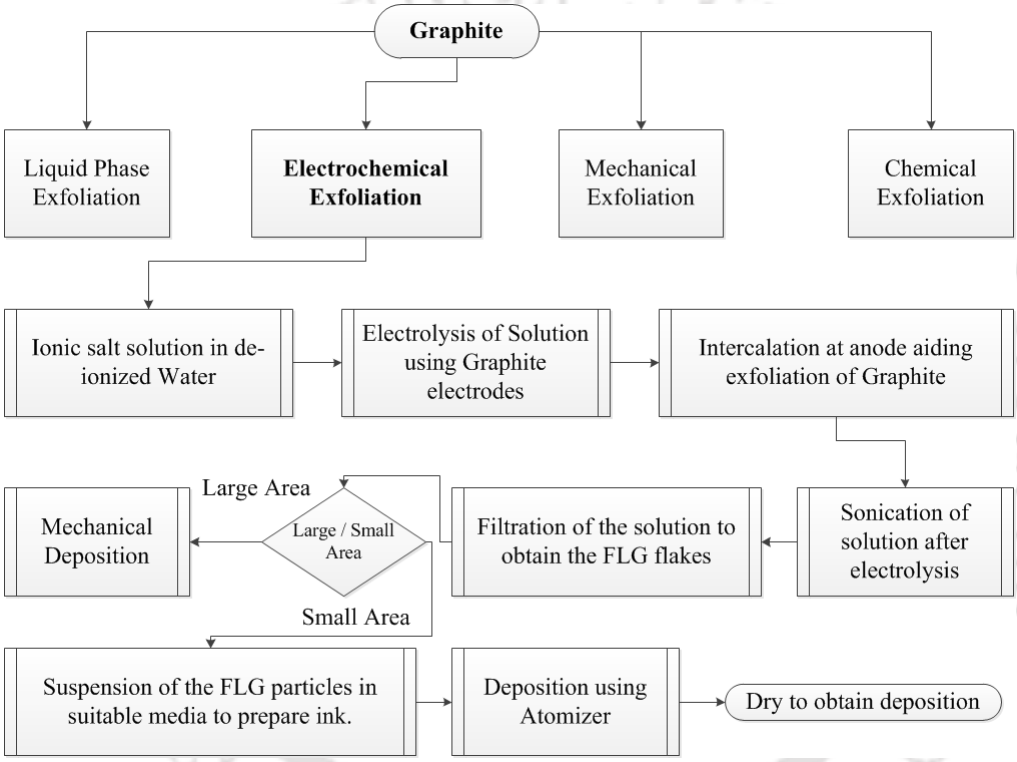

Figure 5.26: Flow Chart showing the methodology adopted in obtaining the FLG based ink from Graphite

In the subsequent sections, we shall discuss the different blocks in flowchart. In Figure 5.26, we have also indicated alternate methods of obtaining the FLG from Graphite. Out of these, we have adopted the electrochemical exfoliation method [97] for our purpose because primarily due to the cost and availability of materials and equipment required for the extraction. A comparison of the cost of different methods for mass production and their quality has been well depicted in [98] as seen in Fig. 5.27.

In the present thesis, we have further tried to minimize on the cost wherever possible in an attempt to make our procedure a cost-effective one as will be evident in the subsequent sections.

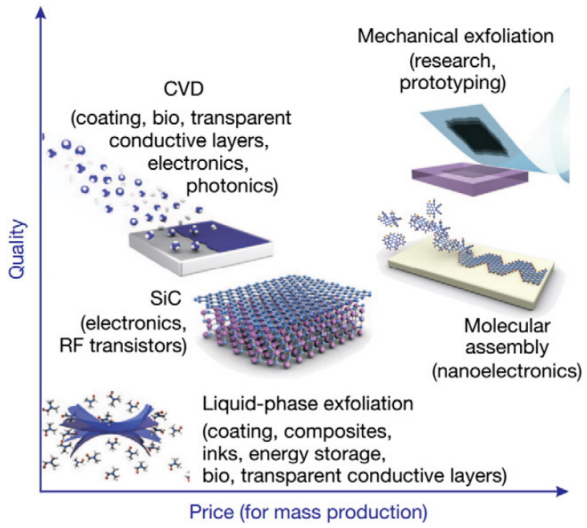

Figure 5.27: Comparison of Different methods in terms of cost versus quality [98]

5.9 Electrochemical Exfoliation of Graphite

In electrochemical exfoliation of FLG from Graphite, we used Graphite of two different forms: Graphite in a plate form and HOPG Graphite in a rod form. An alternate source of Graphite is the carbon rod from a used Zinc-Carbon battery [99]. The various forms were exfoliated and post-processed separately. Both electrodes in our experiments were of Graphite. The Graphite to be exfoliated was connected to the anode. The electrolyte used in all the cases was a 1 M solution of Sodium Sulphate (Na_2SO_4) in water [98]. The DC voltage was obtained by bridge-rectifying the output of the secondary of a 220V/12V rated transformer. In both the cases, the electrochemical exfoliation was carried out in a 500 ml glass beaker and the subsequent sonication was performed in an ultrosonic bath.

The precipitate after sonication was filtered out using filter paper placed over a glass funnel. The wet sample on the filter paper was then dried overnight using a Hot-Air Oven at 65^{o}C. A few images of the experiments have been shown in Figure 5.28.The characterization of the FLG samples obtained from the above exfoliations is discussed in the next section.

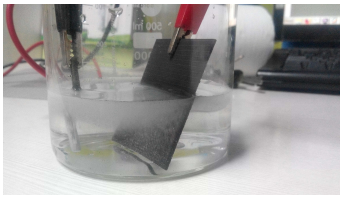

(a)

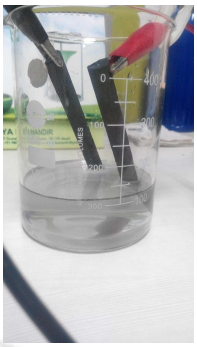

(b)

Figure 5.28: Electrochemical Exfoliation of Graphite in our Laboratory, at IIT Guwahati (a) Plate form (b) HOPG rod

5.10 Characterization of FLG

The dried sample was characterized using Raman Spectroscopy(514nm) and Field Emission Scanning Electron Microscope (FE-SEM, Gemini 300) as shown in Figure 5.29, 5.30, 5.31 and 5.32. These characterizations were obtained at the Central Instruments Facility (CIF), IIT Guwahati.

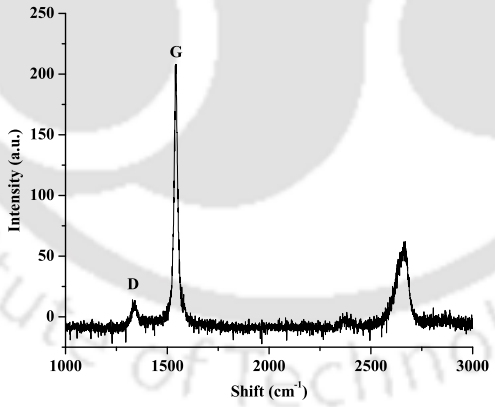

Figure 5.29: Raman Spectrum of FLG sample at 488 nm, obtained at CIF, IIT Guwahati, from 6B pencils

From a review of literature [100, 101], the low I_{2D}/I_G ratio indicates that the FLG sample obtained is quite low in the percentage of SLG flakes due to insufficient exfoliation and therefore needs to sonicated for more time to increase the percentage of SLG flakes. This fact is also noticeable in the SEM images of the samples. Also, the trend of the Raman spectra does not indicate the presence of any impurity in the sample. The FLG sample from 6B pencils was,

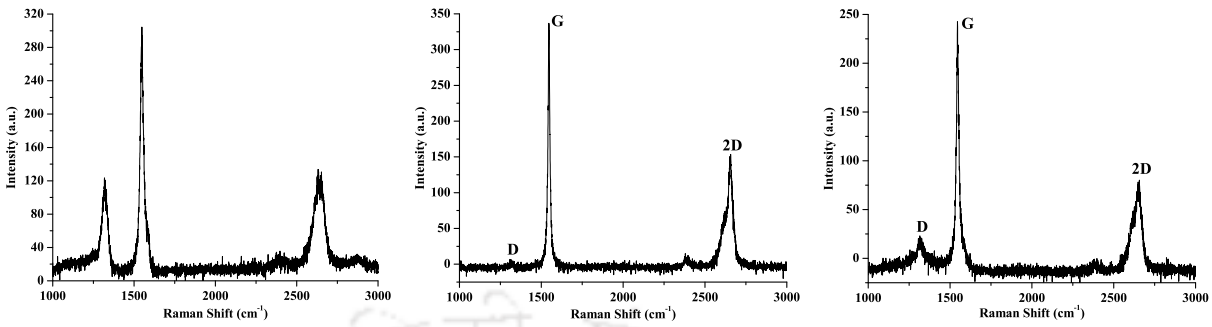

(a) (b) (c)

Figure 5.30: Raman Spectra of FLG samples at 514 nm, obtained at CIF-IIT Guwahati, from (a)6B pencils (b) Graphite Plate (c) HOPG

however, a trial experiment and would not be used for further analysis.

(a) (b)

Figure 5.31: FE-SEM images of FLG sample from Graphite plate obtained at CIF, IIT Guwahati

(a) (b)

Figure 5.32: FE-SEM images of FLG sample from HOPG rod obtained at CIF, IIT Guwahati

5.11 Preparation of FLG based ink

The FLG based ink can be prepared with suitable solvents and printed on a suitable material or deposited onto an appropriate substrate depending on the requirement and constraints of the application. Based on the viscosity of the ink as well as the size of the FLG, it can be also used

in a commercial inkjet printer to fabricate circuits and antennas. Such capabilities enable quick and easy fabrication of low cost electronic circuits and related systems as well as antennas.

Inkjet printable Graphene inks have already been commercialized with potential applications. Several solvents or mixtures of solvents have been reported to disperse the FLGs to make conductive inks with different electrical and thermal properties. However, such commercial inks are inexplicably quite expensive. We have prepared a FLG based ink wherein we have dispersed the FLGs in a mixture of 70%(by wt.) of ethanol and 30%(by wt.) of water with a FLG concentration of 5 mg/mL [102]. However, it has been observed that increasing the water proportion in the solvent leads to a longer dispersion and thereby a better shelf-life of the ink. The presence of alcohol provides and advantage of a fast drying deposition due to the inherent volatility of the alcohol. Therefore, a trade-off has to ascertained prior to dispersion of the FLGs.

5.12 Methods of Depositions of FLG flakes

The FLG based ink can be prepared with suitable solvents and printed on a suitable material or deposited onto an appropriate substrate depending on the requirement and constraints of the application. Based on the viscosity of the ink as well as the size of the FLG, it can be also used in a commercial inkjet printer to fabricate circuits and antennas. Such capabilities enable quick and easy fabrication of low cost electronic circuits and related systems as well as antennas.

As mentioned earlier, inkjet printable Graphene inks have already been commercialized with potential applications. Several solvents or mixtures of solvents have been reported to disperse the FLGs to make conductive inks with different electrical and thermal properties. However, such commercial inks are inexplicably quite expensive. We have prepared our own FLG based ink wherein we have dispersed the FLGs in a mixture of 70%(by wt.) of ethanol and 30%(by wt.) of water with a FLG concentration of 5mg/mL. However, it has been observed that increasing the water proportion in the solvent leads to a longer dispersion and thereby a better shelf-life of the ink. The presence of alcohol provides and advantage of a fast drying deposition due to the inherent volatility of the alcohol. Therefore, a trade-off has to ascertained prior to

dispersion of the FLGs.

5.12.1 Mechanical Deposition

An alternate method of deposition of FLGs, which is popular for large area depositions, is the mechanical method. In the mechanical method of deposition, dry FLG powder is spread on the desired area and mechanical sander is used for even distribution of the thickness of the layer. For small area depositions, we replicate the sanding motion with the finger of the hand and a piece of adhesive tape or paper. The area to be deposited is clearly bounded with masks to avoid spillage. A small amount of FLG powder is dropped onto the tape or onto the desired area and in a circular motion of the fingers, the FLG powder is rubbed on to the area with a mild pressure on the tape or paper as illustrated in Fig 5.33.

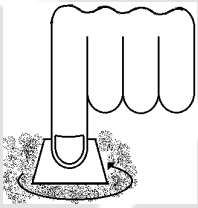

Figure 5.33: Mechanical deposition technique for FLGs

We have tried the above technique and produced a small-area deposition of the FLGs on paper. The deposition has been imaged with Field Emission-Scanning Electron Microscope (SEM), Gemini 300. The images of the edge and the bulk of the deposition are shown in Figure 5.34. The main advantage of this method is that it is simple and cost effective. The drawback

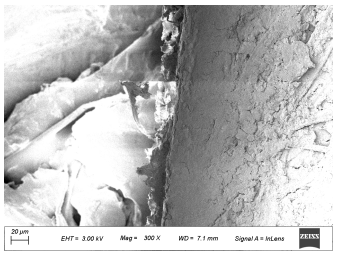

(a) Edge

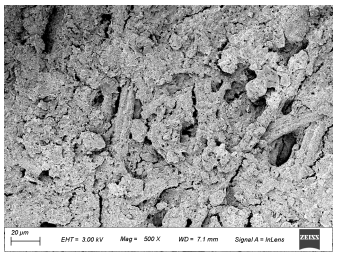

(b) Bulk

Figure 5.34: SEM images of the (a) Edge and (b) Bulk of the mechanically deposited FLGs on paper.

of this technique is the inability to control the thickness of the deposition with sufficient pre-

cision. Especially, for small area depositions, using hand motions might produce thickness variations over the area of deposition. The images in Figure 5.33 show the uneven distribution of the FLG flakes in the bulk region of the deposition. This flaw can be reasonably rectified using our proposed method which is discussed next.

5.12.2 Deposition using atomizer

We propose an alternate and simple method of deposition of FLG based inked onto a desired material. In this method, the FLGs are first dispersed in a mixture of Acetone/Ethanol and Water using ultrasonication and the dispersion is then poured into an atomizer. The atomizer used, is a readily available commercial and low cost plastic bottle. It works on the similar mechanism as a spray-painting system, a deodorant or a perfume bottle. The method is illustrated in Figure 5.35:

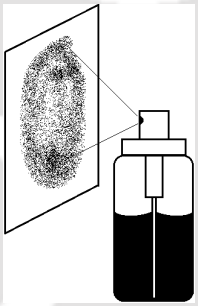

Figure 5.35: Deposition of FLGs using Atomizer

Using this method a sample of deposited FLGs was prepared and imaged using FE-SEM and the images are shown in Figure 5.36:

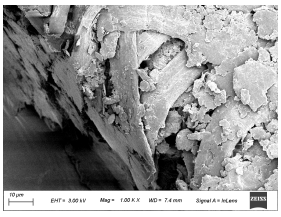

(a) Edge

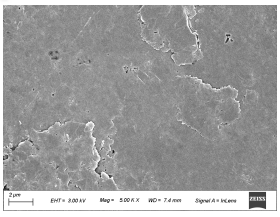

(b) Bulk

Figure 5.36: SEM images of the (a) Edge and (b) Bulk of the deposited FLGs on paper using an atomizer.

As evident in the SEM images, the bulk region is relatively smooth compared to mechanical deposition. The edge region shows undulations which can be rectified using appropriate mask-

ing and clipping techniques. In Appendix C, we present an ISM band antenna fabricated on a paper substrate using the atomizer technique.

5.13 Conclusion

In this Chapter, we proposed a novel Graphene based PMA for THz band applications. Extending the model for a conventional PMA, we presented important results for the Graphene based PMA. Using Ansys HFSS^{TM} we simulated our proposed antenna geometry and presented investigations on the influence of geometrical parameters of the antenna on its characteristic. Subsequently, we also presented a discussion on a low-cost and effective method of extracting FLG flakes from bulk Graphite. We also proposed a cos-effective technique of deposition of FLG based conductive ink on desired substrate for fabrication of FLG based antennas.

6

Conclusion and Future Works

In this thesis, we focus on the various issues related to the design of antenna systems in the THz band which is an essential component in THz sources and detectors from a wireless communication stand point. We also discuss a relatively new material, Graphene, and investigate its application to the conventional antenna technology. We also discuss the methodologies of obtaining Graphene and propose techniques of fabrication of Graphene based antennas. We summarize the contributions of the thesis in Section 6.1 and also highlight possible future direction of research endeavours in the Section 6.2.

6.1 Summary of Contributions

- **Analytical model of radiation from THz PMAs:** We propose an alternate, simple and generalized analytical model of the radiation from a THz PMA which combines the multiphysical scenarios involved in the operation of the PMA.

- **Signal Modulations in the THz PMA:** We investigate possible strategies to incorporate modulation in the PMA output which crucial for the PMA to be suitable for applications in wireless communications. We introduce novel technique of modulating the output of the PMA by incorporating an additional modulating signal component into the PMA system.

- **Application of Graphene to conventional antenna systems:** We proposed novel microstrip transmission line, antenna and antenna array designs employing Graphene which enables dynamic variation and control in their performance characteristics of these designs. Use of Graphene endows voltage controlled operation which has potential applications in several fields.

- **Extraction of GNPs and fabrication of GNP based antennas:** We discuss simple and cost-effect methodology of extracting GNPs from bulk graphite and preparation of GNP based conducting inks which are very useful in the electronics industry. We characterize these GNP samples with sophisticated imaging and spectroscopic techniques to ensure sample purity. We also introduce an alternate and low cost methodology of deposition of

GNP based inks on desired substrates for fabrication of GNP based antennas.

6.2 Scopes of Future Research Endeavours

In this thesis, broadly, we have attempted investigate two major directions towards realization of wireless communications in the THz frequency band.

The first direction is the investigation of continuous-wave sources in the THz band within which we proposed the analytical model for the PMA. However, the main prevalent bottle-neck of PMAs and PCAs are the low efficiency of these photoconductivity based sources. Although there are several advantages of using PCAs and PMAs, the popularity of these sources depend on their capability to efficiently convert the optical power to electrical radiated power. We have highlighted several factors that can influence the efficiency of the PMA in Section 3.10. A detailed investigation involving optics as well as device physics is an area which needs further probe to yield more efficient PCAs and PMAs suitable for application in varied fields. From an antenna stand-point, a frequency domain analysis of the PMA is very important part of an antenna analysis. However, due to the multi-physics involved in the operation of the PMA, a proper domain definition of several conventional antenna parameters are not available and need to be investigated. Influence of thermal effects in the substrate on the output of the antenna also has not been adequately addressed.

The second direction is the search of novel materials for antenna applications at the THz frequency band wherein we discuss the characteristics and applications of Graphene. We have proposed Graphene employed antenna designs which provide dynamic control over their performance characteristics by application of DC bias. Investigations on the other such designs employing Graphene can also be carried out for potentially important results. However, as discussed earlier, a detailed frequency domain analysis of Graphene employed antennas and a proper design procedure for such antennas would be a potentially significant direction of future research. Additionally, investigations on other candidate materials for THz band applications such as High Resistivity Silicon, which has a low loss tangent and high effective dielectric constant, would be worthwhile and useful topic for a future research to the work presented in this

thesis.

A

Appendix A

A.1 Radiated Fields from PMA

The expressions for some of the terms used in the Chapter 3 are given below:

$$P(\omega) = \Bigg[P_{L1}cos\theta_1 + P_{L2}cos\theta_2 + \frac{\sqrt{P_{L1}P_{L2}}}{\sqrt{1+\omega^2\tau^2}}(cos\theta_1 + cos\theta_2)cos(\omega t - y(k_1 sin\theta_1 + k_2 sin\theta_2) - \zeta - tan^{-1}(\omega\tau))\Bigg] \tag{A.1}$$

$$Q(\omega_1,\omega_2, V_{bias}) = \Bigg[\sqrt{2P_{L1}\eta_0}cos\theta_1 cos(\omega_1 t - k_1 y sin\theta_1) + \sqrt{2P_{L2}\eta_0}cos\theta_2 cos(\omega_2 t + \zeta + k_2 y sin\theta_2) + \frac{V_{bias}}{w_g}\Bigg] \tag{A.2}$$

$$F_{1\theta}(\theta,\phi) = -\Bigg\{\frac{cos^2\theta}{-cos\theta + (n^2 - sin^2\theta)^{\frac{1}{2}}} + sin^2\theta cos\theta \frac{-cos\theta - (n^2 - sin^2\theta)^{1/2}}{-n^2 cos\theta + (n^2 - sin^2\theta)^{1/2}}\Bigg\} sin\phi \tag{A.3}$$

$$F_{1\phi}(\theta,\phi) = \frac{cos\theta cos\phi}{cos\theta - (n^2 - sin^2\theta)^{\frac{1}{2}}} \tag{A.4}$$

$$F^1_{2\theta}(\theta,\phi) = \left\{ sin^2\theta cos\theta \frac{(1-n^2sin^2\theta)^{\frac{1}{2}} - ncos\theta}{n(1-n^2sin^2\theta)^{\frac{1}{2}} + cos\theta} + \frac{cos^2\theta}{(1-n^2sin^2\theta)^{\frac{1}{2}} + ncos\theta} \right\} sin\phi \tag{A.5}$$

$$F^1_{2\phi}(\theta,\phi) = -\frac{cos\theta cos\phi}{(1-n^2sin^2\theta)^{\frac{1}{2}} + ncos\theta} \tag{A.6}$$

$$F^2_{2\theta}(\theta,\phi) = \left\{ sin^2\theta cos\theta \frac{(n^2sin^2\theta-1)^{\frac{1}{2}} + jncos\theta}{n(n^2sin^2\theta-1)^{\frac{1}{2}} - jcos\theta} - j\frac{cos^2\theta}{(n^2sin^2\theta-1)^{\frac{1}{2}} - jncos\theta} \right\} sin\phi \tag{A.7}$$

$$F^2_{2\phi}(\theta,\phi) = -\frac{cos\theta cos\phi}{(n^2sin^2\theta-1)^{\frac{1}{2}} - jncos\theta} \tag{A.8}$$

B

Appendix B

B.1 2-element Antenna Array Employing Graphene

In this work, we propose a radio-frequency (RF) level switched beam antenna array system with digital phase shifting realized through application of Graphene. The proposed system alleviates the limitation of a conventional Butler matrix technique by providing a wider beam switching capability with a relatively lower number of elements. Although, the proposed technique compromises on the orthogonality of transmitted and received signals available with a conventional technique, a proper isolation and time-division between transmission and reception can be employed at the system level to solve the above problem. Such an arrangement would be excluded from the antenna structure and hence would not compromise on the space

The simulations in this work have been performed using Ansys HFSS^{TM} Version 15.

B.2 Geometry of Proposed Antenna Array

A $L \times W$ 2-element antenna array is designed on a grounded silicon dioxide ($SiO_2, \epsilon_r = 4$) substrate fed by a coplanar branch line coupler (as used in design of Butler matrix) through four coplanar patches of Graphene (S_1, S_2, S_3, S_4) as shown in Figure B.1. The values of the

Table B.1: Dimensions of the Antenna Array Geometry

Antenna parameter	**Value**
Length of Patch(L)	2.641 mm
Width of Patch (W)	3.162 mm
Height of Substrate (h)	0.381 mm
Width of microstrip line (m)	0.838 mm
Inset length (d)	0.997 mm
Notch Width (g)	0.083 mm
Length of Substrate (Ls)	14 mm
Width of Substrate (Ws)	14 mm
Length of Ground plane (Ls)	14 mm
Width of Ground Plane (Ws)	14 mm
Thickness of Patch (t)	60 nm
Thickness of Graphene layers (gr)	60 nm

various geometrical dimensions in Figure B.1 have been presented in Table B.1.

Two wave-ports P_1 and P_2 are used as input to the antenna array. All the widths of the feed, the transmission lines, the inset feed to the antenna element and the input ports have been calculated according to 50Ω reference. The values of the geometrical parameters mentioned in Table B.1 have been optimized as per tolerances to produce optimal results. The distance between two antenna elements is chosen such that mutual coupling between the antenna elements is very small.

B.3 Antenna Operation

The excitation at any input port $P_i; i = 1, 2$ feeds the two antenna elements through the coupler which divides the power equally and provides a phase shift of $\frac{\pi}{2}$ between the output ports. The conductivities of the Graphene patches are changed by application of transverse DC bias voltages of 0V and 15V, so that the the Graphene patches switch between the ON and OFF state as discussed in Chapter 4.

The two quadrature phase signals from the output of the branch line coupler is inset-fed into the two antenna elements through appropriate Graphene (ON state) patches, thereby producing additional path difference and a corresponding phase difference between the antenna inputs. More number of such Graphene patches can be introduced adjacently to produce multiple path

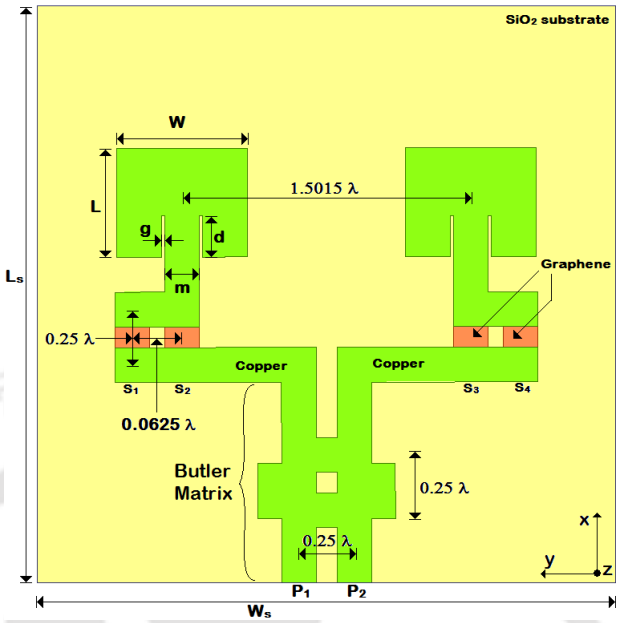

Figure B.1: 2 element array using Graphene and coplanar branch line coupler

differences thereby increasing the number of phase shifts possible among the inputs to the antenna elements. Such arrangements increase scanning precision as well as dynamic capability of the design while also increasing the complexity of detection and an associated increase in detection error.

B.4 Results and Discussion

$2^4 \times 2$ combinations of ON/OFF states (OFF⇒0, ON⇒1) among $S_1 - S_4$ are possible, thereby providing total number of 32 phase shift possibilities for this 2-element antenna array. The angles of maximum radiation for all the combinations of $S_1 - S_4$ and for inputs at ports 1 and 2 have been tabulated in Table B.2.

Clearly, from the Table , we can see that the number of angles of maximum radiation are indeed several times higher than than that a conventional 2-element beamforming antenna array fed through a 2x2 Butler Matrix. The return loss characteristics of the 2-element antenna array structure for excitations at Port 1 and 2 are presented in figures B.2 and B.3 respectively.

All possible combinations for excitations on both ports have been simulated and a few of the beam switching behaviours of the antenna array structure is shown in figures B.4,B.5 and

Table B.2: Angles of Maximum Radiation in $\phi = 90^o$ plane

Excitation at Port 1			Excitation at Port 2		
Comb.	Max. Gain (dB)	Angle (Deg.)	Comb.	Max. Gain (dB)	Angle (Deg.)
0000	2.027	19	0000	1.949	-19
0001	3.394	18	0001	3.638	-20
0010	2.823	20	0010	2.634	-20
0011	3.109	-39	0011	3.171	-20
0100	2.609	20	0100	2.857	-20
0101	3.874	20	0101	4.352	-21
0110	3.420	20	0110	3.435	-21
0111	3.228	-39	0111	4.147	-21
1000	3.717	19	1000	3.514	-19
1001	4.442	18	1001	4.414	-18
1010	4.347	20	1010	3.897	-20
1011	4.189	14	1011	3.873	-23
1100	3.274	21	1100	2.723	39
1101	3.875	22	1101	4.293	-14
1110	4.050	21	1110	3.297	40
1111	2.780	11	1111	2.937	-10

B.6 below.

As can been seen from Table B.2, the beam covers a span from$\sim -39^o$ to $\sim +40^o$. This can be seen in Figure B.7 where we plot the antenna gain pattern in the $\phi = 90^o$ plane for corresponding excitations as presented in the Table B.2.

Some of the salient observations made while investigating the antenna system are discussed below:

Firstly, the resonant frequency for certain combinations deviates from 30 GHz. This is primarily because of the presence of Graphene in the transmission line path which also determines the quality of power coupling into the antenna inset feed line.

Secondly, with two radiating elements the main lobe beamwidth is quite wide and would result in lower detection efficiency in the detection mode of the antenna. A narrower beam would mitigate such malefics and we are investigating this issue.

Thirdly, in the detection mode, when signal from a particular direction is received, it would be difficult to decide as to which combinations of $S_1 - S_4$ to be used. A reasonable solution

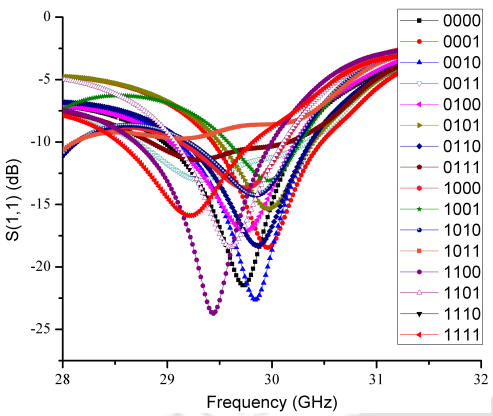

Figure B.2: S_{11} Parameters for all combinations corresponding to excitation at Port 1.

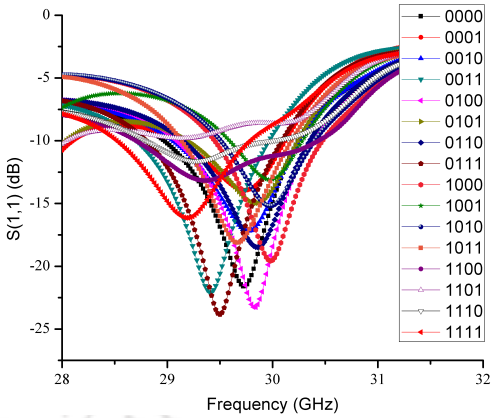

Figure B.3: S_{11} Parameters for all combinations corresponding to excitation at Port 2.

would be to run a maximum likelihood algorithm to detect the correct combination and the subsequent detection of the received signal.

Lastly, although all the combinations of $S_1 - S_4$ do not produce beam shifts, they increase the gain in certain directions which may be helpful in improving the received Signal-to-Noise Ratio (SNR) during detection from those directions.

Besides Table 4.3, comparative simulations of return loss characteristics, of the hybrid coupled antenna array, have also been performed in order to study the antenna characteristics using the various types of switches listed in Table 4.3. Owing to absence of specific data on the respective data-sheets, these simulations have been carried out assuming resistive models for the commercially available. These resistive models have been reverse calculated using the insertion loss and isolation values given in Table 4.3. The simulation results would vary if a complex modelling of the commercial devices is incorporated in the simulations. Due to space constraints, results for only a few combinations have been presented here in Figures B.8, B.9 and B.10.

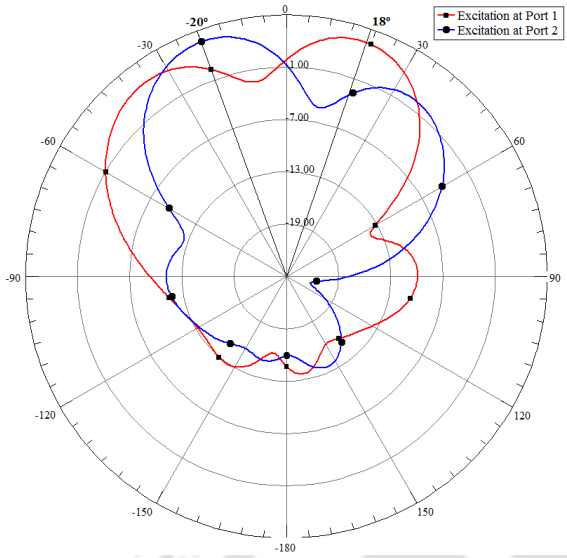

Figure B.4: Plot of Antenna Gain on $\phi = 90^o$ plane for combination 0001 corresponding to excitations at Port 1 and 2

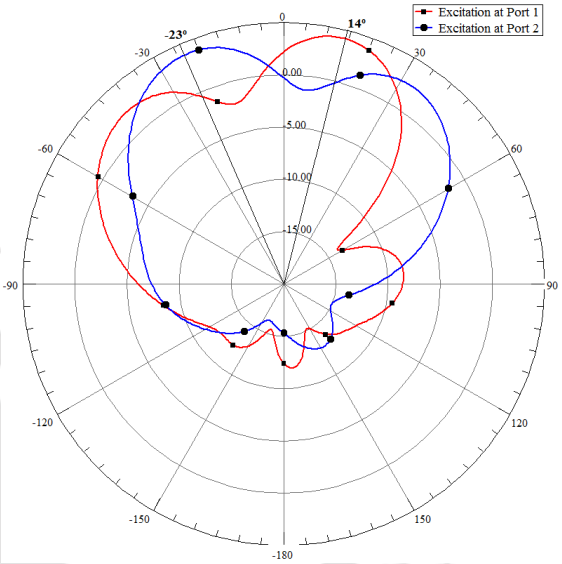

Figure B.5: Plot of Antenna Gain on $\phi = 90^o$ plane for combination 1011 corresponding to excitations at Port 1 and 2

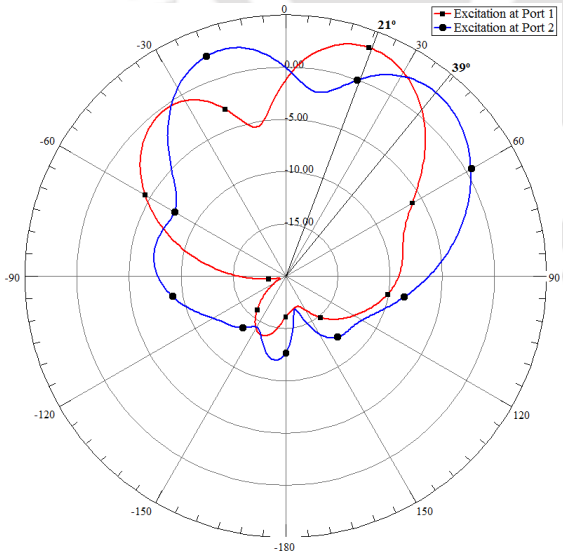

Figure B.6: Plot of Antenna Gain on $\phi = 90^o$ plane for combination 1100 corresponding to excitations at Port 1 and 2

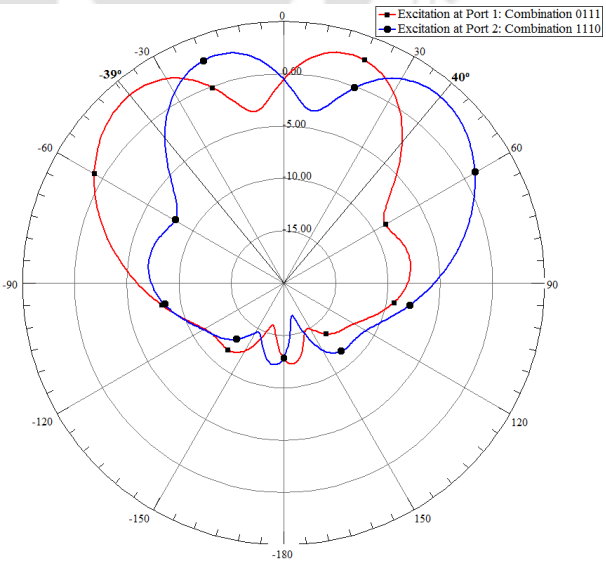

Figure B.7: Plot of Antenna Gain in $\phi = 90^o$ plane showing the angular coverage range of the 2-element beamforming array.

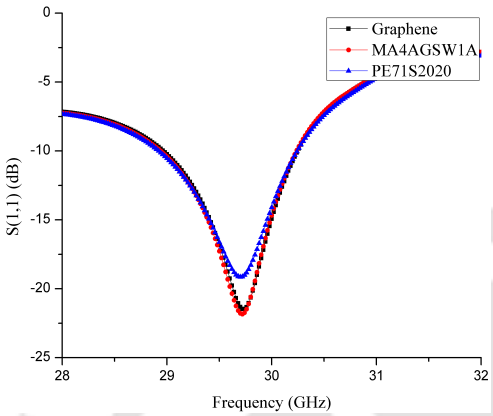

Figure B.8: S_{11} corresponding to combination 0000 and excitation at Port 1.

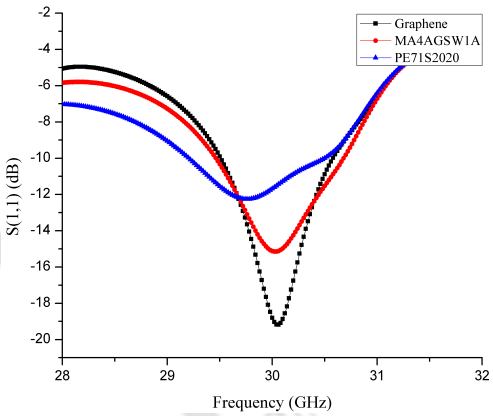

Figure B.9: S_{11} corresponding to combination 0001 and excitation at Port 1.

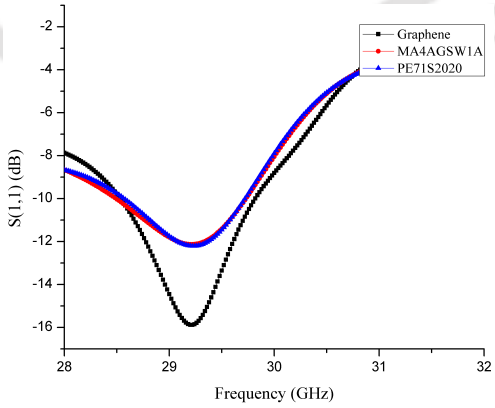

Figure B.10: S_{11} corresponding to combination 1111 and excitation at Port 1.

C

Appendix C

C.1 Design and Analysis of FLG based ISM band Antenna

The design of a conventional microstrip antenna includes several important steps such as selection of appropriate material and size for the substrate, calculation of the patch dimensions and design of the feed. Accordingly, we present the procedure adopted in design of the FLG based antenna in the subsequent sections.

C.2 Preparation of Antenna Substrate

The material for fabricating the antenna being a conductive ink and paper being readily available and also low cost, we selected a paper substrate. The dimensions of the substrate are *100* x *100* x *2 mm*. To achieve the required substrate thickness, we glued several A4 sheets together and cut out the lateral dimensions from this glued stack of papers using a scale and an exacto knife. The dielectric constant of paper is 2.7 which also makes it a good choice for substrate of microstrip antennas. The presence of layers of glue and minute inter-layer air-gaps within a substrate thickness of *2 mm*($\ll\lambda \approx 122.45mm$) would contribute very less to an effective dielectric constant. Therefore, we assume the bulk substrate dielectric constant to be

equal to that of paper.

C.2.1 Fabrication of the Ground plane

The ground plane in the antenna was made by sticking copper tape onto the back of the paper substrate. The copper tape was *10 mm* wide. A total of 10 strips covered the area of the ground plane. The continuity among the strips was ensured using a multimeter.

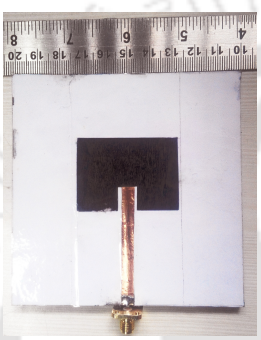
Front

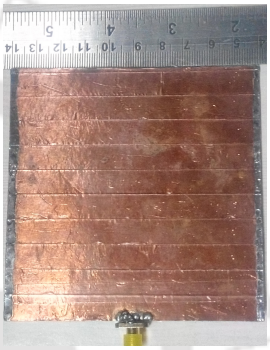
Back

Figure C.1: Microstrip antenna fabricated using GNP based ink and an atomizer.

C.3 Deposition of Antenna Geometry

After ascertaining the dimensions of the patch (*33* x *45 mm*) and the feed for the antenna to resonate at the ISM band, we printed a mask on a paper and the portions of the antenna and feed were cut out. The mask was then covered with household adhesive tape and then glued to the top of the substrate. The adhesive tape cover makes the unmasking process easier. The FLG based ink was poured into an atomizer bottle and sprayed. For quick drying we used a commercial hair-dryer. This process was repeated several times until a sufficiently thick layer of the material was formed on the substrate at the patch and the feed line regions. The mask was then gently lifted off leaving being the deposited antenna and the feed line. However, to achieve a stable contact of the deposited feed-line and the flat-flange SMA connector, we laid a copper strip of identical width over the feed-line which is seen in Figure C.1. The width of the feed line is *5.4 mm*. The analysis of the power transfer characteristics between the copper and the deposited multi-layer Graphene is a topic of future investigation and would be reported later.

The discrepancy in Fig. C.2 between the simulated and the measured results can be attributed

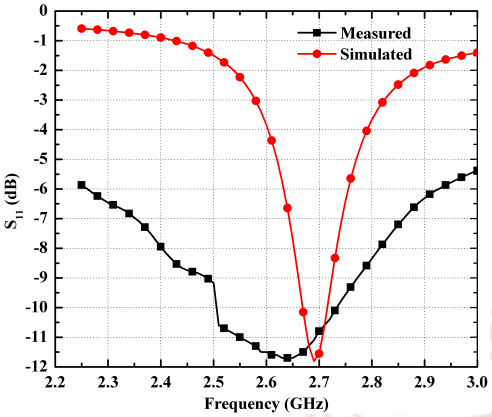

Figure C.2: Simulated and Measured S_{11} of the antenna

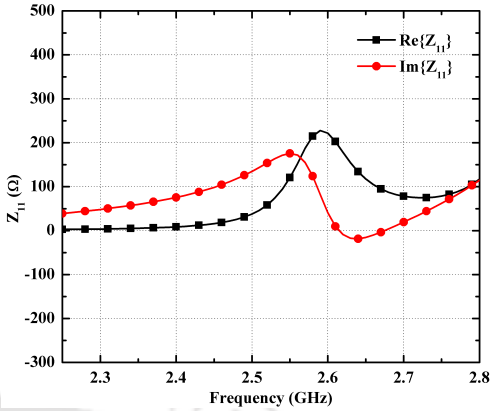

Figure C.3: Real and Imaginary parts of the input impedance of the antenna

to several contributing factors:

- **Conductivity of the substrate:**The actual value of the substrate conductivity was not practically measured and was assumed from reported literature. Since the bandwidth depends on the conductivity, this could be one of the factors of mismatch.
- **Antenna Structure:**Although the dimensions in the fabricated prototype and the simulations were made as identical as possible, edge imperfections resulting from spraying the ink from the atomizer could not be taken care in the simulation.
- **Substrate Parameters:**The substrate was prepared by stacking sheets of A4 size papers glued together and then cutting out the required dimension piece from the stack. However, in simulations we assumed a bulk paper substrate with identical dimensions. The actual values of the fabricated substrate dielectric constant and loss tangent values could not be measured and hence, could not be included into the simulations.

C.4 Simulation Results of the Antenna

It must be noted that the present antenna has been fabricated merely with purpose of a proof of concept and more practical antennas would be fabricated subsequently. With a backdrop of this notion, the fabricated antenna is being put through measurements and the measured results would be communicated subsequently. However, results from simulation of the design have been presented below.

The scattering parameters at the input port of the antenna and the input impedance of the antenna are shown in Figure C.2 and C.3 respectively. The radiation pattern of the antenna is shown in Figure C.4 which shows a maximum gain of ≈ 6.4 dB. The total, co-pol and cross-pol gain patterns of the antenna in the $\phi = 0^o$ and $\phi = 90^o$ planes are shown in Figure C.5.

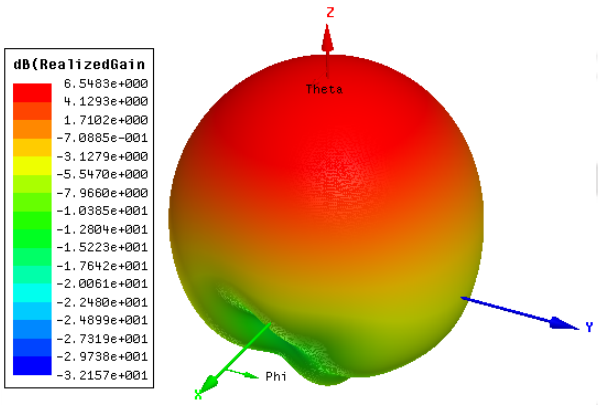

Figure C.4: Radiation pattern the Antenna

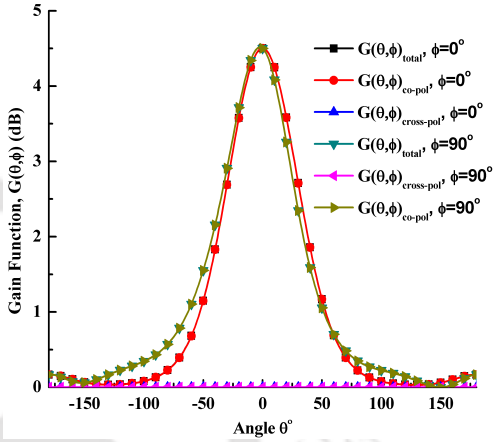

Figure C.5: Gain Function, G(θ, ϕ) plot of the Antenna

भारतीय प्रौद्योगिकी संस्थान गुवाहाटी
Indian Institute of Technology Guwahati

List of Publications

Journal Publications

- M Bharadwaj, J Prajapati, R Bhattacharjee, "Novel Graphene based Antennas for the Terahertz Band," *Semiconductor Science and Technology, IOP Publishing*, 2018, 34, 014003 **(Chapter 5)**
- M Bharadwaj, J Prajapati, R Bhattacharjee, "Analytical modelling of Terahertz Photomixing Antennas," *The IETE Journal of Research, Taylor & Francis*, pp. 1–12, 2019 **(Chapter 3)**

Conference Publications

- M Bharadwaj, J Prajapati, R Bhattacharjee, "Investigation on the Effect of Electrode Shape on the performance Terahertz Photomixing Antenna employing Graphene electrodes," *2nd IEEE-INAE Workshop on Electromagnetics, Thiruvananthapuram, Kerala*, 2018 **(Chapter 5)**
- M Bharadwaj, J Prajapati, R Bhattacharjee, "Analytical Modelling of carrier concentration and conductance in Terahertz Photomixing Antennas," *2017 IEEE Applied Electromagnetic Conference*, Aurangabad, pp. 1–2, 2017. **(Chapter 3)**
- M Bharadwaj, J M Reddy, R Bhattacharjee, "Switched Beam Antenna System Design at Millimeter Wave Band Employing Graphene," *2016 IEEE Annual India Conference (INDICON)*, Bengaluru, pp. 1–5, 2016. **(Chapter 4)**
- M Bharadwaj, J Prajapati, R Bhattacharjee, "Design of Novel Beam-switching Semicircular Microstrip Antenna and Transmission Line with Graphene at Terahertz Frequencies," *2016 IEEE Asia-Pacific Microwave Conference (APMC)*, New-Delhi, pp. 1–4, 2016. **(Chapter 4)**

Other Contributions (Not Part of This Thesis)

Journal Publications

- Prajapati, J., **Bharadwaj, M.**, Chatterjee, A., and Bhattacharjee, *"Radiation field analysis of photoconductive antenna using an improved carrier dynamics"*, Semiconductor Science and Technology, IOP Publishing, 2018 .
- Prajapati, J., **Bharadwaj, M.**, Chatterjee, A., and Bhattacharjee, *"Magnetic Field-Assisted Radiation Enhancement from a Large Aperture Photoconductive Antenna"*, Microwave Theory and Techniques IEEE Transactions On, 1-11, 2018.
- Prajapati, J., **Bharadwaj, M.**, Chatterjee, A., and Bhattacharjee, *"Circuit modeling and performance analysis of photoconductive antenna"*, Optics Communications, 394, 69-79.
- Prajapati, J., Boini, V. K., **Bharadwaj, M.**, and Bhattacharjee, R., *"Comments and Replies"*, IEEE Transactions on Antennas and Propagation, 64(6), 2583(2016).
- Sharma, S., J. C. Dutta, and **M. Bharadwaj**. *"'Response of ISFET as a function of reference Electrode Position and a rule for reference electrode placement'"*, Canadian Journal on Electrical and Electronics Engineering 2.1 (2011).

Conference Publications

- Prajapati, J., **Bharadwaj, M.**, Chatterjee, A., and Bhattacharjee, *"Equivalent electrical circuit model of Terahertz photoconductive antenna receiver in a pulsed system"*, In Innovations in Electronics, Signal Processing and Communication (IESC), 2017 International Conference on (pp. 186-189). IEEE.
- Prajapati, J., **Bharadwaj, M.**, Chatterjee, A., and Bhattacharjee, R., *"Time dependent capacitance in Photoconductive Antenna"*, In Applied Electromagnetics Conference (AEMC), 2015 IEEE (pp. 1-2). IEEE.
- Prajapati, J., **Bharadwaj, M.**, Chatterjee, A., and Bhattacharjee, R., *"A parametric study of photo carrier generation in Photoconductive Antenna"*, In Computers and Devices for Communication (CODEC), International Conference on, pp. 1-4. 2015 IEEE.
- J. Prajapati, **M. Bharadwaj**, A. Chatterjee and R. Bhattacharjee, *"Effect of near fields on radiation from photoconductive antenna"*, 2017 IEEE MTT-S International Conference on Numerical Electromagnetic and Multiphysics Modelling and Optimization for RF, Microwave, and Terahertz Applications (NEMO), Seville, Spain, 2017, pp. 140-142.

Bibliography

[1] R. S. of ITU, "Technology trends of active services in the frequency range 275-3000 GHz," International Telecommunication Union, Tech. Rep., 2015.

[2] P. H. Siegel *et al.*, "Terahertz technology," *IEEE Transactions on microwave theory and techniques*, vol. 50, no. 3, pp. 910–928, 2002.

[3] B. Ferguson and X.-C. Zhang, "Materials for Terahertz science and technology," *Nature materials*, vol. 1, no. 1, p. 26, 2002.

[4] E. Pickwell and V. Wallace, "Biomedical applications of Terahertz technology," *Journal of Physics D: Applied Physics*, vol. 39, no. 17, p. R301, 2006.

[5] H. Tabata, "Application of Terahertz wave technology in the biomedical field," *IEEE Transactions on Terahertz Science and Technology*, vol. 5, no. 6, pp. 1146–1153, 2015.

[6] P. H. Siegel, "Terahertz technology in biology and medicine," *IEEE transactions on microwave theory and techniques*, vol. 52, no. 10, pp. 2438–2447, 2004.

[7] A. Y. Pawar, D. D. Sonawane, K. B. Erande, and D. V. Derle, "Terahertz technology and its applications," *Drug invention today*, vol. 5, no. 2, pp. 157–163, 2013.

[8] M. C. Kemp, P. Taday, B. E. Cole, J. Cluff, A. J. Fitzgerald, and W. R. Tribe, "Security applications of Terahertz technology," in *Terahertz for Military and Security Applications*, vol. 5070. International Society for Optics and Photonics, 2003, pp. 44–53.

[9] P. de Maagt, "Terahertz technology for space and earth applications," in *2007 International workshop on Antenna Technology: Small and Smart Antennas Metamaterials and Applications*. IEEE, 2007, pp. 111–115.

[10] G. Chattopadhyay, "Terahertz antennas and systems for space borne platforms," in *Proceedings of the Fourth European Conference on Antennas and Propagation*. IEEE, 2010, pp. 1–7.

[11] S. M. Razavizadeh, M. Ahn, and I. Lee, "Three-dimensional beamforming: A new enabling technology for 5g wireless networks," *IEEE Signal Processing Magazine*, vol. 31, no. 6, pp. 94–101, 2014.

[12] I. F. Akyildiz, J. M. Jornet, and C. Han, "Terahertz band: Next frontier for wireless communications," *Physical Communication*, vol. 12, pp. 16–32, 2014.

[13] A. Bleicher, "The 5g phone future [news]," *IEEE spectrum*, vol. 50, no. 7, pp. 15–16, 2013.

[14] I. Akyildiz, J. Jornet, and M. Pierobon, "Propagation models for nanocommunication networks," in *Antennas and Propagation (EuCAP), 2010 Proceedings of the Fourth European Conference on*, 2010, pp. 1–5.

[15] J. Jornet and I. Akyildiz, "Graphene-based nano-antennas for electromagnetic nanocommunications in the Terahertz band," in *Antennas and Propagation (EuCAP), 2010 Proceedings of the Fourth European Conference on*, 2010, pp. 1–5.

[16] G. W. Hanson, "Fundamental transmitting properties of Carbon Nanotube Antenna," *IEEE Transactions on Antennas and Propagation*, vol. 53 No. 11, pp. 3426–3435, 2005.

[17] Y. Lan, B. Zeng, H. Zhang, B. Chen, and Z. Yang, "Simulation of carbon nanotube THz antenna arrays," *International Journal of Infrared and Millimeter Waves*, vol. 27, no. 6, pp. 871–877, 2006. [Online]. Available: http://dx.doi.org/10.1007/s10762-006-9123-6

[18] R. Piesiewicz, T. Kleine-Ostmann, N. Krumbholz, D. Mittleman, M. Koch, J. Schoebel, and T. Kurner, "Short-range ultra-broadband Terahertz communications: Concepts and perspectives," *Antennas and Propagation Magazine, IEEE*, vol. 49, no. 6, pp. 24–39, Dec 2007.

[19] J. Federici and L. Moeller, "Review of Terahertz and sub-Terahertz wireless communications," *Journal of Applied Physics*, vol. 107, no. 11, p. 111101, 2010.

[20] D. Auston, K. Cheung, and P. Smith, "Picosecond photoconducting Hertzian dipoles," *Applied Physics Letters*, vol. 45, no. 3, pp. 284–286, 1984.

[21] E. Brown, F. Smith, and K. McIntosh, "Coherent millimeter-wave generation by heterodyne conversion in low-temperature-grown GaAs photoconductors," *Journal of Applied Physics*, vol. 73, no. 3, pp. 1480–1484, 1993.

[22] K. S. Novoselov, A. K. Geim, S. V. Morozov, D. Jiang, Y. Zhang, S. V. Dubonos, I. V. Grigorieva, and A. A. Firsov, "Electric field effect in atomically thin carbon films," *science*, vol. 306, no. 5696, pp. 666–669, 2004.

[23] P. R. Smith, D. H. Auston, and M. C. Nuss, "Subpicosecond photoconducting dipole antennas," *Quantum Electronics, IEEE Journal of*, vol. 24, no. 2, pp. 255–260, 1988.

[24] B. Hu, J. Darrow, X.-C. Zhang, D. Auston, and P. Smith, "Optically steerable photoconducting antennas," *Applied physics letters*, vol. 56, no. 10, pp. 886–888, 1990.

[25] J. Darrow, B. Hu, X.-C. Zhang, and D. Auston, "Subpicosecond electromagnetic pulses from large-aperture photoconducting antennas," *Optics letters*, vol. 15, no. 6, pp. 323–325, 1990.

[26] D. Grischkowsky and N. Katzenellenbogen, "Femtosecond pulses of Terahertz radiation: physics and applications," *OSA Proceedings on Picosecond Electronics and Optoelectronics. TCL Sollner and J. Shah, editors. OSA, Washington, DC*, vol. 9, pp. 9–14, 1991.

[27] J. T. Darrow, X.-C. Zhang, and D. H. Auston, "Power scaling of large-aperture photoconducting antennas," *Applied physics letters*, vol. 58.1, pp. 25–27, 1991.

[28] J. T. Darrow, X.-C. Zhang, D. H. Auston, and J. D. Morse, "Saturation properties of large-aperture photoconducting antennas," *Quantum Electronics, IEEE Journal of*, vol. 28, no. 6, pp. 1607–1616, 1992.

[29] P. Benicewicz, J. Roberts, and A. Taylor, "Scaling of Terahertz radiation from large-aperture biased photoconductors," *JOSA B*, vol. 11, no. 12, pp. 2533–2546, 1994.

[30] C.-S. Y. Chou, Rone-Hwa and C.-L. Pan, "Effects of pump pulse propagation and spatial distribution of bias fields on terahertz generation from photoconductive antennas," *Journal of Applied Physics*, vol. 114.4, p. 043108, 2013.

[31] E. Brown, K. McIntosh, F. Smith, M. Manfra, and C. Dennis, "Measurements of optical-heterodyne conversion in low-temperature-grown GaAs," *Applied physics letters*, vol. 62, no. 11, pp. 1206–1208, 1993.

[32] I. S. Gregory, C. Baker, W. R. Tribe, I. V. Bradley, M. J. Evans, E. H. Linfield, G. Davies, and M. Missous, "Optimization of photomixers and antennas for continuous-wave Terahertz emission," *Quantum Electronics, IEEE Journal of*, vol. 41, no. 5, pp. 717–728, 2005.

[33] K. Ezdi, M. Islam, Y. Reddy, C. Jördens, A. Enders, and M. Koch, "A numerical study of photoconductive dipole antennas: the real emission frequency and an improved antenna design," in *Photonics Europe*. International Society for Optics and Photonics, 2006, pp. 61 940G–61 940G.

[34] C. W. Berry and M. Jarrahi, "Principles of impedance matching in photoconductive antennas," *Journal of Infrared, Millimeter, and Terahertz Waves*, vol. 33, no. 12, pp. 1182–1189, 2012.

[35] Y. Huang, N. Khiabani, Y. Shen, and D. Li, "Terahertz photoconductive antenna efficiency," in *Antenna Technology (iWAT), 2011 International Workshop on*. IEEE, 2011, pp. 152–156.

[36] D. S. Kim and D. Citrin, "Coulomb and radiation screening in photoconductive Terahertz sources," *Applied physics letters*, vol. 88, no. 16, p. 161117, 2006.

[37] G. C. Loata, M. D. Thomson, T. Löffler, and H. G. Roskos, "Radiation field screening in photoconductive antennae studied via pulsed terahertz emission spectroscopy," *Applied Physics Letters*, vol. 91, no. 23, p. 232506, 2007.

[38] D. Li, Y. Huang, C. Yang, and X. Tian, "Optimization of the photoconductive antenna gap," in *Antennas and Propagation, 2007. EuCAP 2007. The Second European Conference on*. IET, 2007, pp. 1–4.

[39] D. Li, Y. Huang, and Y.-C. Shen, "Investigation on bias electric fields produced by improved Photoconductive Antenna structures," in *Antenna Technology: Small Antennas and Novel Metamaterials, 2008. iWAT 2008. International Workshop on*. IEEE, 2008, pp. 306–309.

[40] N. Khiabani, Y. Huang, and Y.-C. Shen, "Discussions on the main parameters of THz photoconductive antennas as emitters," in *Antennas and Propagation (EUCAP), Proceedings of the 5th European Conference on*. IEEE, 2011, pp. 462–466.

[41] D. Saeedkia, "Terahertz photoconductive antennas: Principles and Applications," in *Antennas and Propagation (EUCAP), Proceedings of the 5th European Conference on*. IEEE, 2011, pp. 3326–3328.

[42] N. Khiabani, Y. Huang, Y.-c. Shen, and A. A. B. Sajak, "Photoconductive THz antennas," in *Antennas and Propagation Conference (LAPC), 2013 Loughborough*. IEEE, 2013, pp. 307–310.

[43] N. Khiabani, Y. Huang, Y. chun Shen, and S. Boyes, "Theoretical modeling of a photoconductive antenna in a Terahertz pulsed system," *Antennas and Propagation, IEEE Transactions on*, vol. 61, no. 4, pp. 1538–1546, April 2013.

[44] N. Khiabani, Y. Huang, Y.-c. Shen, and S. Boyes, "THz photoconductive antennas in Pulsed systems and CW systems," in *Antenna Technology (iWAT), 2012 IEEE International Workshop on*. IEEE, 2012, pp. 181–184.

[45] J. Prajapati, V. Boini, M. Bharadwaj, and R. Bhattacharjee, "Comments and Replies," *IEEE Transactions on Antennas and Propagation*, vol. 64, no. 6, p. 2583, 2016.

[46] J. Prajapati, M. Bharadwaj, A. Chatterjee, and R. Bhattacharjee, "Circuit modeling and performance analysis of photoconductive antenna," *Optics Communications*, vol. 394, pp. 69–79, 2017.

[47] N. Khiabani, Y. Huang, Y.-C. Shen, and S. Boyes, "Efficiency calculation of THz photoconductive antennas in a pulsed system," in *Antennas and Propagation (EUCAP), 2012 6th European Conference on*. IEEE, 2012, pp. 3250–3254.

[48] ——, "Time variant source resistance in the THz photoconductive antenna," in *Antennas and Propagation Conference (LAPC), 2011 Loughborough*. IEEE, 2011, pp. 1–3.

[49] J. Prajapati, M. Bharadwaj, A. Chatterjee, and R. Bhattacharjee, "Magnetic field-assisted radiation enhancement from a large aperture photoconductive antenna," *IEEE Transactions on Microwave Theory and Techniques*, vol. 66, no. 2, pp. 678–687, 2018.

[50] Y. Zhou and S. Lucyszyn, "HFSS^{TM} modelling anomalies with THz metal-pipe rectangular waveguide structures at room temperature," *Piers Online*, vol. 5, no. 3, pp. 201–211, 2009.

[51] E. Episkopou, S. Papantonis, W. Otter, and S. Lucyszyn, "Demystifying material parameters for Terahertz electromagnetic simulation," in *Optical and Semiconductor Devices*. 4th UK/EU-China Workshop on Millimetre Wave and Terahertz Technology, 2011, pp. 80–81.

[52] E. Episkopou, S. Papantonis, W. J. Otter, and S. Lucyszyn, "Defining material parameters in commercial EM solvers for arbitrary metal-based THz structures," *Terahertz Science and Technology, IEEE Transactions on*, vol. 2, no. 5, pp. 513–524, 2012.

[53] E. Moreno-Perez, M. Pantoja, S. García, A. R. Bretones, and R. G. Martín, "Time domain simulation of THz photoconductive antennas," in *2012 6th European Conference on Antennas and Propagation (EUCAP)*. IEEE, 2012, pp. 1054–1057.

[54] E. Moreno, M. F. Pantoja, S. G. Garcia, A. R. Bretones, and R. G. Martin, "Time-domain numerical modeling of THz photoconductive antennas," *Terahertz Science and Technology, IEEE Transactions on*, vol. 4, no. 4, pp. 490–500, 2014.

[55] E. Moreno, M. Pantoja, A. R. Bretones, M. Ruiz-Cabello, and S. G. Garcia, "A comparison of the THz photoconductive antennas," *IEEE Antennas and Wireless Propagation Letters*, vol. 13, pp. 682–685, 2014.

[56] E. Moreno, M. Pantoja, S. Garcia, J. Roldan, F. Ruiz, A. Bretones, and R. Martin, "On the simulation of carrier dynamics in Terahertz photoconductive antennas," in *Antennas and Propagation (EuCAP), 2013 7th European Conference on*. IEEE, 2013, pp. 749–750.

[57] N. Khiabani, Y. Huang, Y.-c. Shen, S. Boyes, and Q. Xu, "A novel simulation method for THz photoconductive antenna characterization," in *Antennas and Propagation (EuCAP), 2013 7th European Conference on*. IEEE, 2013, pp. 751–754.

[58] M. Tamagnone, J. Gomez-Diaz, J. Mosig, and J. Perruisseau-Carrier, "Analysis and design of Terahertz antennas based on plasmonic resonant Graphene sheets," *Journal of Applied Physics*, vol. 112, no. 11, p. 114915, 2012.

[59] I. Llatser, C. Kremers, A. Cabellos-Aparicio, E. Alarcón, and D. N. Chigrin, "Comparison of the resonant frequency in GRAPHENE and metallic nano-antennas," in *AIP Conference Proceedings*, vol. 1475, no. 1. AIP, 2012, pp. 143–145.

[60] G. W. Hanson, "Dyadic Greens functions and guided surface waves for a surface conductivity model of Graphene," *Journal of Applied Physics*, vol. 103, no. 6, p. 064302, 2008.

[61] S. Dash and A. Patnaik, "Material selection for THz antennas," *Microwave and Optical Technology Letters*, vol. 60, no. 5, pp. 1183–1187, 2018.

[62] J. M. Jornet and A. Cabellos, "On the feeding mechanisms for Graphene-based THz plasmonic nano-antennas," in *Nanotechnology (IEEE-NANO), 2015 IEEE 15th International Conference on*. IEEE, 2015, pp. 168–171.

[63] J. M. Jornet and I. F. Akyildiz, "Graphene-based plasmonic nano-transceiver for Terahertz band communication," in *Antennas and Propagation (EuCAP), 2014 8th European Conference on*. IEEE, 2014, pp. 492–496.

[64] R. F. Harrington, *Time-harmonic electromagnetic fields*. McGraw-Hill, 1961.

[65] A. Sharma and G. Singh, "Rectangular microstirp patch antenna design at THz frequency for short distance wireless communication systems," *Journal of Infrared, Millimeter, and Terahertz Waves*, vol. 30, no. 1, pp. 1–7, 2009.

[66] R. Garg, P. Bhartia, I. Bahl, and A. Ittipiboon, *Microstrip Antenna Design Handbook*. Artech House, Inc., 2001.

[67] G. Kumar and K. Ray, *Broadband microstrip antennas*. Artech House, 2002.

[68] C. A. Balanis, *Antenna Theory: Analysis and Design*. Wiley-Interscience, 2005.

[69] Y.-S. Jin, G.-J. Kim, and S.-G. Jeon, "Terahertz dielectric properties of polymers," *Jounal of Korean Physical Society*, vol. 49.2, pp. 513–517, 2006.

[70] J. Hejase, P. R. Paladhi, P. P. Chahal *et al.*, "Terahertz characterization of dielectric substrates for component design and nondestructive evaluation of packages," *Components, Packaging and Manufacturing Technology, IEEE Transactions on*, vol. 1, no. 11, pp. 1685–1694, 2011.

[71] D. M. Pozar, *Microwave Engineering*. John Wiley & Sons, Inc., 2005.

[72] E. Brown, "A photoconductive model for superior GaAs THz photomixers," *Applied physics letters*, vol. 75, no. 6, pp. 769–771, 1999.

[73] H. Pahlevaninezhad, B. Heshmat, and T. Darcie, "Modeling Terahertz heterodyne detection based on photomixing," in *Radar Conference, 2010 IEEE*. IEEE, 2010, pp. 113–116.

[74] H. Němec, A. Pashkin, P. Kužel, M. Khazan, S. Schnüll, and I. Wilke, "Carrier dynamics in low-temperature grown GaAs studied by terahertz emission spectroscopy," *Journal of Applied Physics*, vol. 90, no. 3, pp. 1303–1306, 2001.

[75] P. U. Jepsen and S. Keiding, "Radiation patterns from lens-coupled Terahertz antennas," *Optics Letters*, vol. 20, no. 8, pp. 807–809, 1995.

[76] R. H. Kingston, *Detection of optical and infrared radiation*. Springer, 2013, vol. 10.

[77] S. M. Sze and K. K. Ng, *Physics of Semiconductor Devices*. John wiley & sons, 2006.

[78] I. Gregory, W. Tribe, B. Cole, M. Evans, E. Linfield, A. Davies, and M. Missous, "Resonant dipole antennas for continuous-wave Terahertz photomixers," *Applied Physics Letters*, vol. 85, no. 9, pp. 1622–1624, 2004.

[79] N. Vieweg, M. Mikulics, M. Scheller, K. Ezdi, R. Wilk, H.-W. Hübers, and M. Koch, "Impact of the contact metallization on the performance of photoconductive THz antennas," *Optics express*, vol. 16, no. 24, pp. 19 695–19 705, 2008.

[80] J. B. Soole and H. Schumacher, "Transit-time limited frequency response of InGaAs MSM photodetectors," *IEEE Transactions on Electron Devices*, vol. 37, no. 11, pp. 2285–2291, 1990.

[81] N. Engheta, C. Papas, and C. Elachi, "Radiation patterns of interfacial dipole antennas," *Radio Science*, vol. 17, no. 6, pp. 1557–1566, 1982.

[82] M. Dragoman, A. Muller, D. Dragoman, F. Coccetti, and R. Plana, "Terahertz antenna based on Graphene," *Journal of Applied Physics*, vol. 107, no. 10, p. 104313, 2010.

[83] J. M. Jornet and I. F. Akyildiz, "Graphene-based nano-antennas for electromagnetic nanocommunications in the Terahertz band," in *Antennas and Propagation (EuCAP), 2010 Proceedings of the Fourth European Conference on*. IEEE, 2010, pp. 1–5.

[84] I. Llatser, C. Kremers, D. N. Chigrin, J. M. Jornet, M. C. Lemme, A. Cabellos-Aparicio, and E. Alarcón, "Characterization of Graphene-based nano-antennas in the Terahertz band," in *2012 6th European Conference on Antennas and Propagation (EUCAP)*. IEEE, 2012, pp. 194–198.

[85] H.-q. Xia, Q.-X. Pan, J. Hu, and W.-Y. Yin, "Design of a novel Graphene Terahertz antenna at 500 GHz with reconfigurable radiation pattern," in *Antennas and Propagation & USNC/URSI National Radio Science Meeting, 2015 IEEE International Symposium on*. IEEE, 2015, pp. 1462–1463.

[86] P. E. Inc. (2018) Product datasheet PE71S2020. [Online]. Available: https://www.pasternack.com/absorptive-spst-pin-diode-switch-40-ghz-30-dbm-2.92mm-pe71s2020-p.aspx

[87] MACOM. Product datasheet MA4AGSW1A. [Online]. Available: https://www.macom.com/products/product-detail/MA4AGSW1A

[88] L.-Y. Ma, N. Soin, M. H. M. Daut, and S. F. W. M. Hatta, "Comprehensive study on RF-MEMS switches used for 5G scenario," *IEEE Access*, vol. 7, pp. 107 506–107 522, 2019.

[89] P. Tassin, T. Koschny, and C. M. Soukoulis, "Graphene for Terahertz applications," *Science*, vol. 341, no. 6146, pp. 620–621, 2013.

[90] A. Cabellos-Aparicio, I. Llatser, E. Alarcon, A. Hsu, and T. Palacios, "Use of Terahertz photoconductive sources to characterize tunable Graphene RF plasmonic antennas," *IEEE Transactions on Nanotechnology*, vol. 14, no. 2, pp. 390–396, 2015.

[91] C. R. Dean, A. F. Young, I. Meric, C. Lee, L. Wang, S. Sorgenfrei, K. Watanabe, T. Taniguchi, P. Kim, K. L. Shepard *et al.*, "Boron nitride substrates for high-quality Graphene electronics," *Nature nanotechnology*, vol. 5, no. 10, p. 722, 2010.

[92] S. Fratini and F. Guinea, "Substrate-limited electron dynamics in Graphene," *Physical Review B*, vol. 77, no. 19, p. 195415, 2008.

[93] A. Konar, T. Fang, and D. Jena, "Effect of high-κ gate dielectrics on charge transport in Graphene-based field effect transistors," *Physical Review B*, vol. 82, no. 11, p. 115452, 2010.

[94] J. Kumar, B. Basu, F. Talukdar, and A. Nandi, "Graphene-based wideband antenna for aeronautical radio-navigation applications," *Journal of Electromagnetic Waves and Applications*, vol. 31, no. 18, pp. 2046–2054, 2017.

[95] S. Majee, C. Liu, B. Wu, S.-L. Zhang, and Z.-B. Zhang, "Ink-jet printed highly conductive pristine Graphene patterns achieved with water-based ink and aqueous doping processing," *Carbon*, vol. 114, pp. 77–83, 2017.

[96] F. Torrisi, T. Hasan, W. Wu, Z. Sun, A. Lombardo, T. S. Kulmala, G.-W. Hsieh, S. Jung, F. Bonaccorso, P. J. Paul *et al.*, "Inkjet-printed Graphene electronics," *ACS nano*, vol. 6, no. 4, pp. 2992–3006, 2012.

[97] H. Gao, K. Zhu, G. Hu, and C. Xue, "Large-scale Graphene production by ultrasound-assisted exfoliation of natural Graphite in supercritical co_2/h_2o medium," *Chemical Engineering Journal*, vol. 308, pp. 872–879, 2017.

[98] P. Yu, S. E. Lowe, G. P. Simon, and Y. L. Zhong, "Electrochemical exfoliation of Graphite and production of functional Graphene," *Current opinion in colloid & interface science*, vol. 20, no. 5-6, pp. 329–338, 2015.

[99] J. Liu, C. K. Poh, D. Zhan, L. Lai, S. H. Lim, L. Wang, X. Liu, N. G. Sahoo, C. Li, Z. Shen *et al.*, "Improved synthesis of Graphene flakes from the multiple electrochemical exfoliation of Graphite rod," *Nano Energy*, vol. 2, no. 3, pp. 377–386, 2013.

[100] A. C. Ferrari, J. Meyer, V. Scardaci, C. Casiraghi, M. Lazzeri, F. Mauri, S. Piscanec, D. Jiang, K. Novoselov, S. Roth *et al.*, "Raman spectrum of Graphene and Graphene layers," *Physical review letters*, vol. 97, no. 18, p. 187401, 2006.

[101] L. Malard, M. Pimenta, G. Dresselhaus, and M. Dresselhaus, "Raman spectroscopy in Graphene," *Physics reports*, vol. 473, no. 5-6, pp. 51–87, 2009.

[102] W.-W. Liu, B.-Y. Xia, X.-X. Wang, and J.-N. Wang, "Exfoliation and dispersion of Graphene in Ethanol-water mixtures," *Frontiers of Materials Science*, vol. 6, no. 2, pp. 176–182, 2012.